

Differential fast-scanning calorimetry and
differential reheating as direct and indirect methods
to study the critical cooling rates of Al-Zn-Mg-Cu
alloys

Dissertation

zur

Erlangung des akademischen Grades

Doktor-Ingenieur Dr.-Ing.

der Fakultät für Maschinenbau und Schiffstechnik

der Universität Rostock

vorgelegt von

David Zohrabyan, geb. am 19.Oct.1984 in Yerevan

aus Berlin

Rostock, 10.02.2014

urn:nbn:de:gbv:28-diss2015-0186-6

Gutachter :

Gutachter 1: *Prof. Dr.-Ing. habil. Olaf Keßler*

Universität Rostock
Fakultät für Maschinenbau und Schiffstechnik
Lehrstuhl für Werkstofftechnik

Gutachter 2: *Prof. Dr. rer. nat . habil. Christoph Schick*

Universität Rostock
Mathematisch-Naturwissenschaftliche Fakultät
Institute für Physik / Arbeitsgruppe Polymerphysik

Gutachter 3: *Prof. Dr. John Banhart*

Helmholtz Zentrum Berlin
Institut für Angewandte Materialforschung

Datum der Einreichung: 10.02.2014,

Datum der Verteidigung: 13.10.2014

Contents

Differential fast-scanning calorimetry and differential reheating as direct and indirect methods to study the critical cooling rates of Al-Zn-Mg-Cu alloys.....		4
1	Introduction.....	4
2	Literature Review	7
2.1	State of the art in the field of wrought Al-Zn-Mg-Cu- alloys.....	7
2.1.1	Chemical Composition.....	7
2.1.2	Age Hardening.....	9
2.1.3	Microstructure.....	11
2.2	Continuous Cooling precipitation diagrams of Aluminum alloys	13
3	Experimental.....	16
3.1	Materials	16
3.2	Methods.....	18
3.2.1	DSC and DFSC devices	18
3.2.2	Sample preparation for the DFSC's	21
3.2.3	Differential Reheating (DRM) Method.....	25
3.3	Trustworthiness of the Differential Reheating Method (DRM).....	37
3.4	Recording of the precipitation reactions by conventional DSC	43
3.4.1	Conventional DSC sample preparation	43
3.4.2	Sample preparation for metallographic, SEM+EDX and hardness analysis	48
3.4.3	Nano-indentation.....	49
4	Results and Discussion	53

4.1	Precipitation reactions during continuous cooling inside conventional DSC	53
4.2	Ultra-Fast Scanning FSC data obtained via DRM method	65
4.3	Metallographic analysis	71
4.4	Scanning Electron Microscopy and EDX analysis.....	75
4.5	Nano-Indentation results	84
5	Summary	87
	Eidesstattliche Versicherung	89
	Abkürzungsverzeichnis.....	90
6	References	91

Differential fast-scanning calorimetry and differential reheating as direct and indirect methods to study the critical cooling rates of Al-Zn-Mg-Cu alloys

1 Introduction

Precipitation reactions inside aluminum alloys are known to be very important for hardness and yield strength. Premature precipitation during quenching from solution annealing decreases the yield strength after aging. A methodology to determine the amount of precipitates as function of quench rate (quench sensitivity) for a wide range of aluminum alloys is proposed. The method allows determining the critical cooling rate for suppressing precipitation during quenching. Differential fast-scanning calorimetry was applied to cover the cooling rate range needed for high alloyed materials. New methodology, called differential reheating method, was applied for differential fast-scanning calorimetry (DFSC) and differential scanning calorimetry (DSC). The combination of DSC and DFSC extends the available cooling rate range for precipitation studies from mK/s up to some 10.000 K/s.

Knowledge of the properties like yield strength is essential when designing a component, because it generally shows the upper limit of the load that can be applied. Aluminum alloys are generally used because of their preferable strength to weight ratio. High purity aluminum in the annealed condition has very low yield strength of a few 10 MPa. Dislocation movement is the dominant carrier of plasticity. Different types of crystallographic defects can create obstacles for dislocation movement resulting in yield strength increase. Precipitation hardening (age hardening) is a heat treatment method used to increase the yield strength of metals, including alloys of aluminum. Lower solubility of alloying elements with decreasing temperature is a requirement to produce the needed particles. These particles can be introduced in the matrix, in a finely dispersed way, to increase the yield strength [1, 2]. Upon plastic deformation, gliding dislocations in the matrix are obstructed in their movement by these obstacles. In this case two options exist. Either the dislocations cut the particles, or they bow out between particles. The first mechanism prevails for tiny particles coherent with the matrix. If incoherent large particles occur, the governing mechanism is the second one. Further, also solute atoms, other dislocations and grain boundaries disturb the ideal lattice regularity, thus the dislocations movements can be hindered by these obstacles [1]. As a result yield strengths of some 100 MPa can be achieved with aluminum alloys.

Several investigations of the precipitation processes during aging exist, but only few investigations of the precipitation processes during cooling from solution annealing [3-9]. The Critical Cooling Rate (CCR) [10, 11] gives information about the rate where all precipitation reactions are fully suppressed [4, 7-9]. After cooling aluminum alloys with the CCR or even faster (overcritical cooling) the maximum hardness value after aging was achieved [4, 5, 8, 9, 12]. Depending on the type of aluminum alloy and composition, the CCR can change dramatically (for 6XXX aluminum alloys typically from some 0.1 K/s to some 1000 K/s) [Godard5]. The CCR is commonly obtained from continuous cooling precipitation (CCP) diagrams. However CCP diagrams for aluminum alloys are hardly available. The common recording procedures for steels are not usable and only few other experimental procedures exist. One possibility for recording CCP diagrams of aluminum alloys is given by differential scanning calorimetry (DSC) [4-6, 8, 9, 13, 14]. Due to the fact that modern DSC still has a limited cooling rate range (typically below 10 K/s), aluminum alloys which have CCR higher than the cooling rate range achievable by the device, cannot be studied. [4, 6, 8, 9]. The problem may be solved by the recently developed Differential Fast-scanning calorimetry [15-17] reaching cooling rates up to 10^6 K/s.

Differential fast-scanning calorimeters are available nowadays e.g. for polymers, but they are not well suited for studying materials like aluminum alloys. The differential fast scanning calorimeter (DFSC) [15], applied here, utilizes extremely small samples in dimension of some 10 μm . This small sample dimensions give the possibility to reach faster cooling rates than in conventional DSC, because sample and addenda (everything which is not related to sample) heat capacity and maximum possible cooling rate are dependent. This thesis presents first experiments utilizing DFSC for studying precipitation reactions in high alloyed aluminum alloys. New method was developed, based on reheating experiments, to study the precipitation reactions over a wide cooling rate range from 1 - 3000 K/s. This covers the cooling rate range where also for highly alloyed Al- alloys no precipitation occurs.

Aluminum was a 'late comer' and can still be called a young metal, as compared to other structural materials used today. The process to produce aluminum alloys on an economic basis was developed only about 100 years ago because of the fact that aluminum is difficult to recover from its ore. However, due to their versatilities, e.g. low specific weight, good heat and electrical conductivity, high reflectivity and resistance to corrosion, aluminum is consumed more than all other non-ferrous metals combined, including copper and its alloys

as well as lead, tin and zinc. Today aluminum is the second most widely used metal in the world. About 80% of aluminum is used for wrought products, e.g. rolled plates, sheet, foil, extrusions, rod, bar, wire. Aluminum began to achieve industrial importance in the period 1900-1914. The discovery of the age-hardening effect by the German metallurgist A. Wilm in 1907 was one of the most important developments on this path [18]. Wilm had attempted to harden an aluminum alloy containing copper and magnesium by heating it to 500 °C and then quenching in water (similar procedure used for steels). The experiment was unsuccessful, the alloy remained still soft. Some days later having an occasion to re-test the same alloy, Wilm found that it had become much harder. Further the strength was also increased. Weight reduction is mainly achieved via decrease in density [1]. Therefore this is the reason why Aluminium alloys are connected to transportation, notably to aerospace industry. This was one of the main stimuli for them to develop very fast. The strength to weight ratio is also a dominant consideration. The advantages of the decreased density become even more important in engineering design when parameters such as stiffness and resistance to buckling are being involved. In most countries aluminum is being used mainly in following areas: building and construction, containers and packaging, transportation, electrical conductors, machinery and equipment. Although the most metals will alloy with aluminum, comparatively few have sufficient solid solubility to serve as major alloying additions. From most of the elements which are being used, only zinc, magnesium, copper, and silicon have significant solid solubility. But it's very useful to mention that there is couple of other elements with very little solid solubility typically less than a percent, which play an important role in improvement mechanisms for the alloy properties. In most cases the maximum solid solubility occurs at eutectic and peritectic temperatures [3]. Wrought alloys that constitute heat treatable, (precipitation hardenable) aluminum alloys include the 2XXX, 6XXX, 7XXX, and some of the 8XXX series alloys [19].

- 2XXX series – Al-Cu-Mg
- 6XXX series - Al-Mg-Si
- 7XXX series - Al-Zn-Mg

2 Literature Review

2.1 State of the art in the field of wrought Al-Zn-Mg-Cu- alloys

2.1.1 Chemical Composition

Combinations of magnesium and zinc in aluminum provide a class of heat treatable alloys, some of which develop the highest strengths presently known for commercial aluminum based alloys. This is the result of the combination of elements that have a high solid solubility in aluminum and also develop unusually high precipitation-hardening characteristics [13, 14, 20]. Supplementary alloying additions to such alloys include chromium, copper, manganese. Recent advances in aluminum alloys/temper development are maintaining aluminum alloys as the materials of choice for future commercial aircraft structures, where there is a need to meet cost and weight-requirement objectives. Al-Zn-Mg-Cu Alloys of complex specified properties, such as strength, ductility, fracture resistance, stress corrosion cracking resistance are required for the application in structures operating under heavy loadings (aircraft) with prescribed high level of safety margin.

Aluminum alloys, due to convenient strength-to-density ratio, have found extensive application in heavy-duty structures. This is the case with Al-Zn-Mg-Cu alloys exhibiting the highest level of strength, but in the same time high level of susceptibility to fracture and stress corrosion. Mechanical properties of Al-Zn-Mg-Cu alloys are depended on the chemical composition, primarily on total Zn and Mg content and Zn/Mg ratio, on the presence of Mn, Cr, Zr, and impurities Fe and Si, on the microstructure, as a result of fabrication and heat treatment conditions, e.g. on morphology, distribution and volume portion of intermetallic phases and texture. Based on requirement to develop aluminum alloys with ultimate tensile strength above 700 MPa ($R_m > 700$ MPa) and satisfactory level of ductility and fracture toughness, several alloys had been designed with Zn content between 6 and 8.8 % and Mg content of 2.15 to 3.5%, saving the amount of other alloying elements (Cu, Mn, Cr, Zr). One of the main advantages of Al-Zn-Cu-Mg alloys in comparison with other aluminum based alloys is their high strength combined with high ductility. One disadvantage of the Al-Zn-Mg-Cu alloys is that their high room temperature strength is accompanied with a high deformation resistance at hot working temperatures. High deformation resistance at hot working temperatures may result in a low extrusion speed due to limitations in available ram pressure and due to heat generation during extrusion. Aluminum alloys of the 7075 type (Al-Zn-Mg-

Cu) are widely used in airframe structures, they provide very high strength and stiffness, but are prone to stress corrosion cracking, particularly when aged to near the peak strength T6 condition. Their resistance to stress corrosion cracking can be increased by over aging to the T73 temper, with a loss of strength. For example, the yield strength of the 7075-T73 is about 10 to 15% lower than of 7075-T6.

To replace the traditional 7xxx Al alloys, such as the 7075, Russian B95, and the Chinese LC4 and LC9 alloys (similar types), which were widely used in Chinese airplanes, the Beijing Institute of Aeronautical Materials has recently developed a new super high strength Al-Zn-Mg-Cu alloy (C912: Zn-8.6%, Mg-2.6%, Cu-2.4%). The tensile strength and compressive strength of the C912 alloy are higher than those of the traditional 7xxx aluminum alloys, such as 7049, 7075, 7178, and the Russian alloy B96, which have the highest strengths of the commercial Al-Zn-Mg-Cu alloys. To achieve the objective of obtaining a superior alloy, micro alloying elements were added to improve the mechanical and corrosion properties of the various commercial alloys. Although the amount of micro alloying elements is less than 1%, they lead to improved combinations of strength and ductility, weldability, toughness, and corrosion resistance. Micro alloying element additions such as Zr, Mn, Cr, Ag, and Sc can enhance many critical properties in aluminum alloys. Experiments were conducted to determine the general effect of micro alloying elements (such as Sc, Ni, and Ce) on the properties of various super high performance alloys. In particular, it was examined whether Sc has a positive effect on retarding the recrystallization and improving the strength and corrosion resistance of the Al-Zn-Mg-Cu alloys, just as it does in other aluminum alloys. Determination whether Nickel has an effect on the improving the strength and corrosion resistance, even though it has limited solubility in aluminum, and to examine whether Ce can improve the alloy's corrosion resistance just as it does in some other wrought aluminum alloys is of great importance in parallel [14].

2.1.2 Age Hardening

The basic requirement for the alloy to be suitable for age-hardening is a decrease in solid solubility of one or more of the alloying elements with decreasing temperature. The stages responsible for heat treatment are the following:

- Solution heat treatment at relatively high temperature within the single phase, where everything is being dissolved (wrought alloys)
- Rapid cooling or quenching, usually to room temperature for obtaining a supersaturated solid solution of the suitable alloying elements in aluminum
- Controlled decomposition of the supersaturated solid solution to form finely, dispersed precipitates usually by aging for convenient times at one and sometimes to different temperatures

The complete decomposition of the supersaturated solid solution is a very complex process which may involve various stages. Typically, GP zones and an intermediate precipitate may be formed in addition to the equilibrium phase. The GP zones are well ordered solute rich groups of atoms that may be only one or two atom planes in thickness. They retain the structure of the matrix with which they are said to be coherent although they can produce appreciable elastic strains in the surrounding matrix. Diffusion associated with their formation involves the movement of atoms over relatively short distances and is assisted by vacant lattice sites that are also retained on quenching. GP zones are normally very finely dispersed. Depending on the particular alloy system, the rate of nucleation and the actual structure may be greatly influenced by the presence of the excess vacant lattice sites. The intermediate precipitate is normally larger in the size than GP zone and is only partly coherent with lattice planes of the matrix. It has been generally accepted to have a definite composition and crystal structure both of which differ from those of the equilibrium. In some alloys the intermediate precipitate may be nucleated from, or at the sites of stable GP zones. In others this phase nucleates heterogeneously at lattice defects such as dislocations. Formation of the final equilibrium precipitate involves complete loss of coherency with the parent lattice. It forms only at relatively high ageing temperatures and, because it is coarsely dispersed. Most aluminum alloys that respond to ageing will undergo some hardening at ambient temperatures. This is called natural ageing, and may continue almost indefinitely, although the

rate of change becomes extremely slow after months or years. Ageing at a sufficiently elevated temperature (so called artificial ageing) is characterized by different behavior in which the hardness usually increases to a maximum value and then decreases. Maximum hardening in commercial alloys normally occurs when there is present a critical dispersion of GP zones, or an intermediate precipitate, or a combination of both them [1]. In various alloys more than one intermediate precipitate may be formed.

An understanding of the submicroscopic processes of precipitation in alloys developed, the equally invisible concept of dislocations was proposed in 1934 to explain plastic deformations. Mott and Nabarro first suggested an explanation of age hardening in terms of dislocations. They considered precipitates with respect to their localized stress fields and reason that, for, dislocations to pass through such regions, the applied stress must exceed the average internal stress. They also recognized that the inherent line tension of the dislocation placed limitations on its flexibility and therefore its capacity to curve between precipitates. Their theory predicted that critical particle spacing for maximum hardening would be approximately 10nm.

In 1934 Orowan proposed that the spacing between precipitates with large dislocations could expand into the region between them, rejoin and move on. Providing the particles themselves could withstand the applied stress, Orowan proposed that the flow stress for the alloy would be governed entirely by their spacing. It was also recognized that smaller precipitates could be sheared by moving dislocations. Each of these predictions has since been confirmed with the advent of the various microscopy techniques. Now it has been agreed that the greatest impedance to the dislocation motion and hence the maximum potential for strengthening by age hardening will take place when the alloy contains precipitates which are large enough to resist the shearing by the dislocations and yet are too finely spaced to be passed by.

Optimal dispersions, shapes and orientations of the precipitates are usually hard to achieve in the practical alloy. For example when the ageing treatments that give maximum strengthening in 7000 series of alloys produce microstructures containing only shearable GP zones, either properties like ductility, toughness, and resistance to stress corrosion cracking may be deficient. Frequently the maximum response to hardening occurs when the microstructure

contains a combination of the zones and relatively widely dispersed semi coherent intermediate precipitates. Greater hardening is possible if more uniform dispersions of one or more of these latter phases can be encouraged to form and this has been one of the main objectives of the multi stage ageing treatments. Micro alloying may also stimulate nucleation and growth of specific intermediate precipitates.

The main precipitation sequence during reheating of a complete supersaturated solid solution, that is thought to dominate hardening in 7xxx alloys involves mainly Mg and Zn atoms [18, 21, 22]:

- Supersaturated solid solution (SSSS) \rightarrow GPB zones \rightarrow S' \rightarrow S(MgZn₂)

The second possible precipitation sequence involves the T phase [22, 23]:

- SSSS \rightarrow GP \rightarrow T' \rightarrow T-phase (Al₂Zn₃Mg₃ or (AlZn)₄₉Mg₃₂)

The third possible precipitation sequence involves only Cu and Mg [5]:

- SSSS \rightarrow GPB \rightarrow S' \rightarrow S-phase (Al₂CuMg)

It seems possible that all of these three equilibrium phases could precipitate during quenching. They consume Zn, Mg and Cu atoms, which are necessary for subsequent hardening.

2.1.3 Microstructure

Conventionally produced wrought aluminum alloys originate from the cast ingots and all subsequent mechanical and thermal processing represents various degrees of change to the structure. The visible modifications consist of:

- Alteration of the composition and crystal structure of phases during casting

- Solution of more soluble phases, and spheroidization and coalescence to reduce their surface energy
- Elevated temperature precipitation of elements that had supersaturated the as-cast solid solution
- Mechanical fragmentation of brittle intermetallic phases and alignment of these particles in the principal direction of working

The main alloying element is zinc, which by itself is highly soluble in aluminum and exerts no appreciable influence on the microstructure of a simple alloy such as 7072. However, the class of alloy most frequently encountered contains magnesium and copper, as well as additives such as chromium, iron, and silicon. In cast ingot form alloy 7075 forms one or more variants of $(\text{Fe,Cr})_3\text{SiAl}_{12}$, Mg_2Si , and a pseudobinary eutectic made up of aluminum and MgZn_2 . The latter phase contains aluminum and copper as a substitute for zinc and can be written $\text{Mg}(\text{Zn,Cu,Al})_2$. Subsequent heating causes the iron-rich phases to transform to $\text{Al}_7\text{Cu}_2\text{Fe}$. Mg_2Si is relatively insoluble and tends to spheroidize somewhat. $\text{Mg}(\text{Zn,Cu,Al})_2$ rapidly begins to dissolve and at the same time some Al_2CuMg precipitates, which then requires high temperatures and lengthy soaking to become a completely dissolved. Chromium is precipitated from supersaturated solution as $\text{Cr}_2\text{Mg}_3\text{Al}_{18}$ dispersoid, concentrated heavily in the primary dendrite regions. A well solutionized wrought alloy contains only $\text{Al}_7\text{Cu}_2\text{Fe}$, $(\text{FeCr})_3\text{SiAl}_{12}$, and Mg_2Si , along with the dispersoid [24].

Other high and moderate strength 7xxx alloys represent variants from 7075, 7049A. Alloy 7049A with higher copper and zinc content has more Al_2CuMg to be dissolved at the solution annealing temperature. More dilute alloys are usually readily dissolving all of the zinc – rich phases. Signs of overheating in 7xxx alloys are usually related to segregated regions with unusual concentrations of Al_2CuMg . The homogeneous alloy has an equilibrium solidus that is well above the solution heat treating temperature range. If Al_2CuMg is present, very rapid heating rates can result in the appearance of rosettes because of the inadequate time for diffusion and particle dissolution before exceeding the nonequilibrium eutectic temperature.

2.2 Continuous Cooling precipitation diagrams of Aluminum alloys

Quenching is one of the key issues to affect the properties of aluminum alloys. With a full continuous cooling precipitation diagram it is possible to get the optimal quenching rate of an aluminum alloy. Method for the establishment of such diagrams for steels is a mature technique and many suitable diagrams has been studied widely as well as used in industry starting from long time ago. However it should be mentioned that the conventional methods for producing the continuous cooling precipitation diagrams for steels such as distortions method, are not suitable for aluminum alloys. Fortunately thermal analysis especially differential scanning calorimetry (DSC) is possible to help, and provides an approach for studying and constructing the continuous cooling precipitation diagrams for various types of aluminum alloys. Precipitation hardenable aluminum alloys progressively lose their ability to develop maximum strength and corrosion resistance with decreasing quench rate. The effect on strength is attributed to a decreased supersaturation resulting from a loss of vacancies and to precipitation in a size and distribution which does not contribute to strengthening. Fink and Wiley pioneered [25] attempts to describe the effect of quenching on properties of aluminum alloys. Using isothermal quenching techniques they developed C – type curves for strength of 7075-T6 and corrosion behavior of 2024-T4. These curves of temperature vs. time required to precipitate the fraction of solute which either reduced the strength by a constant amount or caused a change in the corrosion behavior illustrated the critical temperature where precipitation was most rapid. Critical temperature ranges from the C-type curves were used in conjunction with properties of samples continuously quenched at various rates from the solution treatment temperature to predict properties. Minimum average quench rate through the critical temperature range which would insure acceptable corrosion behavior was determined by inspection of the data, while strength was predicted from a plot of strength vs. average cooling rate. The method works well if the cooling rates are fairly constant (uniform), but it could not accurately predict the properties if cooling rates vary considerably during the quenching step of the precipitation hardening. Under isothermal conditions, the critical time for precipitation can be calculated from nucleation and from diffusion:

$$\frac{C_t}{k_1} = k_2 \exp \frac{k_3 k_4^2}{RT(k_4 - T)^2} \exp \frac{k_5}{RT} \quad (2)$$

where the:

C_t – critical time which is going to be required to precipitate constant amount,

k_1 – constant which equals the natural logarithm of the fraction untransformed, k_2 - constant related to the reciprocal of the number of nucleation sites, k_3 - constant related to the energy required to form a nucleus, k_4 - solvus temperature constant, k_5 - activation energy or diffusion constant. $R=8,31 \text{ J}\cdot\text{K}^{-1}\cdot\text{mol}^{-1}$, T - temperature in Kelvin.

Cahn and others [26] have shown that for the transformations where reaction rate is a function only of the amount transformed material and temperature, the measure of the amount which is transformed during continuous cooling is given by the following equation (3).

$$\int_{t_0}^{t_f} \frac{dt}{(T)C_t} = \tau \quad (3)$$

where the:

τ - quench factor,

t - time from the cooling curve

t_0 - time at the quench start

t_f - time at the end of the quench

$C_t(T)$ - critical time from the C-curve

The cooling process must be very fast to suppress the precipitation reactions which can take place during cooling; on the other hand the cooling should be slow enough to avoid the extensive residual stresses and distortions. Summarizing these counter requirements we can say that cooling must be carried out just above the critical cooling rate, which therefore is the slowest cooling rate where no precipitation occurs. The influence of the precipitation behavior is described by continuous cooling precipitation diagrams. These diagrams can be used to

optimize the quenching step of the age-hardening process. Moreover, simulation of the precipitation during the cooling step of the age-hardening process will be possible. There are available a few CCP diagrams for the aluminum alloys because of the recording procedures, such as dilatometry are not suitable for recording such diagrams. Reports from various sources show that the precipitation reactions are of exothermic origin and also the Differential Scanning Calorimetry can be used to investigate these processes.

The cooling rate dependence of the precipitation behavior of aluminum alloys can be described in analogy to continuous cooling transformation diagrams for steels. Such diagrams are not easily produced and available, meanwhile they can be now recorded by differential scanning calorimetry. During the cooling process of 6XXX alloys, can be seen mostly two to three main types of precipitation reactions. To get an idea about the phases and their structure advanced analysis involving various techniques (XRD, SEM, TEM, and EDX) are going to be needed. Fig. 1 represents the time/temperature profile of the 6005A alloy during cooling, the black lines show the regions where the precipitation is occurring, the start and end temperatures [8].

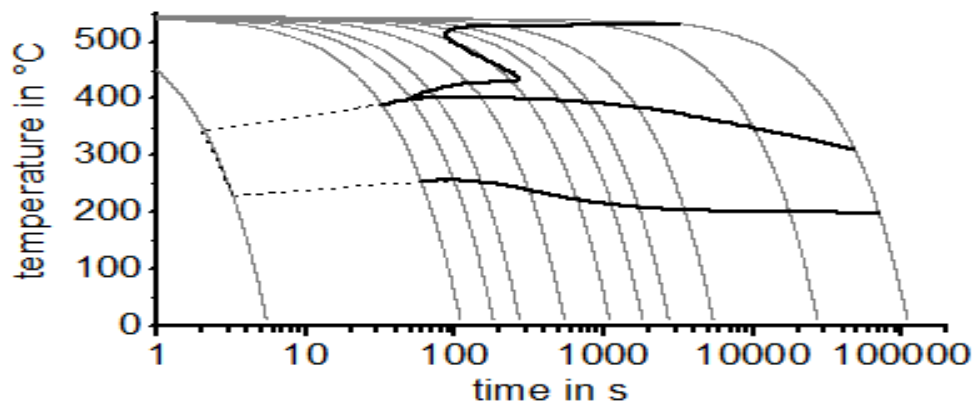


Fig. 1. Continuous cooling precipitation diagram for a common aluminum alloy, showing the start/end of the exothermic reactions, also how they develop with time EN AW 6005A alloy [8].

Depending on the type of aluminum alloy and composition, the CCR can change dramatically (for 6XXX aluminum alloys typically from some 0.1 K/s to some 1000 K/s) [4]. The CCR is commonly obtained from continuous cooling precipitation (CCP) diagrams. One possibility for recording CCP diagrams of Aluminum alloys is given by differential scanning calorimetry (DSC) [3-5, 7, 8, 12, 13]. Due to the fact that modern DSC still has a limited cooling rate range (typically below 10 K/s), aluminum alloys which have CCR higher than the cooling rate

range achievable by the device, cannot be studied. [3, 5, 7, 8]. The problem may be solved by the recently developed differential fast-scanning calorimetry [14-16] reaching cooling rates up to 10^6 K/s. Alloy 7049A, and further series are widely used in the aerospace industry. Due to its high strength, it is normally used for load bearing structures such as beams or spars in aeroplane wings. For this purpose, 7049A tends to be produced as thick plates. It is expected that the surface and centre layers of these thick plates will experience different cooling paths during quenching after solution treatment. Thus the strength in the centre layer decreases dramatically with increasing thickness of the plates. In order to achieve a high strength at the centre, the plates must be cooled as fast as possible to avoid the precipitation of equilibrium phases. However the argument for faster quenching rates is not entirely practical, since both the magnitude of residual stresses and of the distortion that develops in the products tends to increase with increasing rate of cooling.

3 Experimental

3.1 Materials

Aluminum alloy EN AW 7049A (AlZnMgCu) has a high content of alloying elements and precipitation heat is expected to be large. Further this alloy is known to have a high critical cooling rate [15, 27]. It is therefore a good candidate for fast-scanning experiments. EN AW-1050 commercially pure aluminum with an aluminum mass fraction of more than 99.5 % was used as reference material. No precipitation reactions are detectable for this material in the temperature range of interest. EN AW-6063 alloy with a low content of alloying elements and a CCR of about 1.5 K/s was used to test the newly developed reheating method in a conventional DSC, as discussed later. The compositions of the alloys are given in Table 1.

Mass fraction in %	Si	Fe	Cu	Mn	Mg	Cr	Zn	Ti
EN AW-1050 (<i>ref</i>)	0.09	0.32	0.002	0.004	0.001	0.001	0.01	0.004
EN AW-7049A	0.25	0.35	1.90	0.20	2.90	0.22	8.2	0.10
EN AW-6063	0.6	0.35	0.10	0.10	0.9	0.10	0.10	0.10

Table 1: alloying elements contents of the used aluminum alloys.

In Fig. 2 the EN AW 7049A alloy sample is studied.

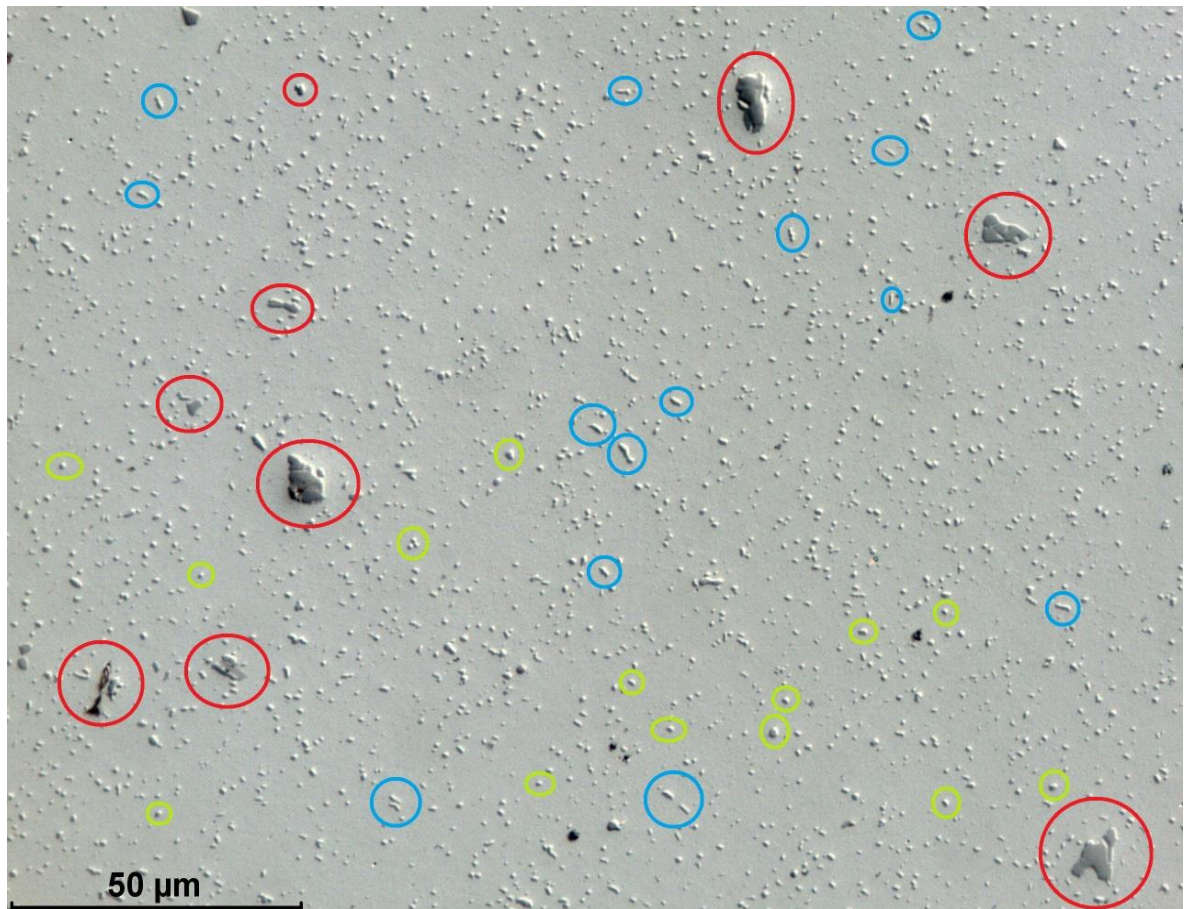


Fig. 2. EN AW 7049A aluminum alloy, reference state microstructure and light microscopy of the sample, primary precipitates – red circles, secondary – blue circle, and acid green circles.

There are several phases which can be clearly determined from this image: big black particles, which have size of about 5 – 15 μm, the smaller and needle like particles, which have sizes of 2- 3 μm, and the spherical bright particles 1- 5 μm in diameter. The very big and black colored particles are the precipitates which come from production of the aluminum, they are intermetallic compounds which have very high melting temperature [28]. Their structures do not change depending on heat treatment.

3.2 Methods

3.2.1 DSC and DFSC devices

Highly alloyed Aluminum materials with high CCR require calorimeters which can cool very fast, in order to be able to follow the rapid precipitation reactions which are taking place inside the materials Fig. 3, Fig. 4. Fast cooling and heating can only be achieved using extremely small samples. Sensors which are used in the differential fast-scanning calorimeters [29],[30] Fig. 5, Fig. 6 are based on silicon nitride membranes, because they have a low addenda heat capacity.

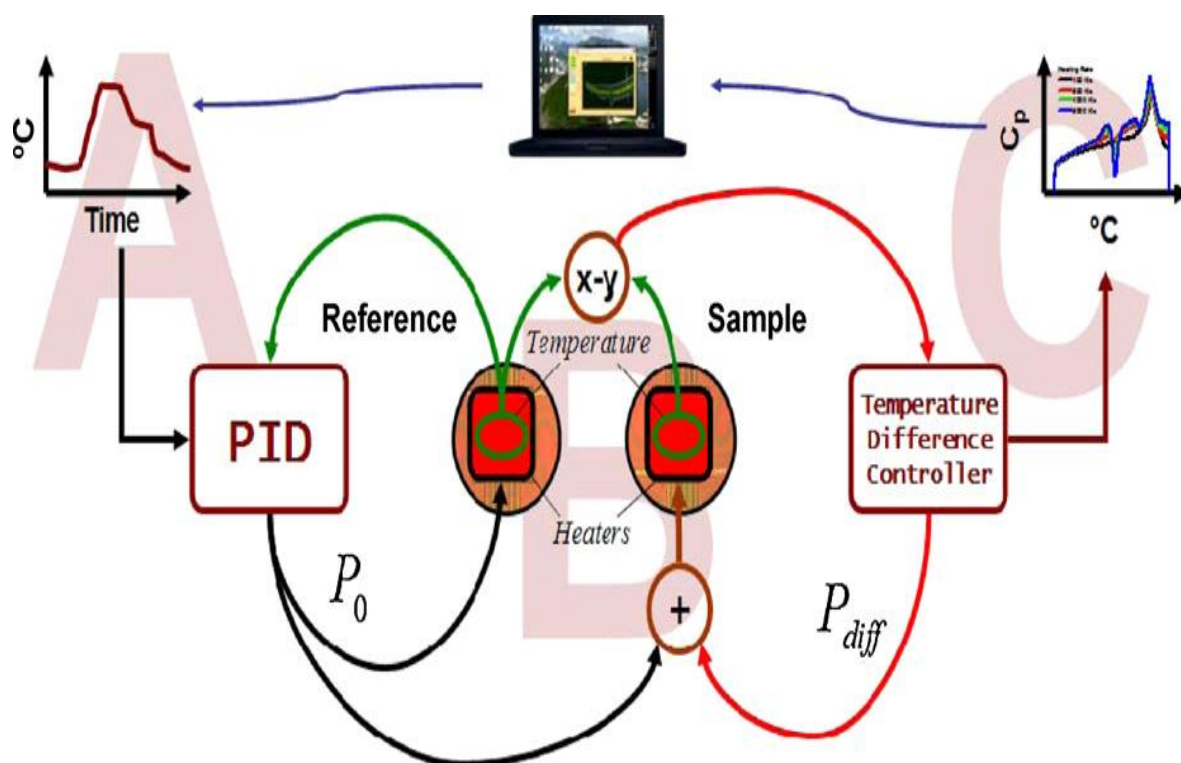


Fig. 3. Scheme of the power compensated fast scanning calorimeter. A, the time-temperature profile is generated by the user and is provided to the PID controller through a DAC board. B, sample temperature is controlled to follow precisely the required profile by means of control loop. C, the resulting temperature difference can be recalculated to heat flow rate and sample heat capacity as shown below.

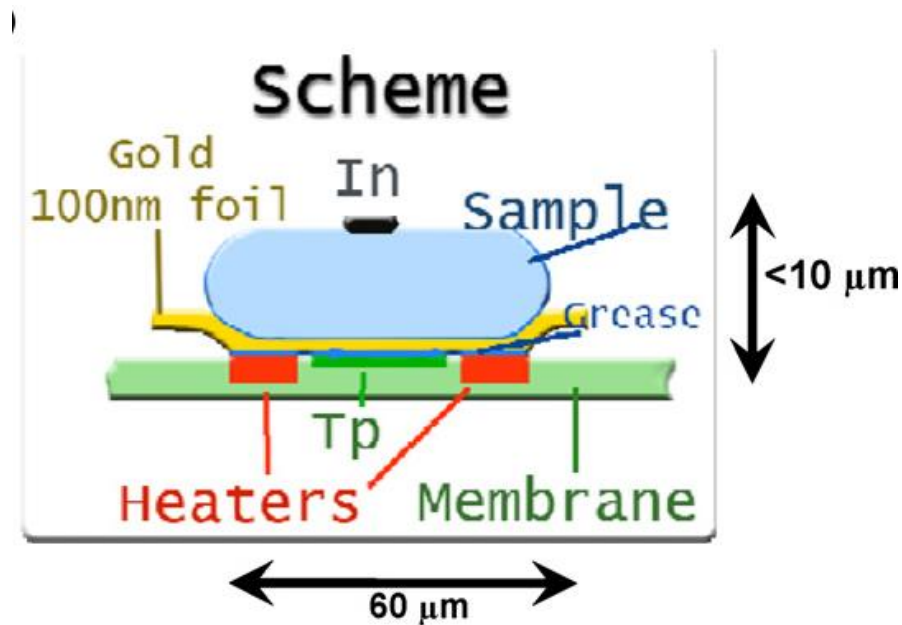


Fig. 4. The sample is placed in the center of the membrane covering the heated area. To homogenize temperature laterally a 100nm thick gold foil is used. Silicon oil is placed in between the gold sheet and the membrane making a good wet thermal contact. Only a small amount of oil, not adding much to addenda heat capacity, stays there due to capillary forces. A similar foil is placed in the same way on the reference sensor. The specified schematics hold for polymers. For alloys the Indium on top is changed to Zinc and the gold foil is also removed for better contact with sensor.

The foil itself ($70\mu\text{m}\times 70\mu\text{m}\times 100\text{nm}$ thick) adds negligibly small addenda heat capacity in comparison with $10\mu\text{m}$ thick alloy sample and the difference between two similar foils is even smaller, ca. 0.5 nJ/K . A small piece of the material under investigation is placed on the gold foil on the sample sensor. After first melting it spreads over the foil and creates a good thermal contact with the foil. The dimensions of the prepared sample should not exceed the size of the heated area. In order to ensure the correct sample temperature measurement and for demonstration purposes a small indium particle was placed on top of the sample.

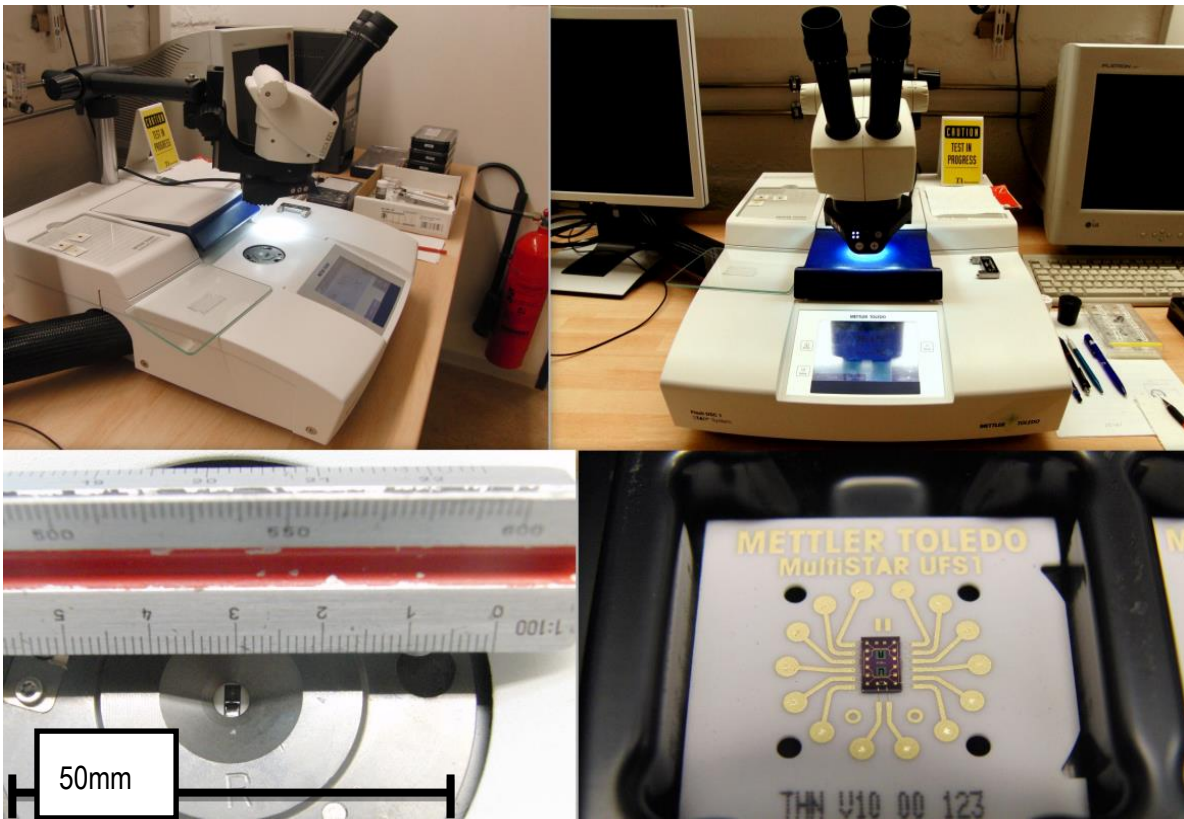


Fig. 5. Mettler-Toledo Flash-1 fast scanning DFSC (left and right top) and the sensor image which is utilizing the device from Xensor Integrations NL.

In Fig. 5 one can see that the high temperature sensor has dimensions of several millimeters. The active area within the calorimetric setup is much smaller and has diameter of a few 100 μm .



Fig. 6. Differential Fast Scanning calorimeter constructed in University of Rostock (Polymerphysik AG). Differential setup Fig. 12 which connects the sensors to the man control unit, where are located PID controllers, signal amplifiers etc.

3.2.2 Sample preparation for the DFSC's

Scanning rates up to 1,000,000 K/s can be realized, but the devices have low sensitivity below 100 K/s [31]. Due to the flat sensor surface, the sample has to be flat too [32], for better contact with the sensor. Samples with the required geometry can be prepared with a scalpel from larger pieces under a microscope Fig. 7, Fig. 8, Fig. 9, in ideal case the ready setup is shown in Fig. 10.

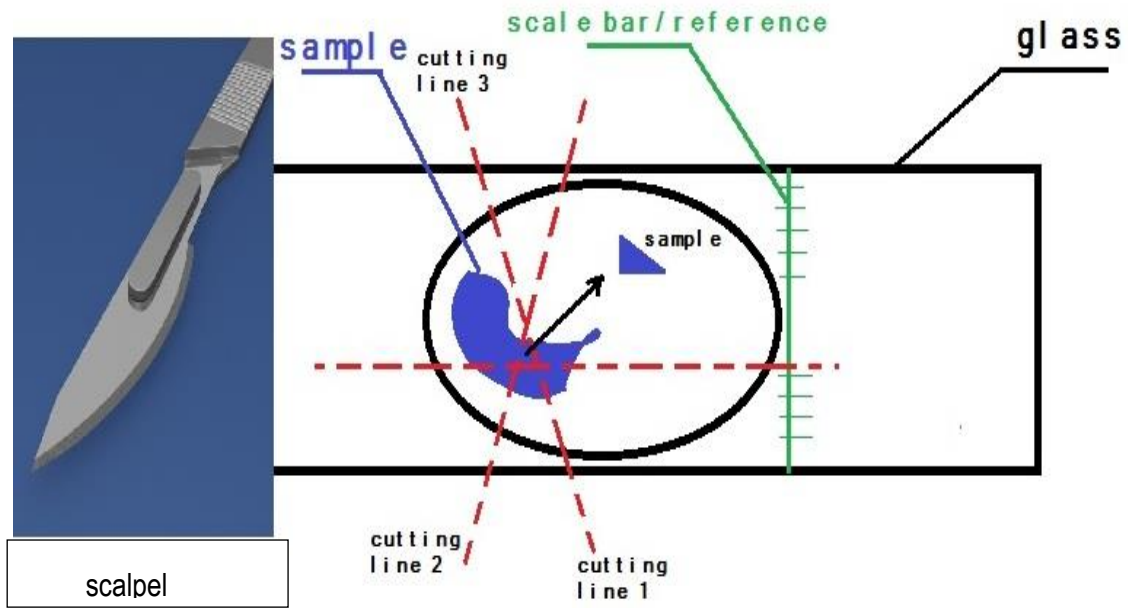


Fig. 7. Sample preparation technique which illustrates how the small samples are prepared, from bulk sample with 3 line cutting method are prepared finer samples for ultrafast experiments. EN AW 7049A alloy samples used.

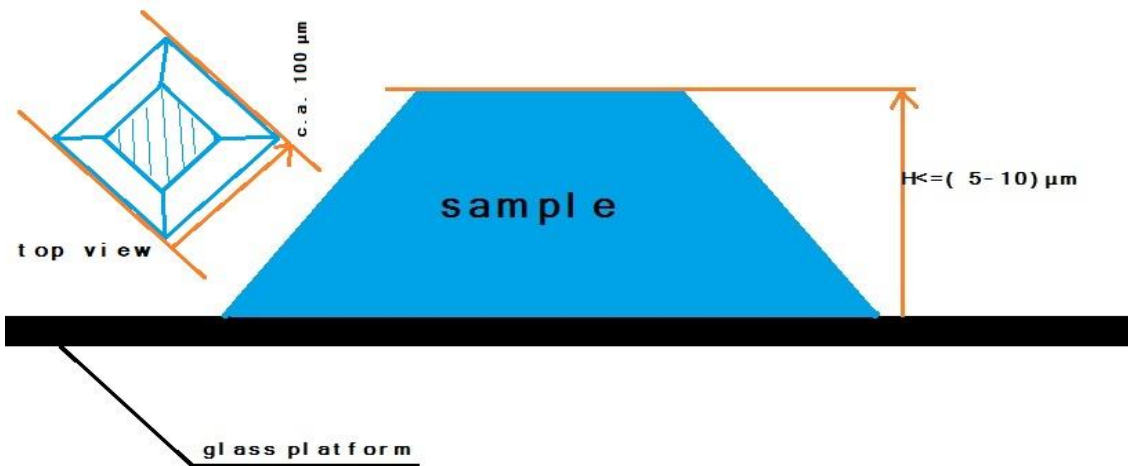


Fig. 8. Side cut of the sample which is prepared and ready for scanning, the ideal sample should have a geometric shape similar to pyramid, with height $10 \mu\text{m}$. Alloy EN AW 7049A is used.

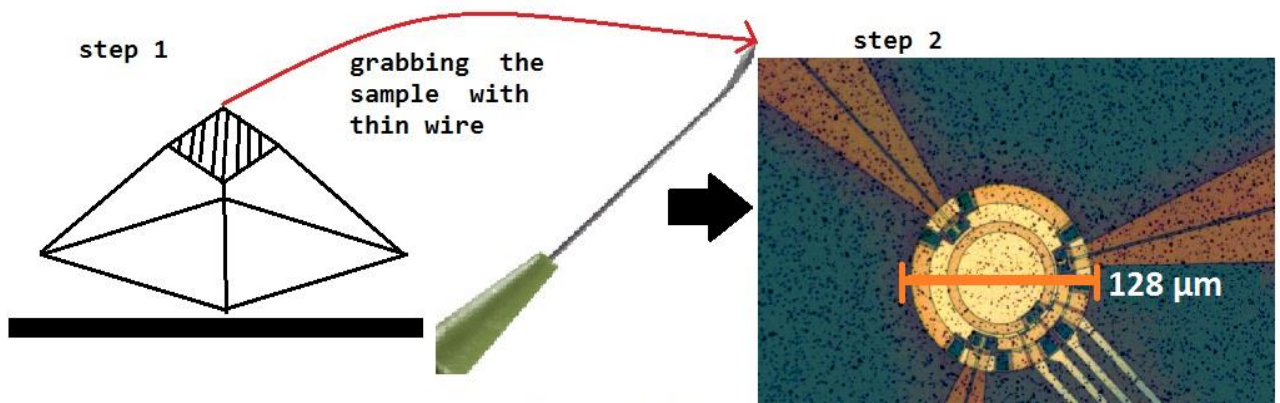


Fig. 9. Finalizing the sample preparation procedure, steps needed to achieve a stable sample for experiments: grabbing the sample with wire and transportation to the sensor active area, later treatment with lubricant for the stability [31]. Alloy type is EN AW 7049A.

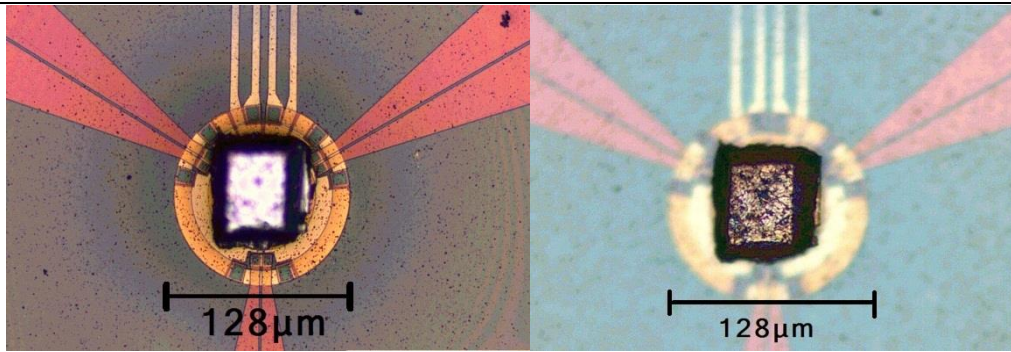
The sample preparation consists of several stages: cutting small piece from bulk material, adjusting the sizes of the sample for the used DFSC sensor, and surface optimization for better thermal contact. Small samples of EN AW-7049A with lateral dimensions (ca. $100 \times 90 \times 20\ \mu\text{m}^3$) were prepared this way and later placed on the sensor surface,

Fig. 10, Fig. 11, Fig. 12 and Fig. 8



(Picture a)

(Picture b)



(Picture c)

(Picture d)

Fig. 10. EN AW 7049A alloy, light microscope images illustrating the sensor structure (picture a,b) and a sample on the sensor (picture b,c), sensor type: XI-377/441 from Sensor Integrations, NL.

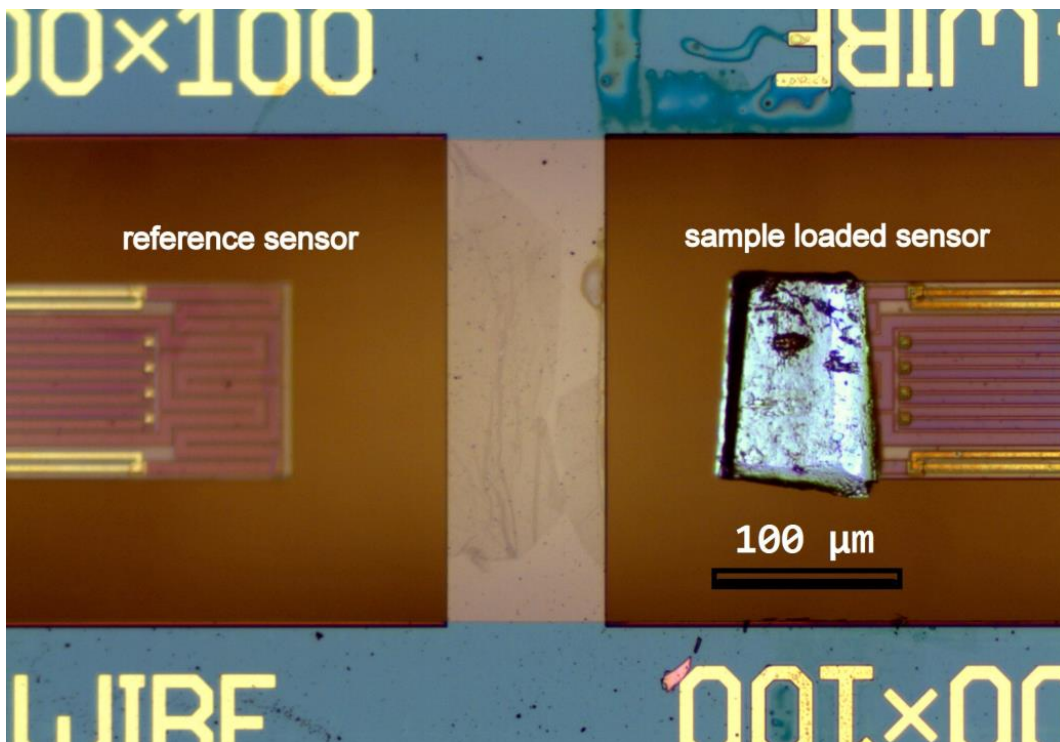


Fig. 11. In this figure, high temperature gold/Platinum coated sensor is represented. From left to right the reference and sample of the EN AW 7049A on the sensor are shown.

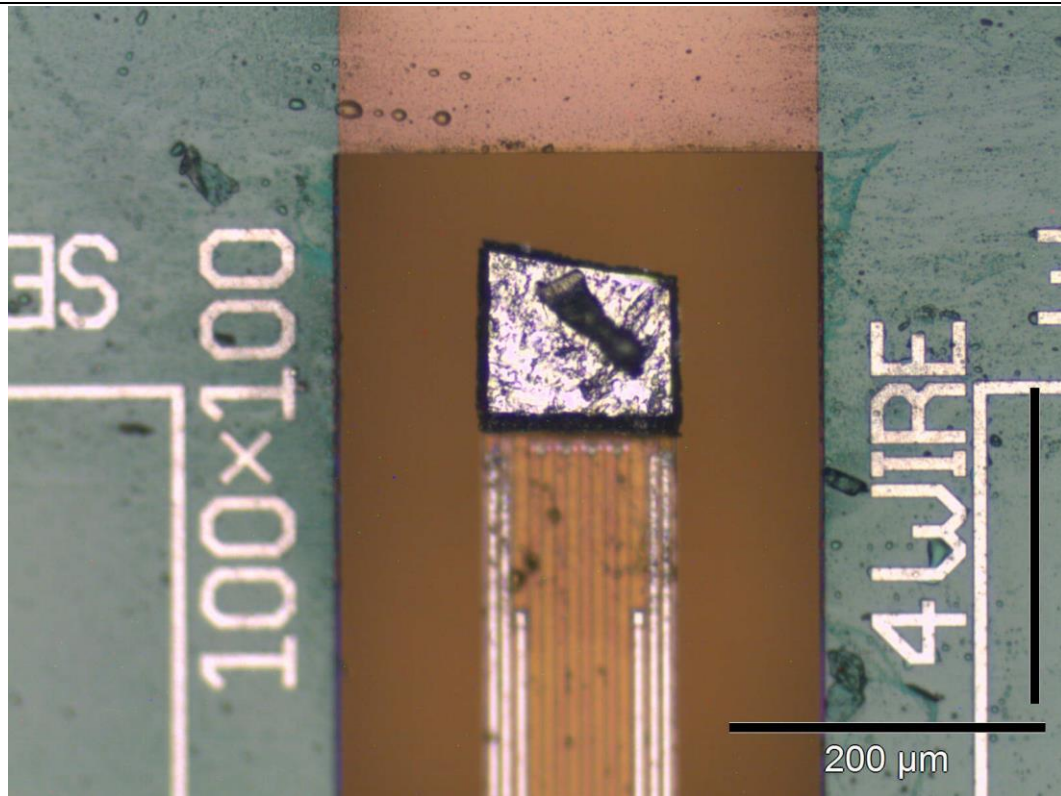


Fig. 12. Sensor with loaded sample of EN AW 7049A and with the reference (Zink) material on top which is used for temperature calibration of the sensor.

After sample preparation the sample loaded sensor and an empty sensor (reference) are connected to the electronic system, which provides the needed power to the heaters of the sensors.

3.2.3 Differential Reheating (DRM) Method

The differential fast-scanning calorimeter is intended to measure the heat flow rate into the sample as the power difference between the empty and the sample loaded sensor during fast temperature scans on heating and on cooling at controlled rates. The power difference is recalculated from the remaining temperature difference between sample and reference sensor. For details of the device see [4, 5, 8, 9]. The device has an effective working range of

controlled heating and cooling in between ($100\text{-}10^6$ K/s). Unfortunately at lower rates (below ~ 300 K/s) the signal to noise ratio is reduced. Very fast analog to digital converters allows very fast data acquisition rates up to some 100.000 points per second, in case that the processes being studied are very fast. In the presented curves always more than 10 points per Kelvin are collected. Fig. 13 shows as an example typical thermal signal from a differential fast-scanning calorimeter experiment data from a high purity zinc sample. The sample was heated and cooled to show how the signal looks like and to check temperature calibration [33]. Fig. 13 shows the remaining temperature difference between reference and sample sensors, which is proportional to the differential heat flow rate, at heating and cooling at 60 K/s. At these low rates the curve is noisy and only the sharp melting and solidification peaks are clearly seen.

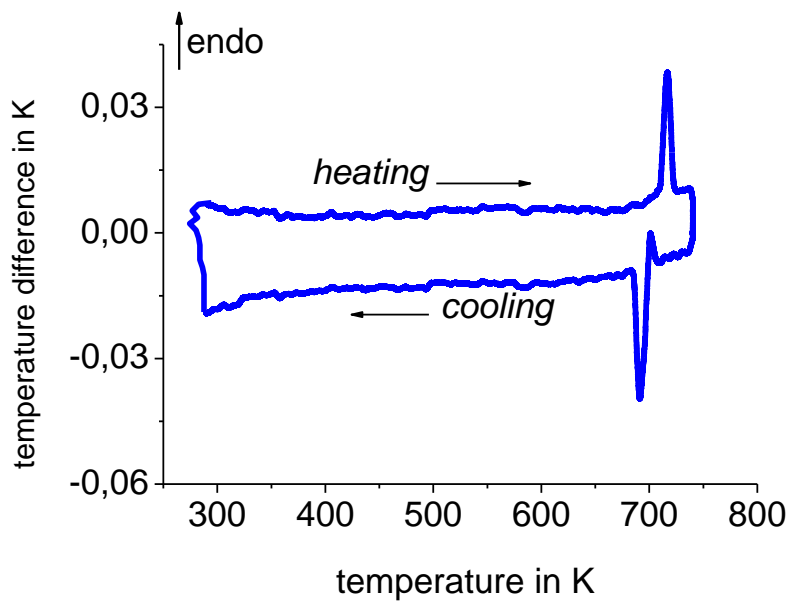


Fig. 13. DFSC heating and cooling scans of a high purity zinc sample showing melting and solidification peaks. The zinc particle (ca. $30 \times 20 \times 25 \mu\text{m}^3$) was placed on the sensor and scanned between ambient temperature and 740 K heating and cooling rate was 60 K/s.

DFSC should allow reaching the critical cooling rate, where precipitation does not occur, even for high alloyed materials. But low sensitivity at lower cooling rates (300 K/s and less) does

not allow distinguishing between noise and very small thermal effects. Nevertheless a sample of the aluminum alloy 7049A shown in Fig. 10(B) was used to check the possibilities of DFSC for determining its critical cooling rate. First, the temperature program of Fig. 14 has been used. The sample is solution annealed at 470°C for 30 minutes and then cooled with different rates.

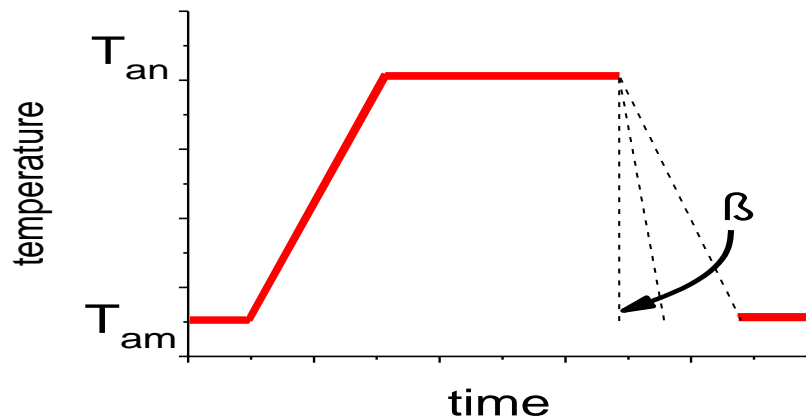


Fig. 14. Program which shows the heat treatment steps, where the sample (EN AW 7049A) is solution annealed and cooled with different rates.

The experimental data gives no useful signals regarding precipitation reactions inside the sample during cooling, Fig. 15. In the investigated cooling rate range between 10 K/s and 300 K/s precipitation reactions of EN AW 7049A were expected because the CCR was estimated to less than 1000 K/s [1]. But the typical exothermic precipitation reactions occurring during cooling are not present in these curves. The reason why precipitation is not seen can be:

- Too low signal to noise ratio (low sensitivity at scanning rates below 300 K/s).
- Insufficient and unstable thermal contact between sample and sensor causing bad signals as seen for the curves at 10 K/s and 100 K/s.

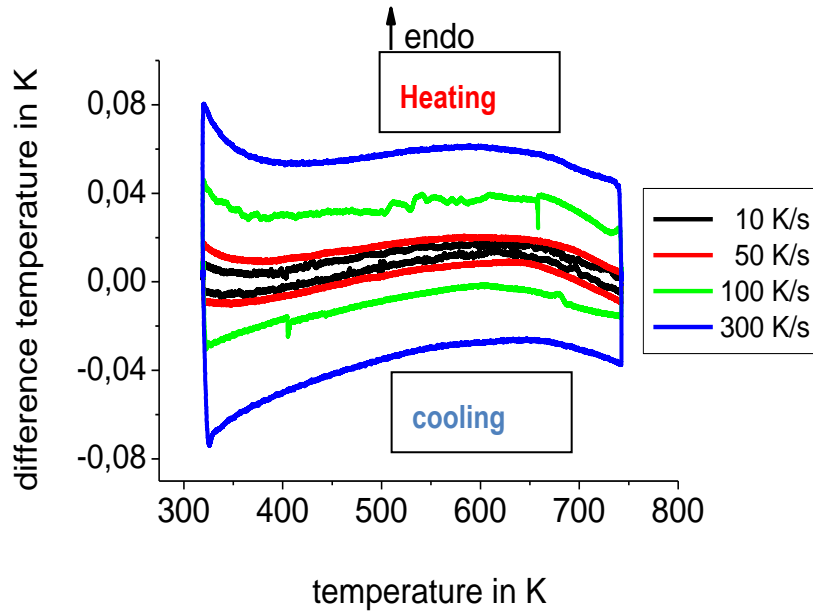
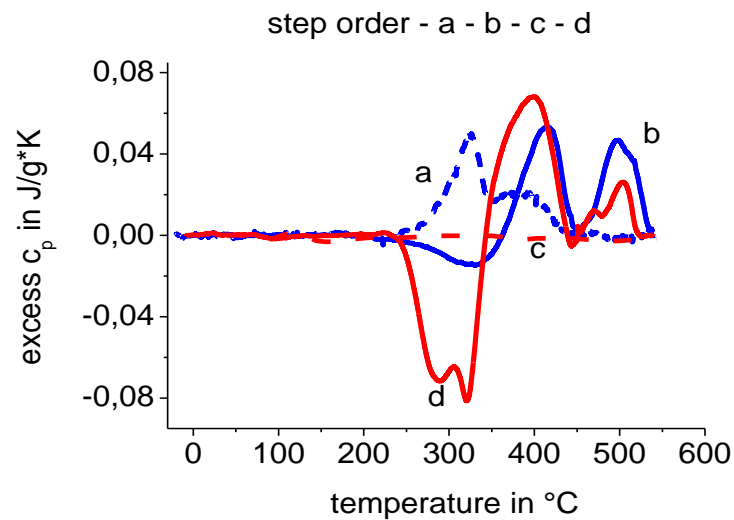


Fig. 15. EN AW 7049A alloy, experiments performed with DFSC. The figure shows heating and cooling scans at different rates.

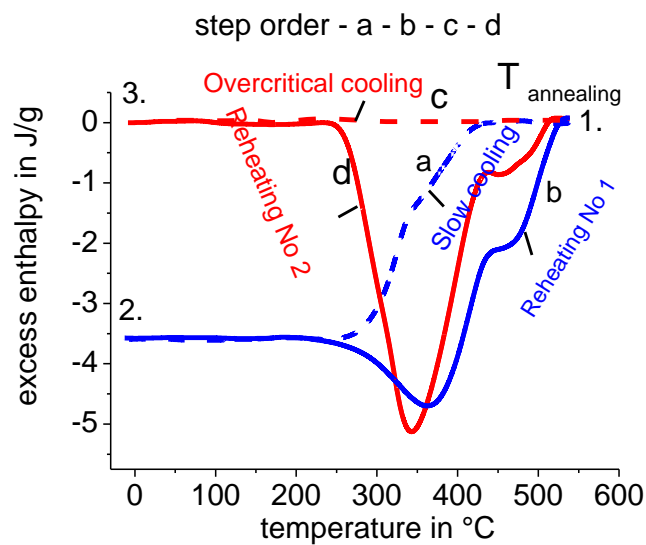
Until now these problems haven't been solved sufficiently. Therefore direct investigations on cooling were stopped and other possible measurement procedures were discussed. One way to overcome the existing technical problems is to study the dissolution of precipitates formed on previous cooling during reheating. In Fig. 16A, excess c_p with temperature for cooling and reheating cycles of an aluminum alloy is shown schematically for relatively fast reheating rates. When the system is slowly cooled from point (1) (solution annealing temperature) precipitation occurs and at point (2) a low enthalpy state is reached. If the sample is reheated immediately after slow cooling back to the annealing temperature (point (2) to point (1)), additional precipitation may occur, but finally all precipitates, including that formed during slow cooling, dissolve.

When the sample is cooled with overcritical cooling rate from point (1) to point (3), during cooling nothing is precipitating, because there is not enough time for nucleation and growth of the precipitates. Immediate reheating from point 3 back to the annealing temperature (point (1)) shows some thermal effects due to precipitation and dissolution on slow heating. The scheme shown in Fig. 16B consists out of two closed loops in temperature – starting and ending at the solution annealing temperature (point (1)). If we assume that independent on the temperature path the same thermodynamic state is reached at the annealing temperature after

reheating (point 1)) then the total enthalpy change for both cooling – reheating cycles equals zero (closed loop).



(A)



(B)

Fig. 16. (A) Measured excess heat capacity curves from Pyris-1 DSC (Perkin Elmer) for the above discussed two closed loops for EN AW 6063 alloy. Curves: (a - blue, dashed) - slow cooling at 0.03 K/s to -20 °C after solution annealing at 540°C for 20 min, (b - blue, solid) - reheating from -20 °C at 0.3 K/s to the solution annealing temperature after (a), (c - red, dashed) - overcritical cooling from 540 °C at 6 K/s to -20 °C, (d - red, solid) - reheating from -20 °C at 0.3 K/s to solution annealing temperature 540°C after (c). (B) Excess enthalpy as a function of temperature from the curves shown in (A).

The enthalpy change on cooling and on heating equals the integral of the heat capacity. As the cooling and reheating processes are taking place in closed loops regarding temperature and enthalpy, one can obtain the total enthalpy changes as the sum of the integrals of the heat capacities of the different parts of the cooling and reheating processes.

Based on a few assumptions we have developed a method allowing determination of precipitation heat on cooling from two reheating scans as detailed next:

Considering a closed thermodynamic cycle where the starting and the end point are in equilibrium, the total enthalpy change equals to zero, eq. (1).

$$\oint H dT = 0 \quad (1)$$

Eq. (1) holds for a closed cycle with slow cooling, when precipitation occurs on cooling, as well as for a cycle where cooling is overcritical. Rewriting the closed loop integral as the sum of the two parts – cooling and heating - one gets

$$\text{for slow cooling} \quad \Delta H_{SC} + \Delta H_{HSC} = 0 \quad (2)$$

$$\text{and for overcritical cooling} \quad \Delta H_{OC} + \Delta H_{HOC} = 0 \quad (3)$$

where ΔH_{SC} - enthalpy change for the slow cooling step, ΔH_{HSC} - enthalpy change for the reheating step No1 in Fig. 17, after slow cooling, ΔH_{OC} - enthalpy change for the overcritical cooling step, and ΔH_{HOC} - enthalpy change for the reheating step No2 in Fig. 17, after overcritical cooling.

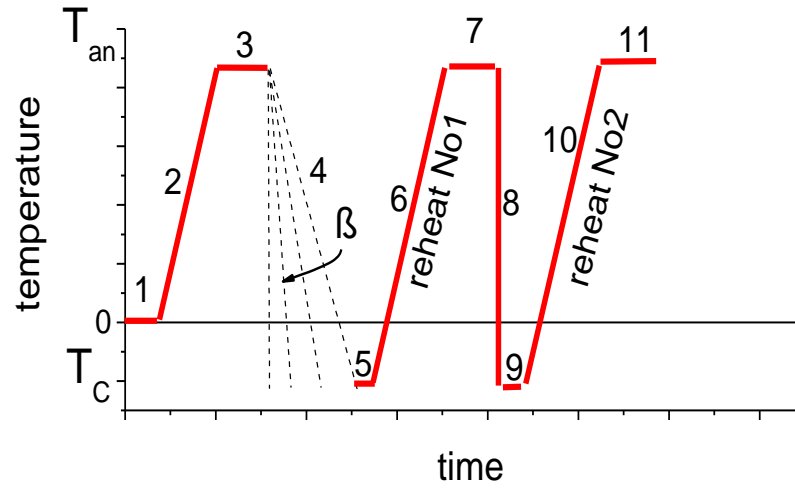


Fig. 17. Modification of the thermal program, consisting of two additional reheating steps after cooling.

Neglecting the contributions from the phononic heat capacity and considering only excess heat capacities as exemplified in [15] one can express the enthalpy terms in equations 2 and 3 as given in equation 4 where T_{an} – solution annealing temperature and T_c – subzero temperature to which the sample was cooled.

$$\text{For slow cooling: } \Delta H_{SC} = \int_{T_{an}}^{T_c} c_{p_{sc}} dT \quad (4)$$

$$\text{For reheating No1 (HSC): } \Delta H_{HSC} = \int_{T_c}^{T_{an}} c_{p_{HSC}} dT$$

$$\text{For overcritical cooling (OC): } \Delta H_{OC} = \int_{T_{an}}^{T_c} c_{p_{OC}} dT$$

$$\text{For reheating No2 (HOC): } \Delta H_{HOC} = \int_{T_c}^{T_{an}} c_{p_{HOC}} dT$$

The corresponding excess enthalpy curves are presented in Fig. 16.

For overcritical cooling, when no precipitation occurs, the excess heat capacity equals zero, see Fig. 16(A), and consequently $\Delta H_{OC} = 0$. The difference of equations (2) and (3) then yields:

$$\Delta H_{SC} = \Delta H_{HSC} - \Delta H_{HOC} \quad (5)$$

where ΔH_{SC} equals the precipitation heat at cooling rates below the critical cooling rate. ΔH_{SC} becomes zero at the critical cooling rate and therefore from ΔH_{SC} as function of cooling rate the critical cooling rate (CCR) is available. Substituting the enthalpy terms on the right hand side by the heat capacity integrals equation (5) results in:

$$\Delta H_{SC} = \int_{T_c}^{T_{an}} c_{p_{HSC}} dT - \int_{T_c}^{T_{an}} c_{p_{HOC}} dT = \int_{T_c}^{T_{an}} (c_{p_{HSC}} - c_{p_{HOC}}) dT \quad (6)$$

The precipitation heat at slow cooling, ΔH_{SC} , is therefore available from the difference of the reheating excess heat capacity curves as expressed in eq. (6). But equation (6) only holds if three conditions are fulfilled:

(i) the cooling starts at a temperature where the sample is in equilibrium and heating ends at the same temperature and equilibrium is reached again. Before cooling, i.e. after solution annealing, equilibrium is reached for most alloys but after reheating, this does only hold if precipitates are highly unstable and fully dissolve during heating. Therefore this approach is valid only for cooling close to critical cooling rate when only small precipitates are formed. Nevertheless, it should allow determining the critical cooling rate.

(ii) The overcritical cooling must be for sure overcritical. Only then $\Delta H_{OC} = 0$ is true and eq. (6) is valid. For the DFSC experiments this will not be a serious problem because cooling rates of at least 100,000 K/s are possible and this should be faster than the critical cooling rate for common aluminum alloys.

(iii) During the isotherm after cooling at the lowest temperature no precipitation occurs. For high alloyed samples this may be a problem particularly after overcritical cooling because then the sample is in a very unstable state. To avoid precipitation at T_c the time spent at T_c should be short and T_c should be as low as possible to slow down precipitation. For the DFSC experiments these conditions are easily fulfilled, the soaking time is of order 0.01 s and T_c can be as low as -170 °C.

It should be mentioned that the above arguments and calculations hold in the same way also for heat capacity (including phononic heat capacity) and not only for excess quantities if

phononic heat capacity is not influenced by the precipitates. Therefore it does not matter if or if not a reference sample compensating for the phononic heat capacity is placed on the reference sensor. Furthermore equation 6 can be applied not only to heat capacity curves but to heat flow data or other measured quantities too, if the same sample and the same heating rate is used for both reheating steps, and the measured quantities are proportional to heat capacity. An example for this is given in [27] and [15] and below.

The temperature time profile used for the differential reheating method is shown in Fig. 16 A first cycle consisting of slow cooling (SC) and first reheating (HSC) and a second cycle consisting of overcritical cooling (OC) and second reheating (HOC) are conducted. The two reheating steps are always performed at the same heating rate to allow an easy data evaluation. The heating rate may be selected according to the instrument used in order to realize maximum sensitivity for reheating. The differential reheating method shown in Fig. 17 compared to the temperature time profile for the direct measurements on cooling as shown in Fig. 14, contains two additional heating steps (Reheat No1 (HSC) and Reheat No2 (HOC)). The excess heat capacity data from these additional steps are finally used to calculate the precipitation heat on slow cooling from equation 6. After solution annealing, (Fig. 17, step 3), first cooling starts (Fig. 17, step 4) and intermetallic compounds may start to precipitate. Depending on cooling rate β_x (fast or slow), precipitation intensity changes. When cooling is fast, the degree of precipitation will be less, [34] or more if the cooling is performed slowly. Overcritical cooled samples are in the metastable state of a supersaturated solid solution, so even at ambient temperature some precipitation can start, violating equation 6. Cooling to sub ambient temperatures (-20°C) avoids precipitation at the lowest temperature, step 5. Afterwards the sample is reheated with constant rate (Fig. 17, step 6) and solution annealed for the same time as before (Fig. 17, step 7). It is assumed, that during this reheating step the precipitates which have been formed during cooling dissolve, showing an overall endothermic effect. As seen in Fig. 16, if precipitation is not complete on cooling, there may be further exothermic precipitation on heating. But for the applicability of the reheating method this is not important. During the next step (Fig. 17, step 8) the sample is subjected to overcritical cooling, this means that the precipitation reactions are fully suppressed. In this step the sample is cooled also to sub ambient temperatures, step 9. The last step (Fig. 17, step 10) reheating No2 is exactly the same as step 6. Further subtracting the excess specific heat capacity curves or other measured quantities like heat flow rates of the reheating No1 (HSC)

in (Fig. 17, step 6) and reheating No2 (HOC) in (Fig. 17, step 10) one can calculate the precipitation enthalpy during step 4 according equation 6.

We checked the applicability of the method with DFSC on precipitation of the aluminum alloy EN AW 7049 A. According the recommended solution annealing conditions for this alloy T_{an} was chosen as 470 °C and t_a as 30 min [9]. Cooling rate was varied in the range from 1 K/s up to 5000 K/s. For the second overcritical cooling step in the scheme of Fig. 17, a cooling rate of 5000 K/s was chosen. The two reheating steps were performed at 1000 K/s, the optimum heating rate for this sample. Heating starts after an equilibration time of 0.05 s at 25 °C. The experimental data, using this method is presented in Fig. 19.

For these experiments the phononic heat capacity was not compensated by a pure aluminum sample on the reference sensor. Consequently, overcritical cooling does not yield $\Delta H_{OC} = 0$.

But as briefly discussed above the additional contribution to the measured heat capacity is present in the first reheating too and is canceled out by the subtraction of the second heating scan. The resulting difference curves (first heating – second heating) are shown in Fig. 19. With increasing cooling rate in step 4 of Fig. 17 the difference between the two reheating steps decreases and eventually vanishes. Although these data are only qualitative they verify applicability of the reheating method to obtain information about the precipitation processes in aluminum alloys at cooling.

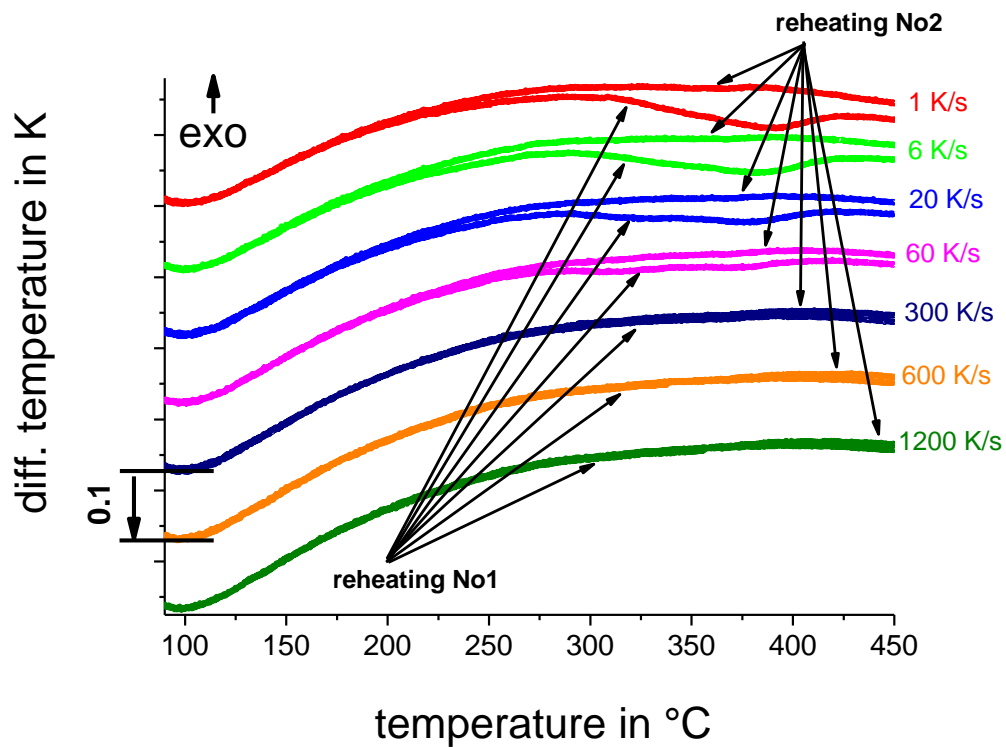


Fig. 18. EN AW 7049A alloy, experiments applying the differential reheating method as described in Fig. 17; first and second reheating vs. sample temperature. The sample was heated to solution annealing temperature 470°C held isothermally for 30 min and cooled to ambient temperature with different rates shown in the graph, and then reheated both, first and second, with 1000 K/s rate to solution annealing temperature.

As known from other aluminum alloys [1], precipitation during cooling proceeds by at least two reactions in different temperature intervals. These two reactions seem also to be visible during reheating of EN AW 7049A, especially after cooling rates in the range 1 - 10 K/s. Two partially overlapping peaks occur. The heating rate of 1000 K/s used for the DFSC experiments do not allow further precipitation on heating, but only dissolution. Consequently, the precipitates formed on cooling are dissolving according their stability and size in two distinct temperature ranges.

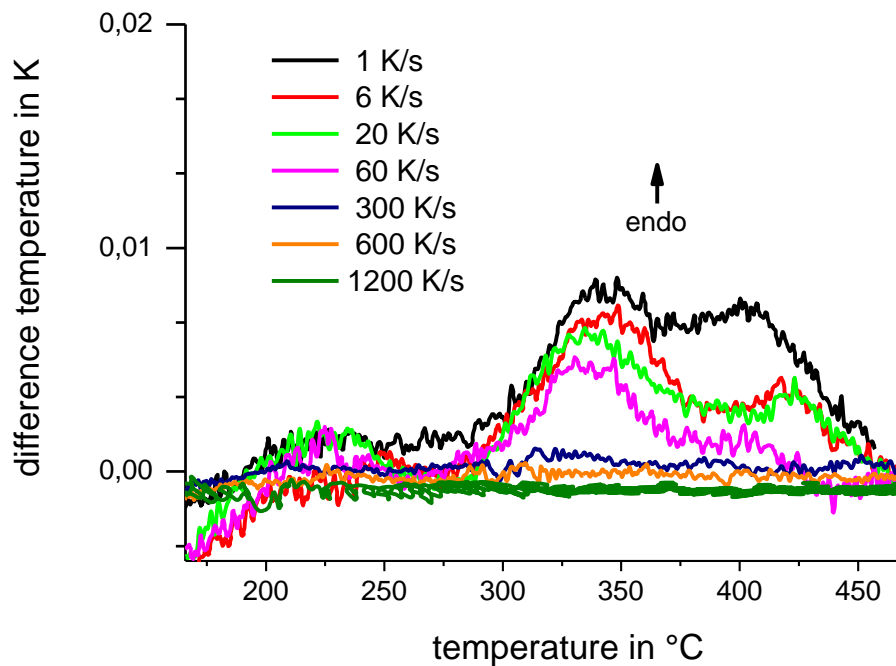


Fig. 19. EN AW 7049 A alloy, results from differential reheating showing the difference between first and second heating as shown in Fig. 18. The sample was solution annealed at 470° for 30 min, then cooled with the indicated rate to ambient temperature and reheated with 1000 K/s rate for both heating to solution annealing temperature. Cooling rate for the step 8 equals to 5000 K/s.

The integrals (peak area) over the temperature difference curves shown in Fig. 19 provide a qualitative measure of the precipitation heats on cooling and are shown in Fig. 20. The area decreases with increasing cooling rate. For cooling rates above 300 K/s the difference to the overcritical cooling curve at 5000 K/s approaches zero within the error limit of the measurements. For the experimental conditions used here, which are quite unsecure regarding solution annealing temperature (± 10 K), the critical cooling rate for the EN AW 7049 A alloy is estimated to 300 K/s. This is in good agreement with critical cooling rates of other high alloyed 7XXX aluminum alloys (7075, 7178) determined by tension tests in the T6 state after quenching with different rates [4, 6, 8, 9, 13, 14, 20, 35].

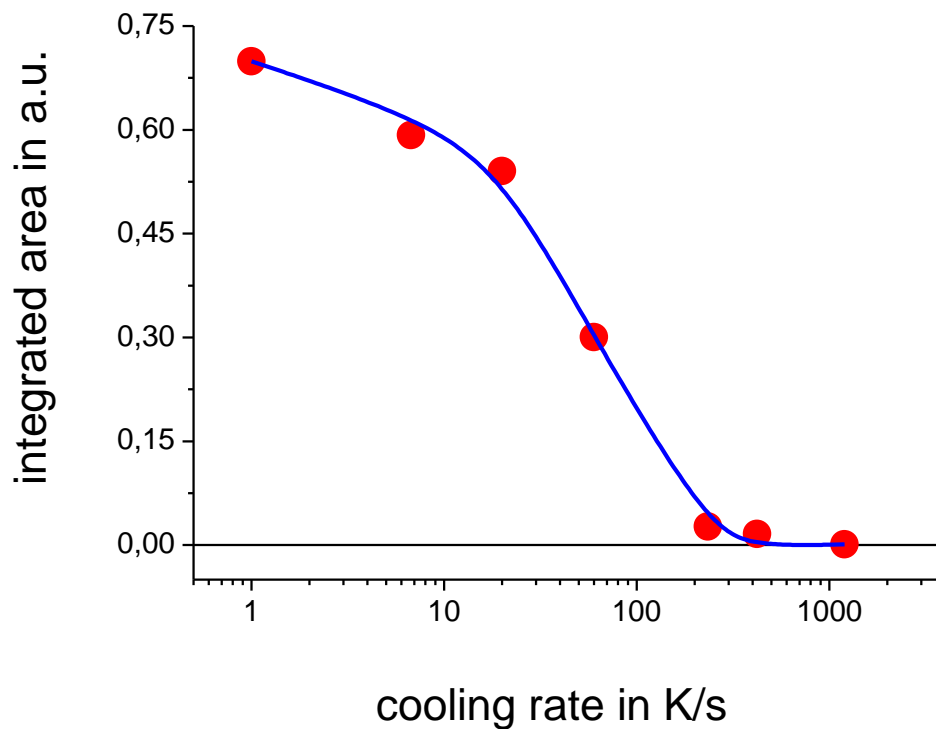


Fig. 20. EN AW 7049A alloy, Integration of the curves in Fig. 19. The line is a guide to the eyes only.

From this proof of concept DFSC experiment we conclude that precipitation reactions are traceable at cooling rates far beyond the limits of conventional DSC (ca. 10 K/s) by the newly developed differential reheating method in combination with the DFSC. Nevertheless, before further using the DFSC reheating method the validity of the basic assumptions as mentioned above must be checked on a quantitative basis.

3.3 Trustworthiness of the Differential Reheating Method (DRM)

For a quantitative check of the reheating method it is useful to compare data from reheating with direct measurements of the precipitation heat on cooling. Precipitation heat on cooling is available from DSC as shown in [4, 5]. For the alloy EN AW 7049A, used for the DFSC experiments, the differential reheating method is not applicable at DSC cooling rates (< 10 K/s), because cooling cannot be realized at overcritical cooling rate (> 300 K/s). But there are other aluminum alloys with a much lower CCR available, which can be used for testing the differential reheating method in a DSC. In [4, 5, 9] it was shown that the aluminum alloy EN

AW 6063 has a critical cooling rate (CCR) of about 1.5 K/s. Because the available DSC allows cooling up to 3 K/s, step 8 in Fig. 17, can be realized at overcritical cooling rate for this alloy.

For checking the differential reheating method according Fig. 17, experiments with the low alloyed aluminum alloy EN AW 6063 have been performed employing a PerkinElmer Pyris-1 power compensation DSC. For this alloy the complete set of precipitation enthalpy data on cooling from slow to overcritical cooling rates are available [5, 9] and allow a quantitative comparison with the data from reheating. The validation of the reheating method consisted of:

- Determination of the optimal reheating rate for the aluminum alloy EN AW 6063 in the DSC.
- Reheating (with optimal reheating rate) of the aluminum alloy EN AW 6063 samples following the temperature program of Fig. 17 and varying cooling rate in step 4 from 0.01 K/s up to 3 K/s.
- Calculation of the specific precipitation heat from the excess specific heat data out of the two reheating steps according Eq. (6).
- Comparison of precipitation heat obtained directly on cooling and from the differential reheating method.

First, the optimum heating rate for the temperature profile of Fig. 17 was determined for the employed DSC and the alloy under investigation. Fig. 21 shows the first reheating (step 6, in Fig. 17) of the aluminum alloy EN AW 6063 at different heating rates starting from 0.1 K/s up to 1 K/s. The cooling (step 4 in Fig. 17) in these experiments was kept constant at 0.5 K/s, to observe the influence of the reheating rate. The graph shows that several reactions occur during reheating. At the highest heating rate (1 K/s) the high temperature reaction shifts to higher temperatures and probably does not finalize during the scan, violating the condition of a closed loop in enthalpy as discussed above. But with slower reheating (0.1, 0.3 and 0.5 K/s) the reactions finalize until the end of the scan. This is indicated by the close to zero excess heat capacity at the end of the scan at high temperatures and the shape of the high temperature flank of the high temperature dissolution peak. From the curves shown in Fig. 21 an upper limit for the heating rate of 0.5 K/s is determined. Obviously a lower heating rate would be better because the dissolution peaks are shifted to lower temperatures but the optimum rate

has also to be chosen considering the decreasing signal to noise ratio at lower rates. Summarizing, the chosen heating rate must be slow enough to allow all dissolution occurring during the heating scan and it must be fast enough to achieve a good signal to noise ratio. Both conditions are fulfilled at 0.3 K/s heating rate. All reheating experiments (Steps 6, and 10, in Fig. 17) were therefore performed at this rate. For all experiments only one sample of EN AW 6063 was used several times. The reproducibility of the measurements was checked by repeating the experiments after cooling at 1 K/s before and after all other experiments.

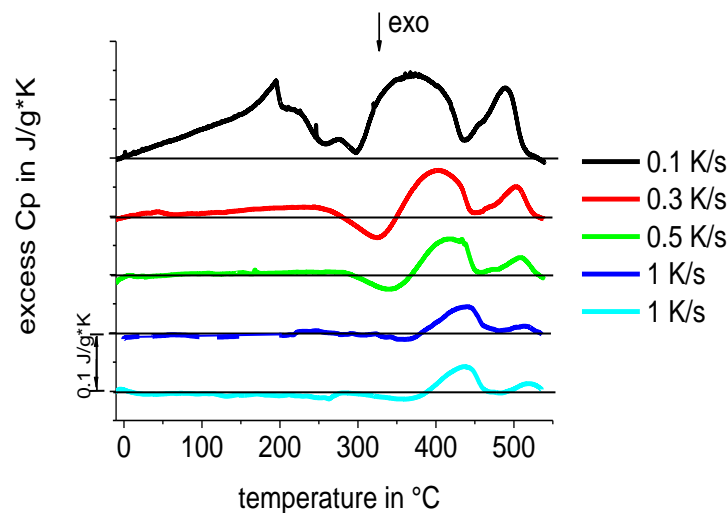


Fig. 21. EN AW 6063 alloy, influence of the reheating rate during first reheating. Sample was subjected to solution annealing at 540 °C for 20 min, then cooled with constant rate 0.5 K/s and then reheated with the rates given in the figure. The two curves with 1 K/s reheating were collected before (blue) and after all other measurements (bottom cyan curve).

The EN AW 6063 sample was reheated after cooling with optimal reheating rate Fig. 21 up to its solution annealing temperature of 540 °C and kept there for 20 minutes every time. The quenching rate was changed from 0.01 K/s to 3 K/s. The sample was quenched to low temperatures (-20 °C) to avoid precipitation at ambient temperatures.

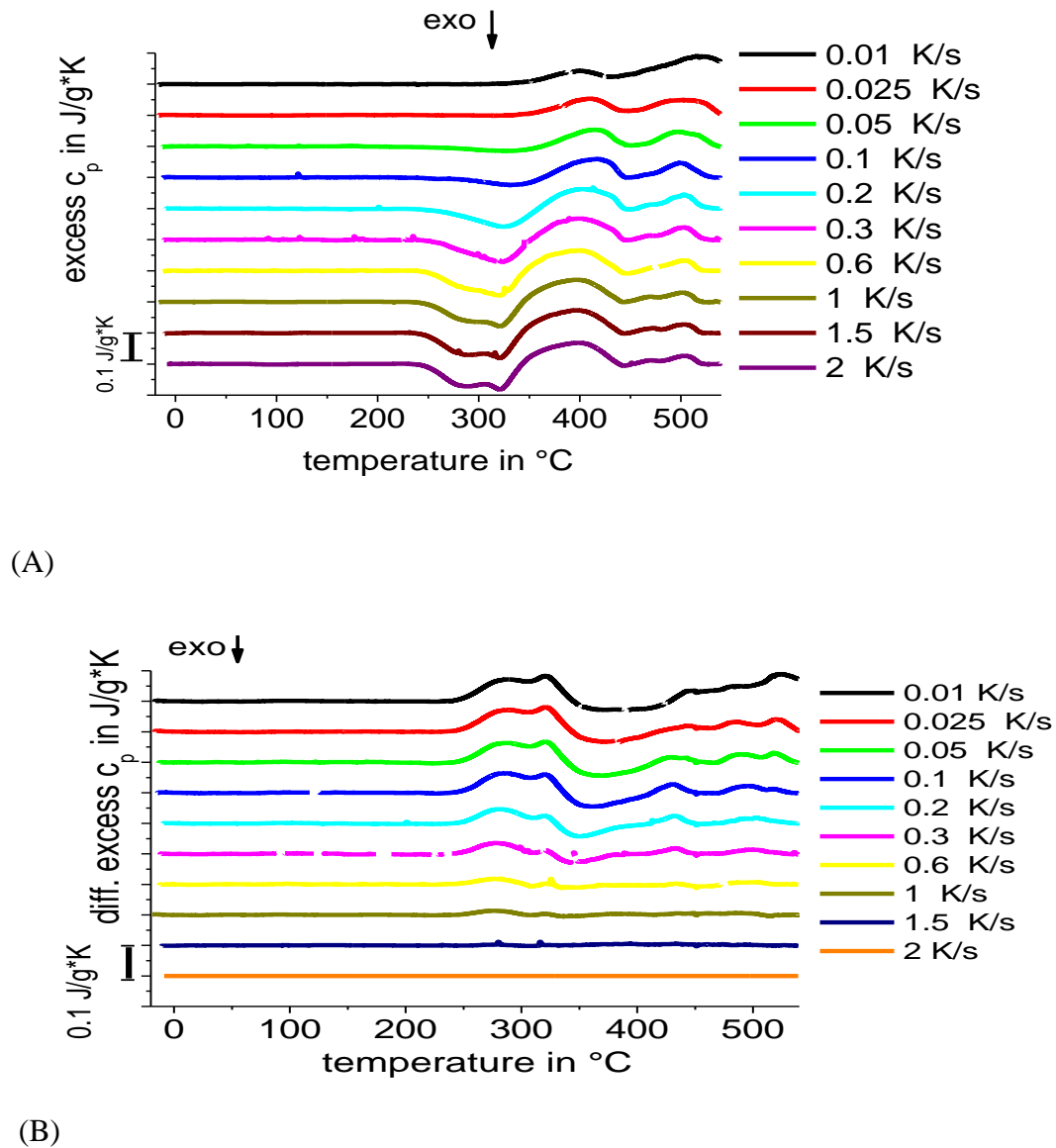


Fig. 22. EN AW 6063 alloy, precipitation/dissolution reactions during first reheating after cooling with different rates (A). Sample was solution annealed at 540 °C for 20 min then cooled with the indicated rates and then immediately reheated with 0.3 K/s. For the differential reheating method (B) the difference between the measured curves in (A) and the reheating curve after overcritical quenching with 2 K/s are shown. The dissolution reactions visible in (B) are decreasing and finally disappear with increasing cooling rate.

In Fig. 22 the reheating of the aluminum alloy EN AW 6063 with various quenching rates is presented. As expected the reheating curves are depending on precipitation during cooling. After lower cooling rates only endothermic peaks are seen in the reheating curves. After faster

cooling, first an exothermic precipitation peak at reheating is seen. This peak corresponds to precipitation of the alloying atoms not precipitated on fast cooling due to kinetic limitations. It is particularly pronounced at rates near to the critical cooling rate (1.5 K/s). For reheating after very slow cooling the high temperature dissolution is not finalized. At slow cooling very large precipitates are formed which on heating need relatively long time to fully dissolve. Therefore the method only works for the curves after cooling from 0.1 K/s up to 2 K/s and faster.

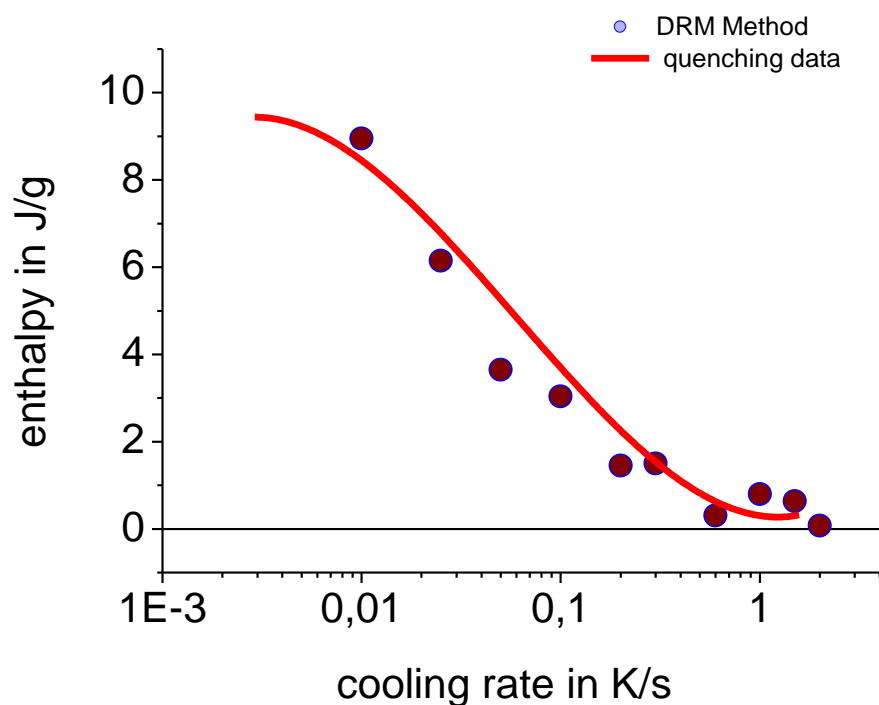


Fig. 23. EN AW 6063 alloy, excess enthalpy from integration of the differential excess c_p curves in Fig. 11 (B) as function of previous cooling rate. Sample was solution annealed at 540 °C for 20 min then cooled with various rates to -20 °C, and reheated with 0.3 K/s. The solid line shows the precipitation enthalpy from cooling data for the same alloy system from [4].

The total specific precipitation heat of the reactions on cooling was determined according equation 6 from the curves shown in Fig. 22(B) above. The change in precipitation enthalpy

as function of previous cooling rate is shown in Fig. 23. The precipitation enthalpy is high at very slow cooling rates, and becomes small, finally zero at critical cooling rate. The alloy EN AW 6063 has a critical cooling rate of about 1.5 K/s. Therefore the precipitation reactions have been suppressed fully on cooling at higher rates and the integral over the excess specific heat at differential reheating became zero too.

For the alloy EN AW 6063 the precipitation heat on cooling is directly accessible by DSC [15]. Fig. 23 shows, for comparison, the precipitation heat on cooling as a solid line. The comparison of the quenching experiments, and reheating data fit perfectly showing that the reheating method can be used quantitatively to determine precipitation heats on cooling.

The new differential reheating method presented here, can be used to characterize the precipitation process during previous cooling of aluminum alloys. The advantages of this method are the following:

- Precipitation monitoring up to critical cooling rate region even for high alloyed aluminum alloys with high critical cooling rates seems to be possible by applying fast scanning calorimetry, e.g. DFSC [23, 36, 37]
- Precipitation enthalpy can be assessed from heating scans collected at optimum experimental conditions without collecting data from the previous cooling step at varying cooling rate.

The prerequisites to be fulfilled for the successful application of the reheating analysis are:

- (i) a reheating curve after overcritical cooling must be available as a reference curve, and
- (ii) the dissolution of the precipitates must be finalized during the heating scan.

The later condition limits the applicable heating rates as well as the lowest cooling rates because of the stability of the precipitates. But the differential reheating method allows the determination of the critical cooling rate probably for any available aluminum alloy.

3.4 Recording of the precipitation reactions by conventional DSC

The analyses were performed with age-hardening Al-Mg-Zn-Cu wrought alloy EN AW 7049A. The samples were solution annealed and cooled in three different types of DSC calorimeters. Following the procedures described in [5].

- Ultra-slow heat flux DSC (Setaram 121)
- DSC Mettler-Toledo 823e
- Power compensation Hyper DSC (Perkin-Elmer Pyris-1)

3.4.1 Conventional DSC sample preparation

- The samples have cylindrical shape and are taken from extruded profile. The sample masses vary from 600 – 1700 mg, with typical dimensions of 4 – 6.5 mm in diameter. The samples were covered with standard 300 μ l aluminum crucibles with a mass of about 360 mg, Fig. 24.
- Mettler-Toledo 823e DSC samples have been taken from the extruded profile. The sample masses are in range of 39 – 60 mg with typical dimensions of ~ 1 mm in length and 3-5 mm in diameter, respectively.
- Hyper DSC samples have been taken from the extruded profile. The sample masses are in range of 90 – 180 mg with typical dimensions of ~ 1 mm in length and 3-5 mm in diameter, respectively for the Perkin – Elmer Pyris -1 DSC, Fig. 24.



Fig. 24. Comparison of the samples (EN AW 7049A) used in different DSC machines, as described above the dimensions vary significantly depending on type of DSC.

Heating was carried out at 5 K/min. The temperature of the block, (block is a part in DSC measuring unit responsible for cooling) was set to 15 °C. The reference sample was turned from cast block. The detailed amount of alloying elements is shown in table No1. The above mentioned EN AW 1050 aluminum alloy was used as a base reference material for all of these experiments. Steps 1-3 are the solution annealing steps, the 4th step of the thermal program so called cooling step ‘quenching’ step was varied starting from very slow (near to equilibrium) up to very fast rates where normally the reactions are suppressed. The same sample later were taken out and naturally aged in T4 mode. The purpose of this was the hardness investigation as well as various metallographic testes for comparison with the data acquired from different DSC’s [6, 35, 38, 39].

The conditions for heat treatment were equal for all the samples inside any kind of device. The data regarding solution annealing, temperature, e.g. time are provided below:

- Solution annealing temperature $T_{\text{annealing}} = 470 \text{ }^{\circ}\text{C}$
- Solution annealing time $t_{\text{annealing time}} = 30 \text{ min}$
- Natural aging was performed at room temperature (24°C) for 30 days
- Excess Specific Heat Capacity was calculated from all experiments

It is important to mention that for the excess specific heat calculation baseline (blank experiment) is needed to be performed each time. In this case the reference material mentioned above was used. The difference between specific heat capacity of EN AW 7049A and EN AW 1050 was calculated.

The slowest experiments were done with a Heat-Flow-DSC of CALVET-type (Setaram DSC 121). The optimal samples have dimensions of about 5.7 mm in diameter and 21.7 mm in length, which results in a sample mass of approximately 1570 mg. The samples were covered by standard aluminium crucibles with a mass of about 360 mg. Heating was carried out at 0.08 K/s. The block-temperature was set to 15 °C, but rises up to 30 °C when the furnace reaches the maximum temperature of 540 °C. Cooling power of the circulating bath was not high enough to keep cooling jacket temperature at 15 °C but this is not important for this type of instrument. The device cooling rate range is in between 0.0005 – 0.2 K/s.

The cooling rates in the intermediate range from 0.1 K/s to 0.5 K/s were performed employing the heat flow type Mettler Toledo DSC 823/822. The optimal samples for these rates and this device have typical dimensions of about 5.4mm in diameter and 1.4 mm in height, which results in a sample mass of approximately 96 mg. The samples were placed in standard aluminum crucibles with mass of about 50 mg. These crucibles have a positioning pin for exact and equal positioning on the measuring block. These crucibles are tightly closed via crimping press designed for that purposes. In each crucible a small hole was made to avoid

buckling. Due to buckling the heat flow to the sample can be altered and therefore some fluctuations may result in the experiments. The buckling may result because of air expansion over a wide temperature range used for the investigations. Heating was performed with suitable rate of 0.5 K/s. Inside the Differential scanning calorimeter for keeping neutral and non-aggressive atmosphere pure nitrogen purging was used all the time. Cooling was realized by a double-stage mechanical cooler.

The fastest DSC which was used in this range was the Perkin Elmer Pyris-1. This type of DSC has a typical power compensation scheme. The sample dimensions are in range of 4 mm in diameter and 1 mm in height. This dimensions result a sample mass of about 30 mg. These sample where placed inside pure aluminum crucibles from Perkin-Elmer in order to avoid the elemental contamination of the microfurnaces of the instrument. Because of the high temperature there is diffusion from sample to the furnace, and this can result into a serious malfunctioning up to short circuiting. There is an important point connected to this DSC, when is needed to achieve maximum highest rates possible. The guard rings which are in between furnace and cooling block should be changed from star shaped to massive metallic ones.

The baseline drifting discussed in figure Fig. 25 was solved via several measurements. Two baseline measurements where performed each time, one before sample scanning, and one after. Radiation and its role are huge especially for DSC technique. The baseline, as well as many other parameters can change due to this phenomenon Fig. 25. Strong change in color can be observed in all samples, the change takes place after each experiment and results into black color in the end. This extensive change is related to surface reactions. The massive change in color is much stronger in samples with high alloying content, because the high alloying elements concentrations results in more intensive reactions which lead to color changing. All these effects have been studied by B. Milkereit et al. in detail.

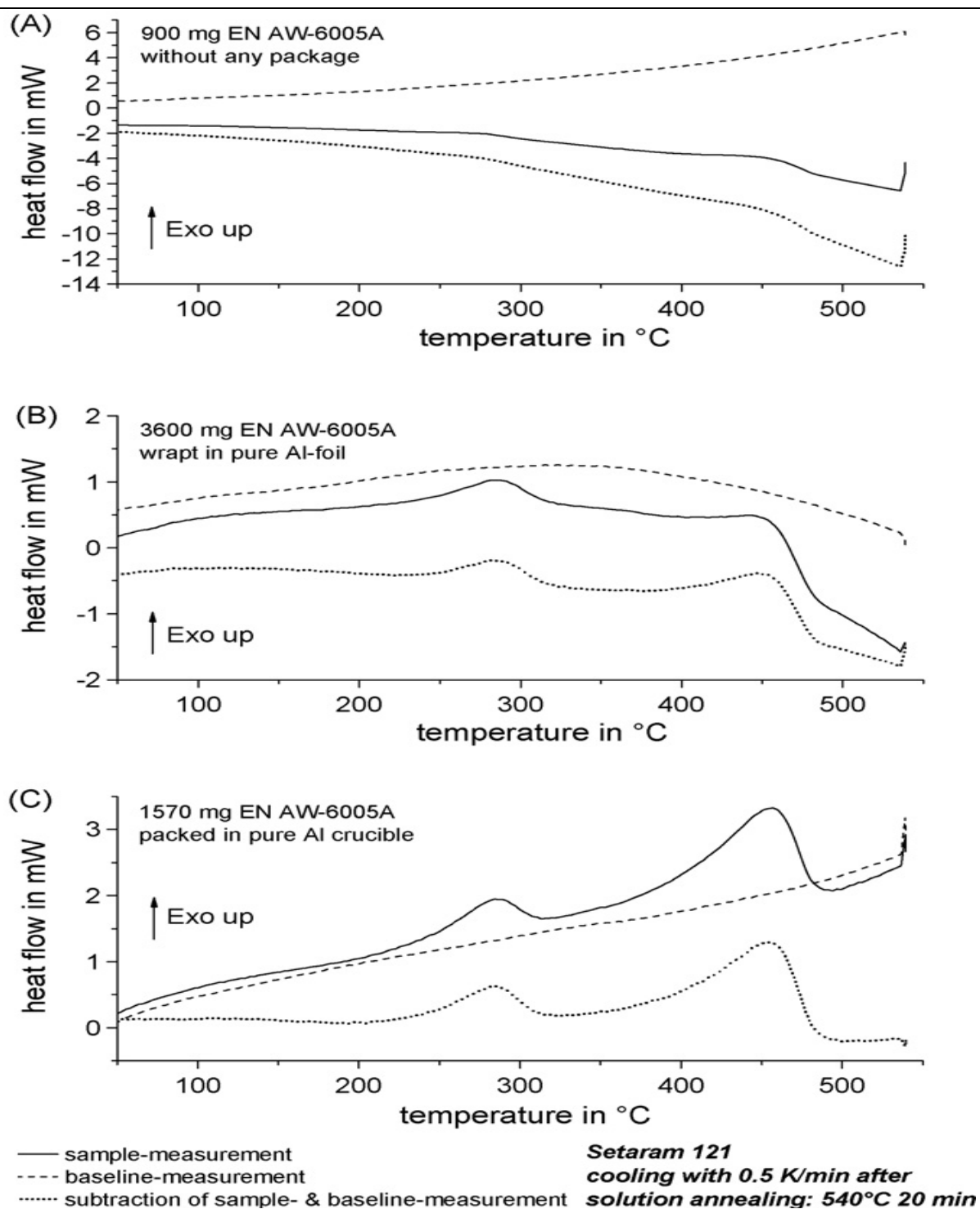


Fig. 25. Bending and its correction proposed [5] by B. Milkereit et al. show how it is important to take this into consideration in order to have precise enthalpy determination Comparison of different samples-packaging in the Heat flow DSC of Calve Type (Setaram 121), A – no packing, B – 40 mg pure aluminum foil, and C- 360 mg pure aluminum crucible.

3.4.2 Sample preparation for metallographic, SEM+EDX and hardness analysis

Scanning electron microscopy analyses were performed with the samples obtained from the various DSC devices. These samples were used mainly to obtain the needed microstructural analysis. The samples taken from DSC were aged directly after cooling for 30 days at room temperature. Then the samples were placed into cold epoxy resin and left for hardening for 24 hours. The samples in Fig. 26 were ground and polished with OPS suspension alcohol, the exact chemical formula is 4g Kalium Permanganate in 100ml plus 1g NaOH for 20 – 25 minutes. After etching the samples are polished again shortly. Then the samples are ready for metallographic and scanning electron microscopic analysis, including EDX as well.

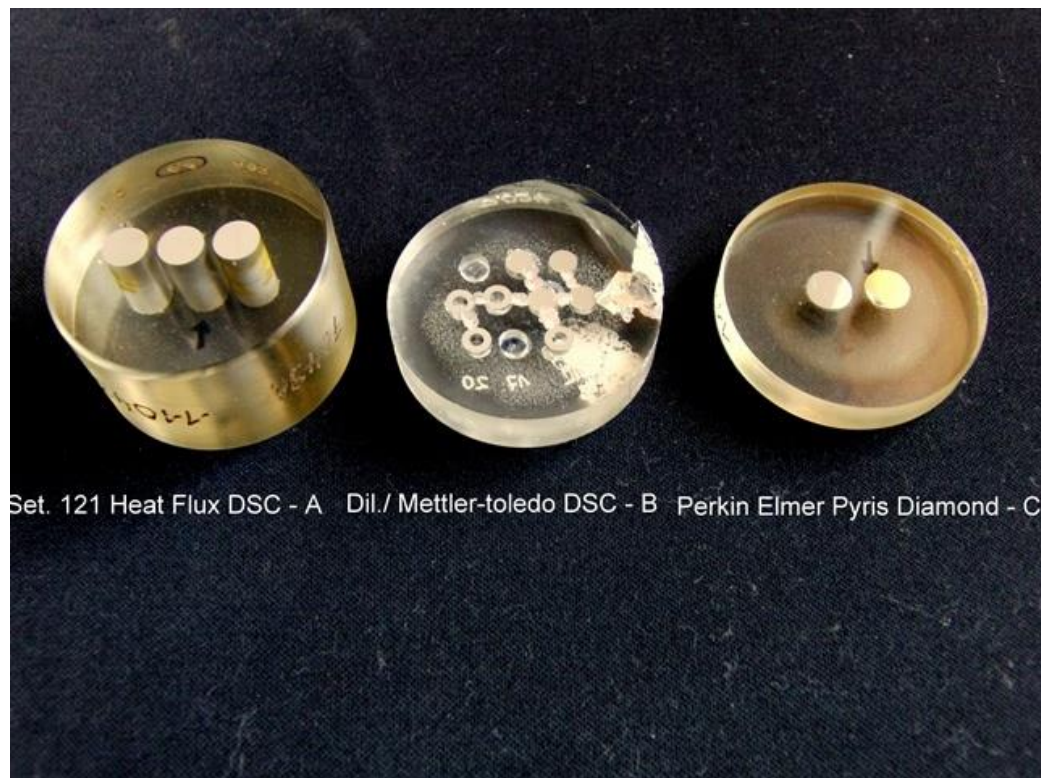


Fig. 26. Samples of the EN AW 7049A from different DSC devices prepared for SEM, EDX and metallographic analysis. A- Calvet type with bigger mass, then C – dilatometer quenched and Mettler Toledo samples smaller, C – Perkin Elmer Pyris Diamond fastest conventional DSC samples.

When the metallographic screenings of the samples are finalized the samples are subjected to hardness analysis. The analyses were performed with Shimadzu HMV-2, microhardness tester

Fig. 27. The weight was 9,81 N (1kg) and the indentation rod was a diamond crystal with pyramid shape (Vickers's Hardness HV1). For each sample in total 5 indentations were performed within various areas of the same sample. Calculation of the hardness was performed by averaging the values. Hardness testing with quenching rates $>5\text{K/s}$ have been tested at samples, which were quenched in a quenching dilatometer `` Bähr 805 AID``.

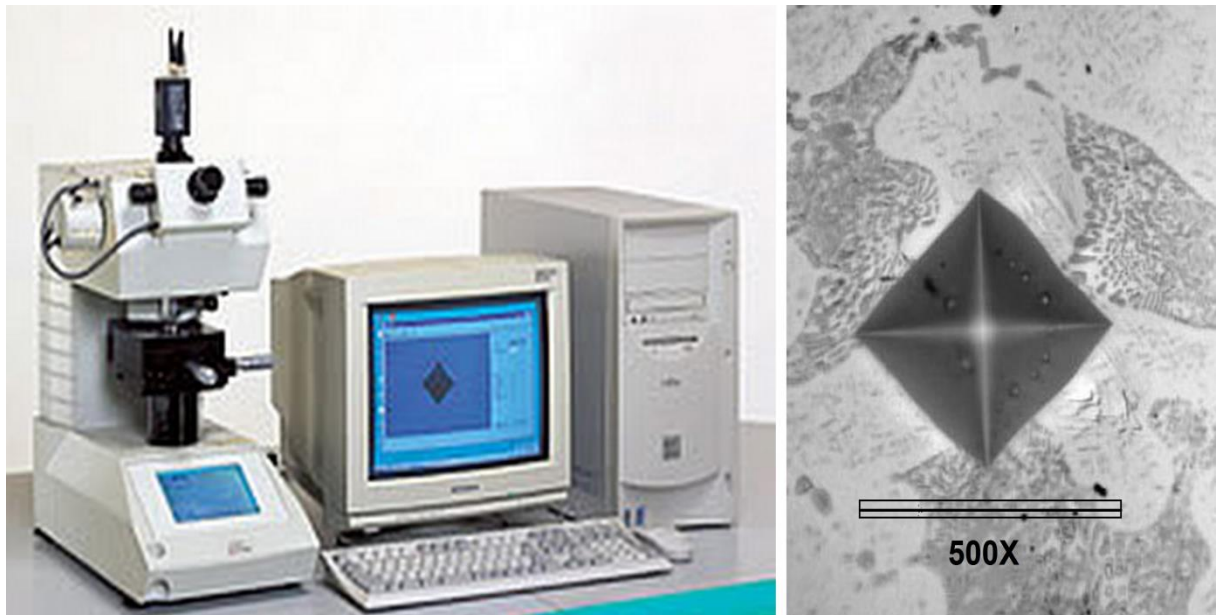


Fig. 27. Shimadzu HMV-2 microhardness tester – left, and the indentation on the right image.

3.4.3 Nano-indentation

Nano-indentation and the hardness analysis were performed at the Chair of New Materials Physics (University of Rostock) and at Erlangen University.

In nano-indentation small loads and tip sizes are used, so the indentation area may only be a few square micrometers or even nanometers. This allows hardness testing of the very small DFSC samples, but also represents problems in determining the hardness, as the contact area is not easily found. Atomic force microscopy or scanning electron microscopy techniques may be utilized to image the indentation, but can be quite cumbersome. Instead, an indenter with a geometry known to high precision (usually a Berkovich tip, which has three-sided pyramid geometry) is employed. During the measurements of the instrumented indentation process, a record of the depth of penetration is made, and then the area of the

indent is determined using the known geometry of the indentation tip. While indenting, various parameters such as load and depth of penetration can be measured. A record of these values can be plotted on a graph to create a load-displacement curve (Fig. 59). These curves can be used to extract mechanical properties of the material. [40]

The method was developed [41] to measure the hardness and elastic modulus of a material from indentation load–displacement data obtained during one cycle of loading and unloading. Although it was originally intended for application with sharp, geometrically self-similar indenters like the Berkovich triangular pyramid, we have since realized that it is much more general than this and applies to a variety of axisymmetric indenter geometries including the sphere. A discussion of why the method works for spherical indentation is given at the end of this section. A schematic representation of a typical data set obtained with a Berkovich indenter is presented in Fig. 28, where the parameter P designates the load and h the displacement relative to the initial unreformed surface. For modeling purposes, deformation during loading is assumed to be both elastic and plastic in nature as the permanent hardness impression forms. During unloading, it is assumed that only the elastic displacements are recovered; it is the elastic nature of the unloading curve that facilitates the analysis. For this reason, the method does not apply to materials in which plasticity reverses during unloading. However, finite element simulations have shown that reverse plastic deformation is usually negligible.

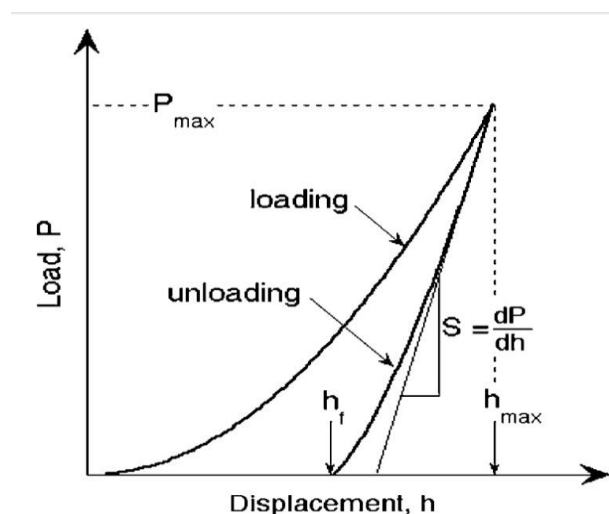


Fig. 28. Schematics of the data extraction from the typical load-displacement curves.

There are three important quantities that must be measured from the P–h curves: the maximum load, P_{max} , the maximum displacement, h_{max} , and the elastic unloading stiffness, $S = dP/dh$, defined as the slope of the upper portion of the unloading curve during the initial stages of unloading (also called the contact stiffness). The accuracy of hardness and modulus measurement depends inherently on how well these parameters can be measured experimentally. Another important quantity is the final depth, h_f , the permanent depth of penetration after the indenter is fully unloaded. The analysis used to determine the hardness, H , and elastic modulus, E , is essentially an extension of the method proposed by Doerner and Nix [40, 42] that accounts for the fact that unloading curves are distinctly curved in a manner that cannot be accounted for by the flat punch approximation. In the flat punch approximation used by Doerner and Nix, the contact area remains constant as the indenter is withdrawn, and the resulting unloading curve is linear. In contrast, experiments have shown that unloading curves are distinctly curved and usually well approximated by the power law relation:

$$P = \alpha (h - h_f)^m, \quad (1)$$

: Where α and m are power law fitting constants [41]

Young's modulus: The slope of the curve, dP/dh , upon unloading is indicative of the stiffness S of the contact. This value generally includes a contribution from both the material being tested and the response of the test device itself. The stiffness of the contact can be used to calculate the reduced Young's modulus [DIN EN ISO 14577] E_r :

$$E_r = \frac{1}{\beta} \frac{\sqrt{\pi}}{2} \frac{S}{\sqrt{A_p(h_c)}}, \quad (7)$$

where:

S - Indicative of the stiffness of the contact

$A_p(h_c)$ is the projected area of the indentation at the contact depth h_c , and β is a geometrical constant on the order of unity. $A_p(h_c)$ is often approximated by a fitting polynomial as shown below for a Berkovich tip:

$$A_p(h_c) = C_0 h_c^2 + C_1 h_c^1 + C_2 h_c^{1/2} + C_3 h_c^{1/4} + \dots + C_8 h_c^{1/128} \quad (8)$$

Where: C_0 for a Berkovich tip is 24.5, while for a cube corner (90°) tip is 2.598. The reduced modulus E_r is related to Young's modulus E_s of the test specimen through the following relationship from contact mechanics:

$$1/E_r = (1 - \nu_i^2)/E_i + (1 - \nu_s^2)/E_s. \quad (9)$$

Here, the subscript i indicate a property of the indenter material and ν is Poisson's ratio. For a diamond indenter tip, E_i is 1140 GPa and ν_i is 0.07. Poisson's ratio of the specimen, ν_s , generally varies between 0 and 0.5 for most and is typically around 0.3.

4 Results and Discussion

4.1 Precipitation reactions during continuous cooling inside conventional DSC

Excess c_p for slow cooling of 7049A is shown in Fig. 29.

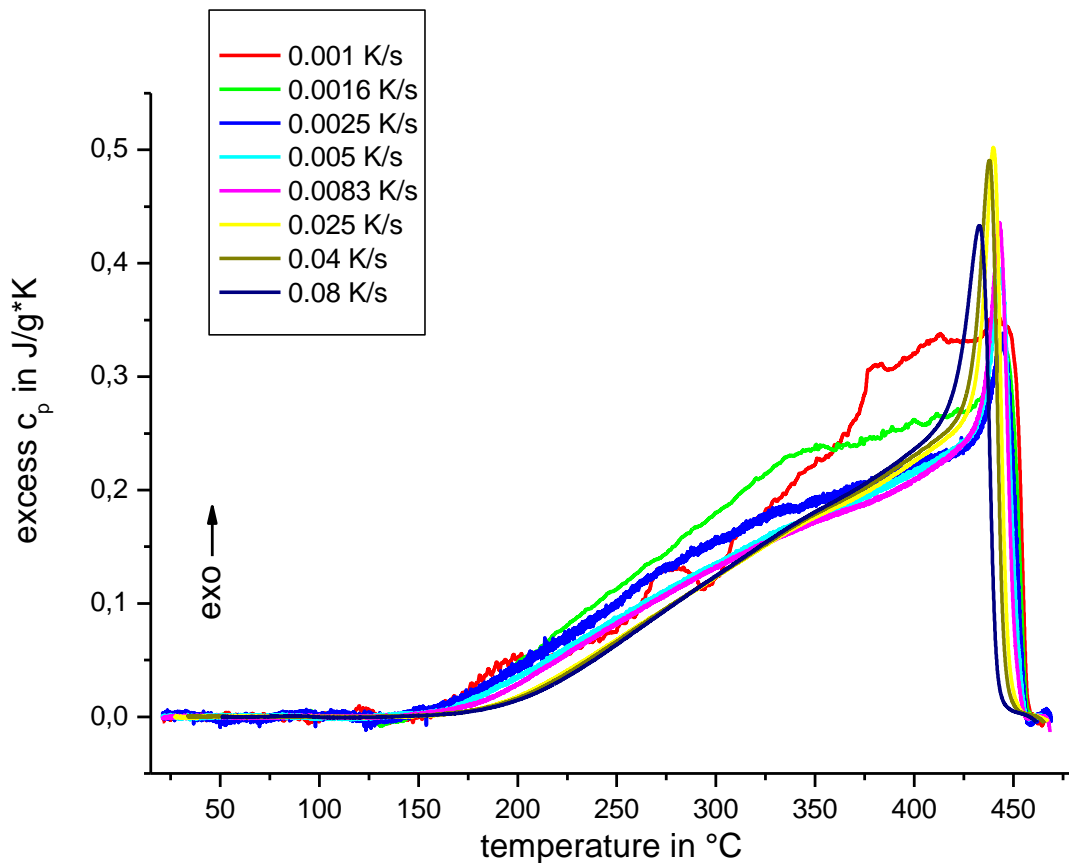


Fig. 29. EN AW 7049A, general overview, excess specific heat vs. sample temperature, various cooling rates starting from close to equilibrium (0.001 K/s). Very broad exothermic reaction zone can be seen which keeps up to c.a. 100 °C from Setaram DSC 121 device.

If the same curves are plotted with vertical shift with defined value 0.1 J/g*K it will be much easier to determine how the precipitation reaction zone develops with changing cooling rate over the temperature range accessible with Setaram 121 DSC, Fig. 29 and Fig. 30.

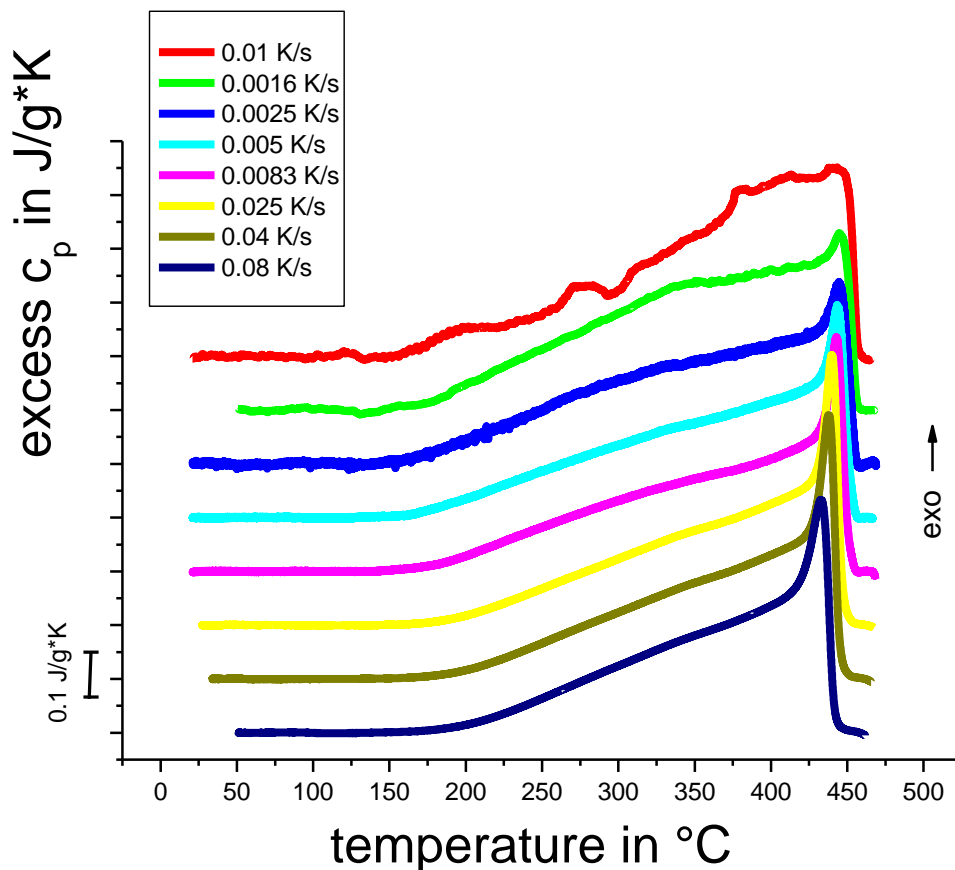


Fig. 30. EN AW 7049A alloy excess c_p vs. sample temperature, starting from the slowest rate on top, red curve. On cooling from the annealing temperature two strong overlapped precipitation reactions can be seen provided from Setaram 121 data.

The strong reaction zones which are so called high-temperature and low-temperature change significantly with cooling rates. The change in curve shows that the broad high temperature exothermic reaction becomes sharper. Meanwhile the second so called low temperature reaction shifts to high temperature where it partially overlaps with high temperature reaction, creating a broad wide range shoulder where both reactions are taking place simultaneously during the cooling.

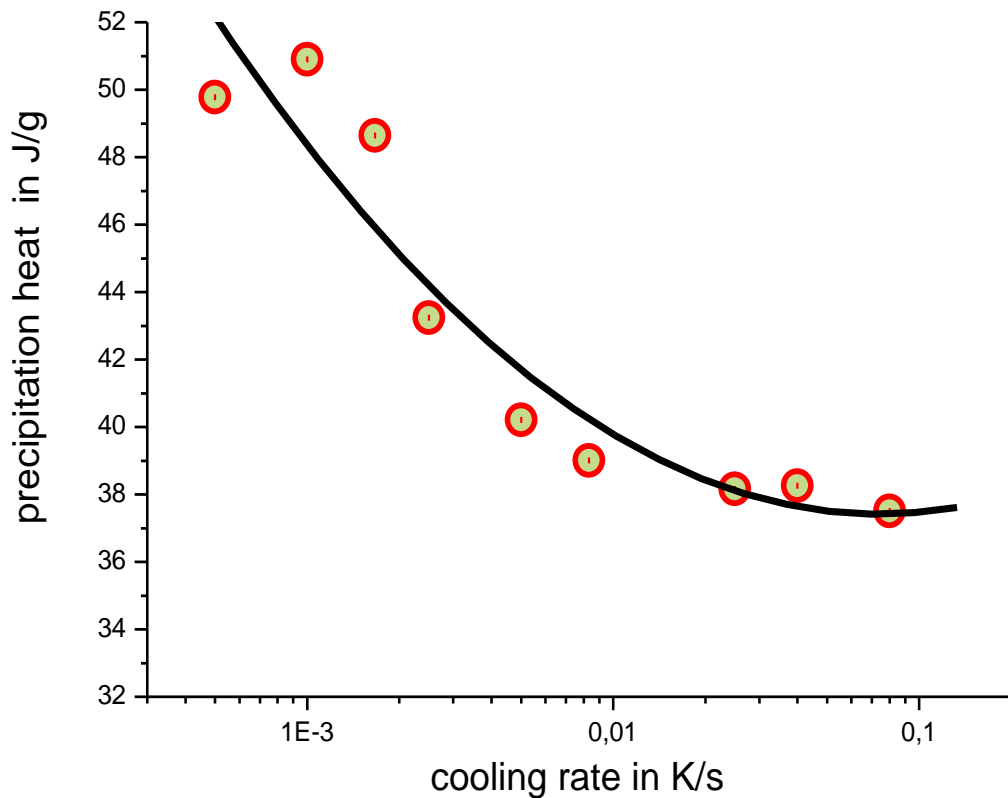


Fig. 31. EN AW 7049A, precipitation heat vs. cooling rate calculated from excess specific heat capacity curves. The device was Setaram 121 DSC.

Fig. 27 represents how the precipitation heat is changing with cooling rate. Starting from about 50 J/g at 0.001 K/s, precipitation heat decreases with increasing cooling rate, down to about 38 J/g at 0.1 K/s.

Fig. 32 shows the change of the excess cp against temperature for the EN 7049A alloy system. Starting from the slowest cooling rate, which equals to 0.05 K/s the overall reaction (precipitation heat), has the highest value of about 0.6 J/g. Though the other rates show similar exothermic reactions, but the overall value with respect to precipitation heat decreases significantly with increasing cooling rate.

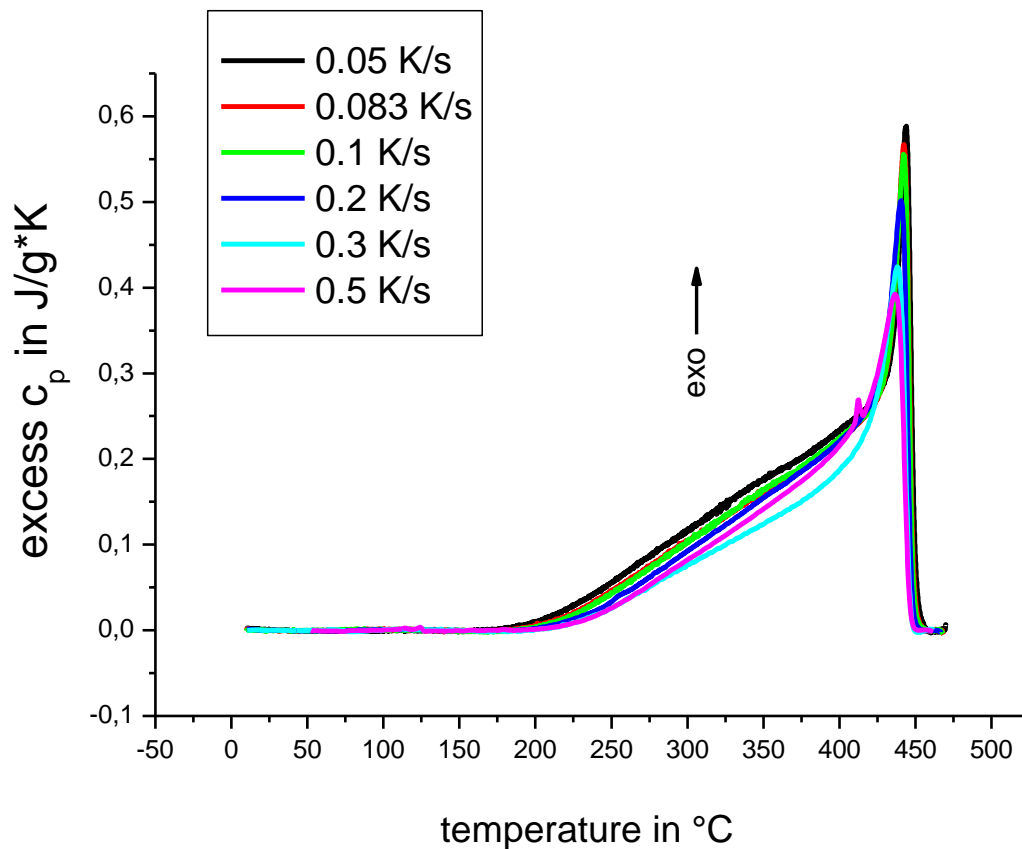


Fig. 32. EN AW7049A, general overview, excess specific heat vs. sample temperature, various cooling rates. The above mentioned data was collected via DSC Mettler-Toledo 823e.

In comparison to the data plotted in Fig. 29 the precipitation reactions are taking place within the same temperature range, but what is changing can be seen from temperature scale, the reaction zone shift to higher temperature and finalized at 200 $^{\circ}C$ instead of 140 $^{\circ}C$ in Fig. 29. The starting onset of the reaction remains the same in both plots and is equal to c.a. 453 $^{\circ}C$.

Fig. 33 shows the change of the excess c_p against temperature for the EN 7049A alloy system. Starting from the slowest cooling rate, which equals to 0.05 K/s the overall reaction (precipitation heat), has the highest value of about 0.6 J/g. Though the other rates show similar exothermic reactions, but the overall value with respect to precipitation heat decreases significantly with increasing cooling rate. The curves in figure have been shifted with 0.1 J/g for better overview.

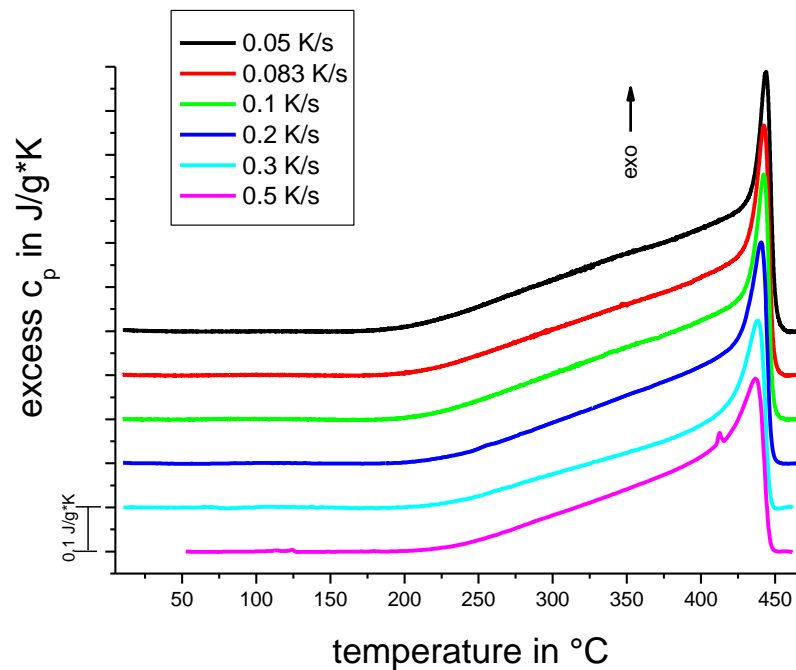


Fig. 33. EN AW 7049A alloy: excess c_p vs. sample temperature for various cooling rates. Starting from the slowest rate (black curve), till fastest (pink), where the cooling from the annealing temperature starts, two exothermic reactions which are overlapped can be seen. The curves are shifted with J/g*K for better overview, DSC Mettler-Toledo 823e⁻ was employed.

The decrease of the two exothermic reaction zones continues here as well, but the shape of the precipitation reactions remains same [35]. Sharp peak starts immediately when cooling starts and with decreasing temperature it continues to have the broad decrease up to 200 °C.

Further the calculation of the precipitation heat from the data in Fig. 33, shows how significant is the decrease of the both reactions with respect to cooling rate change, in the range where Mettler-Toledo DSC 822e⁻ measures the signal of precipitation, Fig. 34.

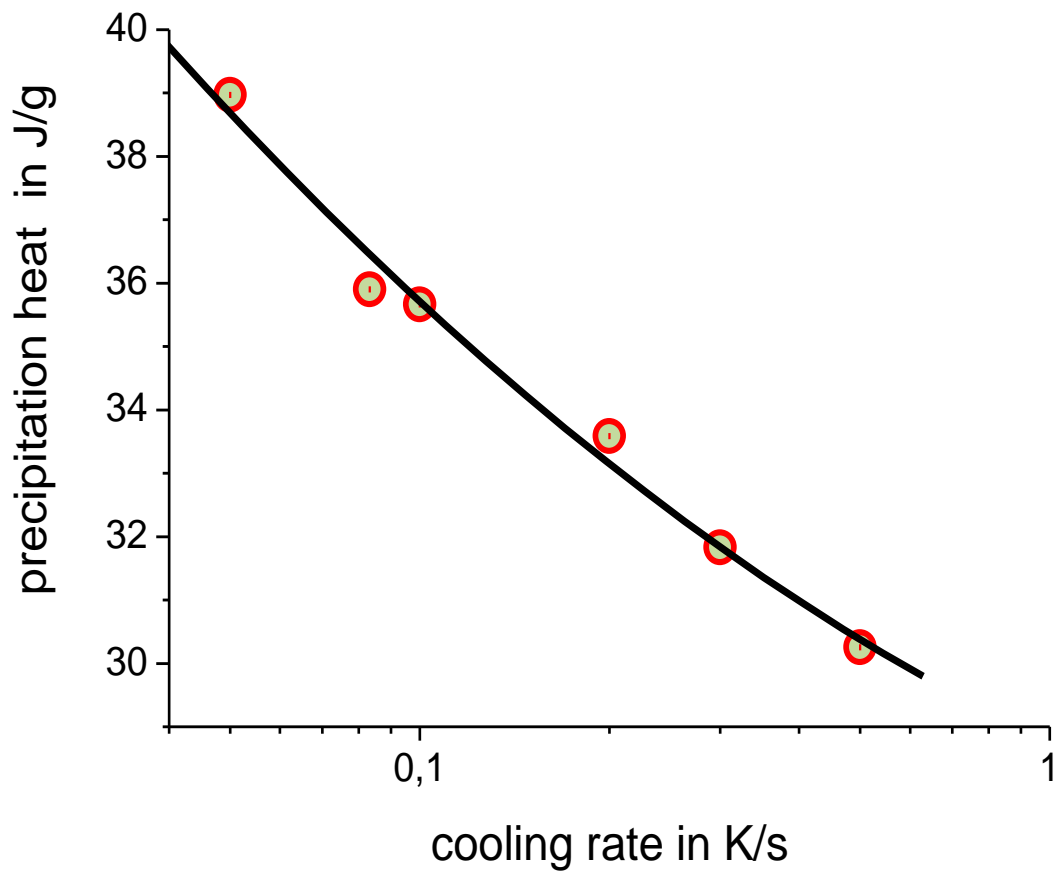


Fig. 34. EN AW 7049A alloy precipitation heat vs. cooling rate, measurements from Mettler-Toledo 822e. The starting value of c.a. 40 J/g decreases by about 10 J/g during cooling from 0.05 – 0.5 K/s.

Similar picture can be observed with the DSC Perkin –Elmer Pyris-1. In comparison to heat flux DSC's, the cooling capabilities of the machine allow much faster cooling rates, up to 7 – 8 K/s. This will help to correlate the data which was obtained from both devices which were discussed above (Setaram 121, Mettler-Toledo 822e).

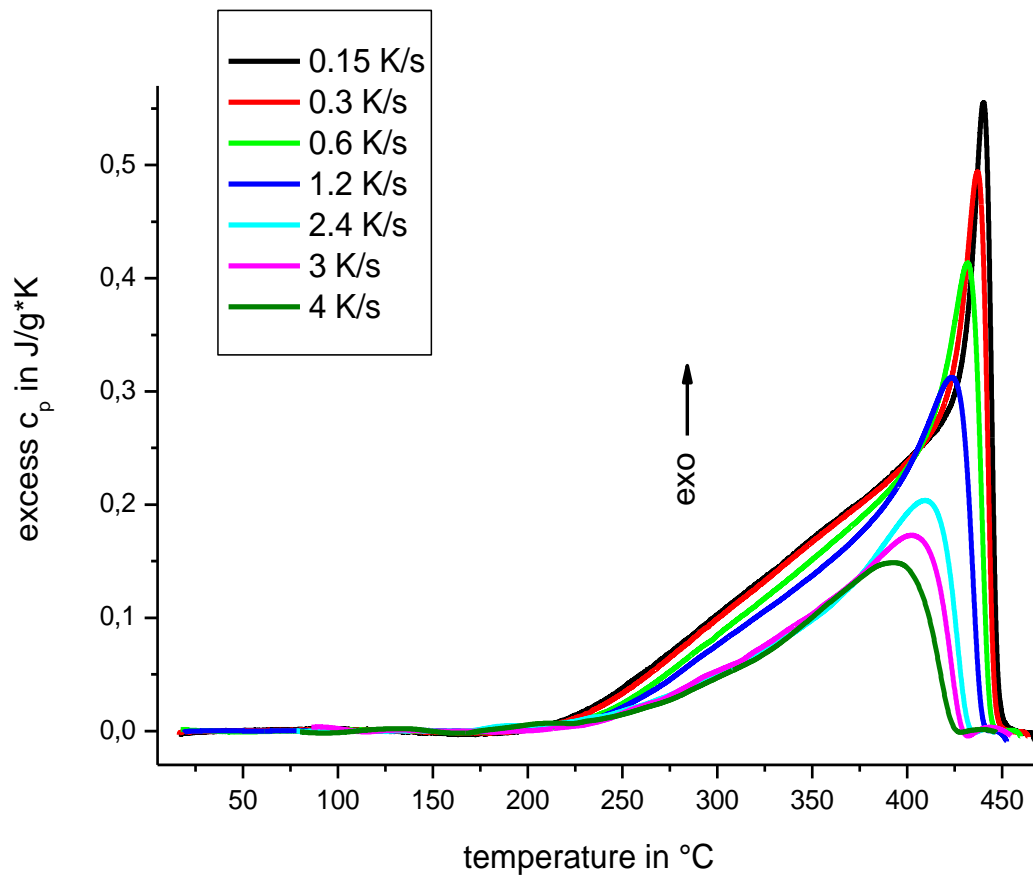


Fig. 35. EN AW 7049A alloy ,general overview, excess specific heat vs. sample temperature, various cooling rates starting from (0.15 K/s). Very broad exothermic reaction zone can be seen which keeps up to c.a. 225 °C, the data was obtained from Pyris-1 DSC from Perkin Elmer.

The precipitation reaction is starting to decrease rapidly, Fig. 35, and the change of the peak shape tells that fast cooling inside the Pyris-Diamond does not allow precipitations to occur intense with respect to other two devices. The sharp high temperature peak becomes small and the low temperature reaction shifts to high temperature. The sum of both effects is just one exothermic reaction zone in the temperature range from 425°C -225°C. In our case the limitation of the technique does not allow to go faster than 4 K/s. But still at this rate we can see that the critical cooling rate cannot be achieved Fig. 36. Further the DRM method and Ultra-fast DSC will be used to continue the experiments, in order to achieve the critical cooling rate for this alloy.

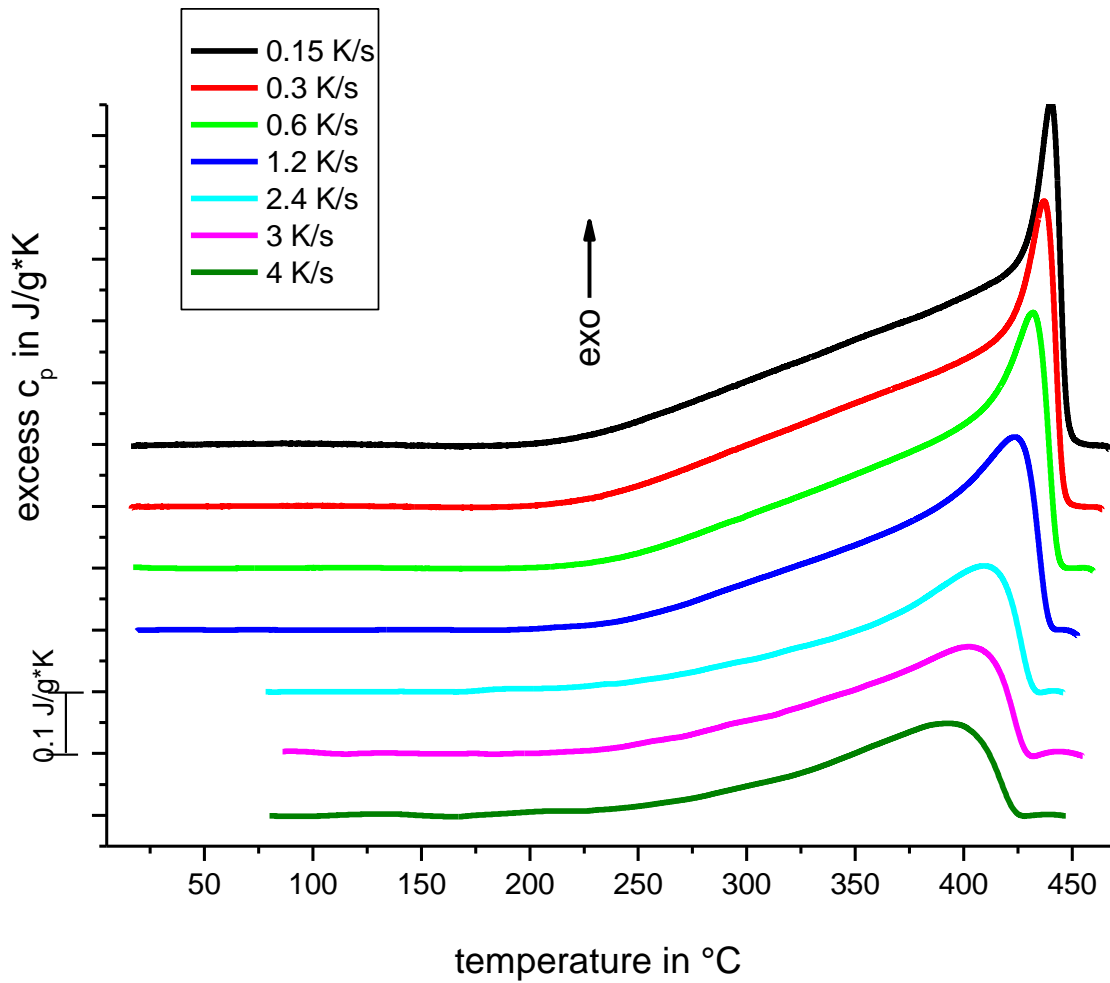


Fig. 36. EN AW 7049A alloy: excess c_p vs. sample temperature for various cooling rates, two exothermic reactions which are overlapped can be seen. The curves are shifted with 0.1 $J/g \cdot K$ for better overview the data was obtained from Pyris-1 DSC from Perkin Elmer.

The decrease of the two exothermic reaction zones continues here as well, but the shape of the precipitation reactions remains same. Sharp peak starts immediately when cooling starts and with decreasing temperature it continues to have the broad decrease up to 200 $^{\circ}C$. Further the calculation of the precipitation heat from the data in Fig. 37, shows how significant is the decrease of the both reactions with respect to cooling rate change, in the range were Pyris-1 measures the signal of precipitation, Fig. 36.

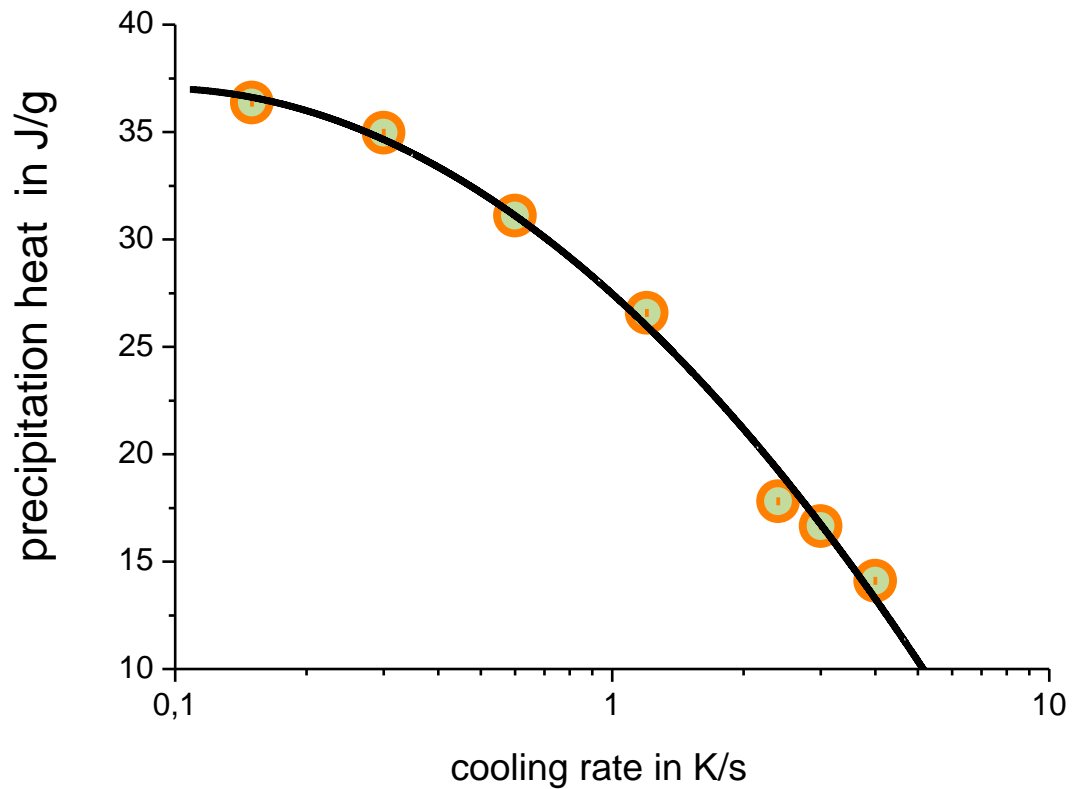


Fig. 37. EN AW 7049A alloy precipitation heat vs. cooling rate, measurements from Pyris-Diamond. The starting value of c.a. 37 J/g decreases till 10 J/g during cooling from 0.15 – 4.0 K/s.

Fig. 38 represents the excess c_p vs. sample temperature for the broad range of technical cooling rates for all three devices which are of great interest. Therefore the exothermic reactions occurring on cooling can be evaluated up to 4K/s. This is the part where the device comes to its limits and therefore it is not possible to go further with faster cooling. The change of the peak shape can be seen from Fig. 38, where it becomes sharp close to 0.005 K/s cooling rate, and later near to 4 K/s it starts to become significantly smaller and broad.

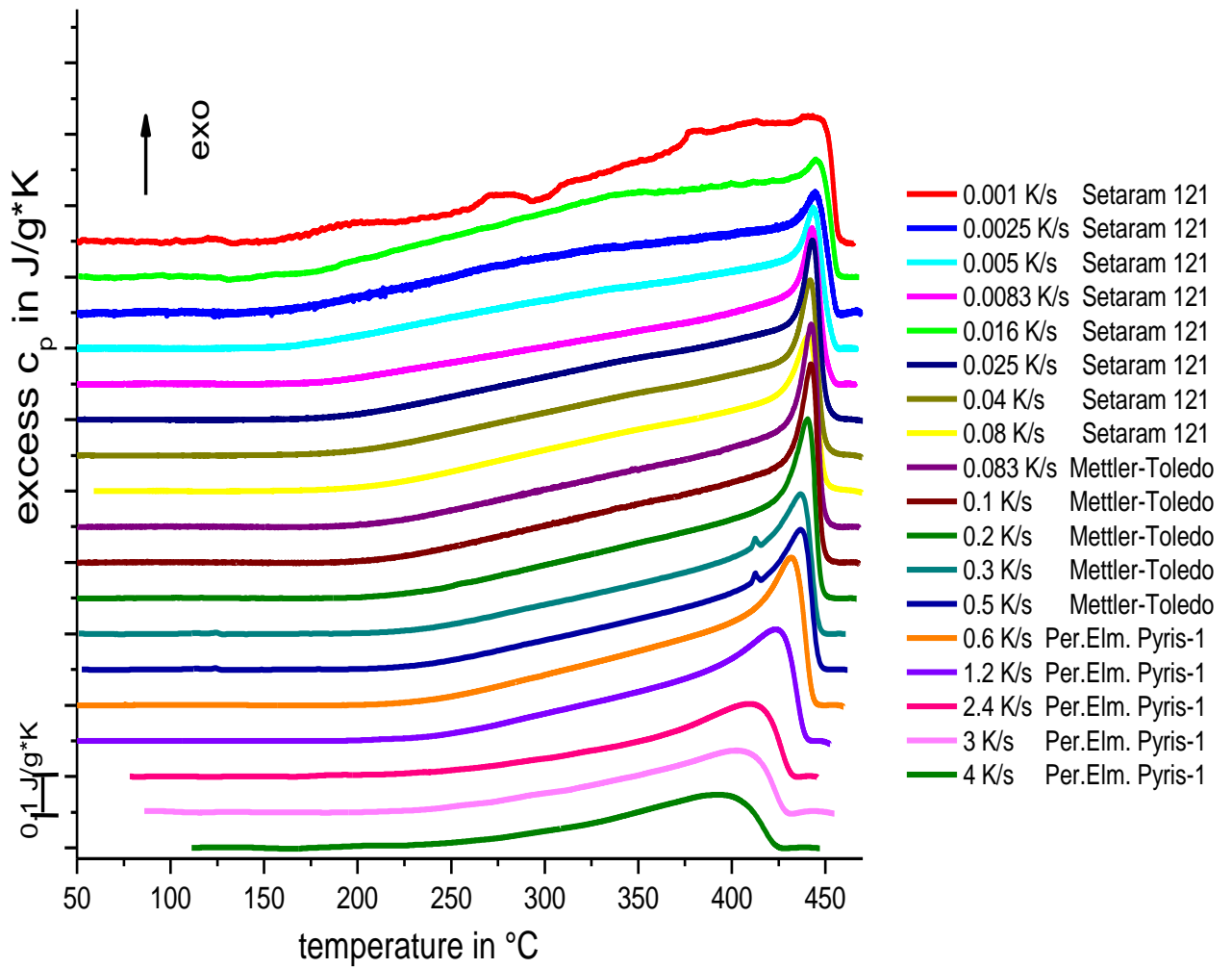


Fig. 38. EN AW 7049A alloy cooling over wide range (0.0005 – 4 K/s). The curves are shifted with 0.1 J/gK, the exotherms are up. Data from 3 DSC devices, except DFSC.

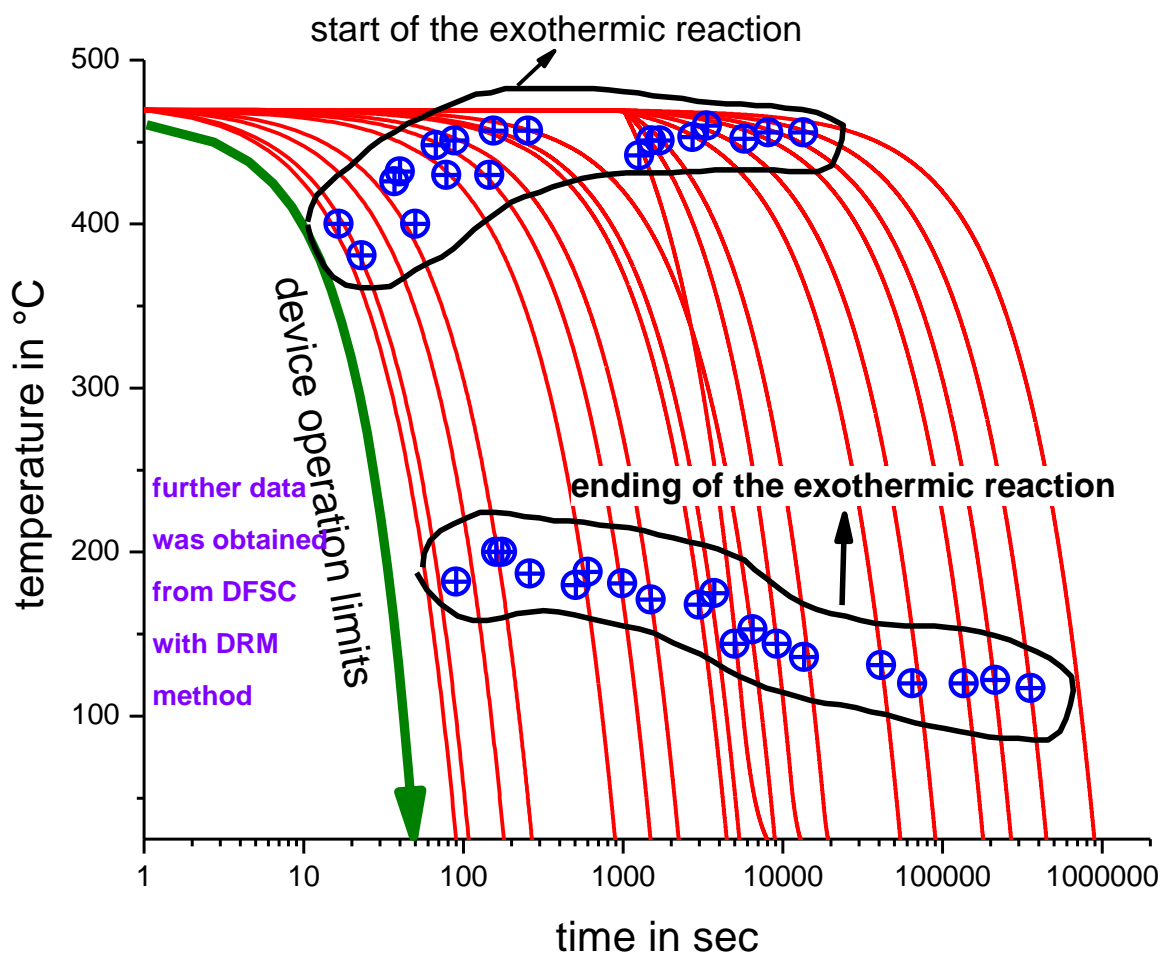


Fig. 39. CCP diagram of the EN AW 7049A alloy calculated from the excess c_p curves, the marked signs indicate the start and end temperature of the main exothermic reactions.

In Fig. 39 the CCP diagram represents the main exothermic reactions starting and ending depending on temperature. The violet circles represent the starting of the high temperature reaction, and the pink triangles are the ending of the low temperature exothermic reaction. The limits are close to 4 K/s, which is due to DSC.

The cooling curves which start from very slow rates are shown on the top of the plot. The two main reactions (so called high and low temperature) are still seen up to 4 K/s and this is already the limitation of the conventional calorimetric technique.

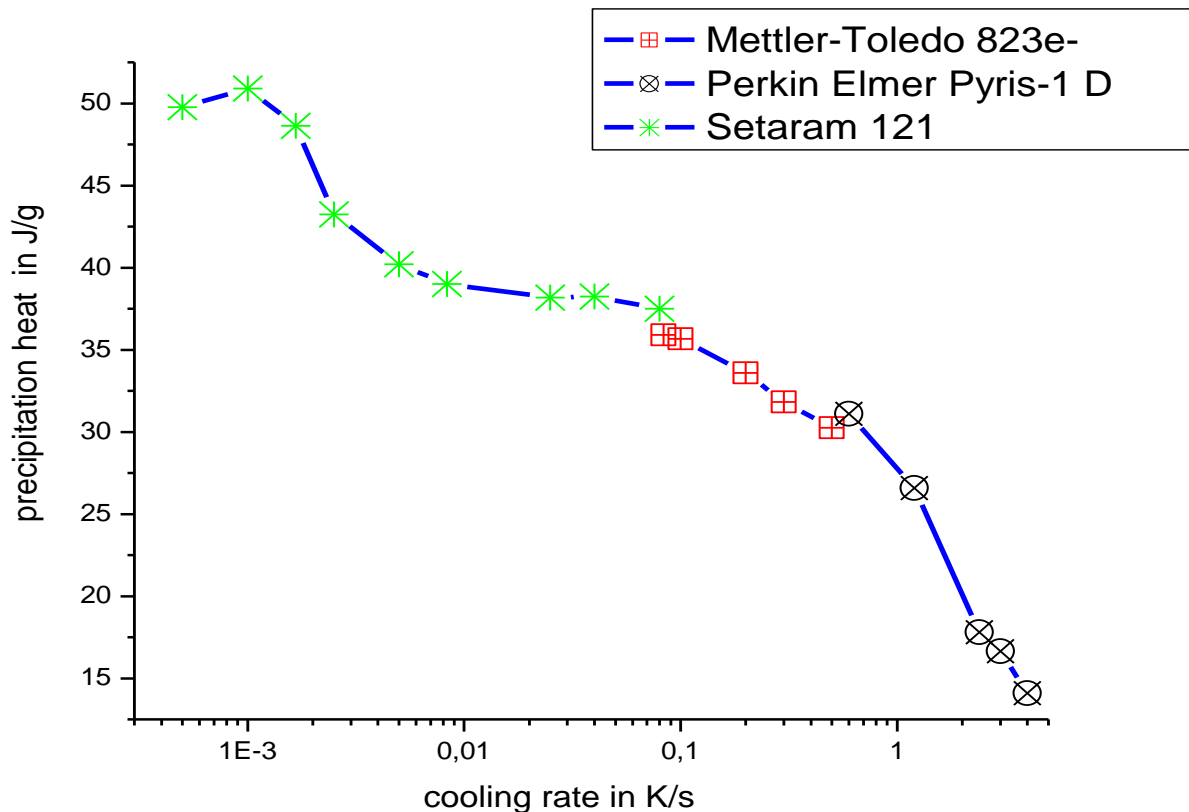


Fig. 40. EN AW 7049A alloy precipitation heat vs. cooling rate, over five orders of magnitude cooling rate range variation was achieved involving three different DSC's except DFSC.

Fig. 40 shows the precipitation heat of all three DSC devices. The good agreement of specific heat, when changing the devices, proves the reliability of the results. The enthalpy change starts from 50 J/g and decrease to c.a. 10 J/g at about 10 K/s cooling rate. It means that there is a strong precipitation effect which causes about 10 J/g enthalpy change. Otherwise we would have ended up with zero enthalpy change instead of 10 J/g.

4.2 Ultra-Fast Scanning FSC data obtained via DRM method

Ultra-fast DFSC [15] Fig. 5, was used for the further study of the precipitation reactions which were observed in conventional DSC's. The limit of the cooling for the fastest commercial DFSC was defined to 4 K/s. Now using the Mettler Flash-1 chip based DSC and involving the differential reheating method discussed in Fig. 16, and Fig. 17 will make an attempt to find the critical cooling rate of the EN AW 7049A alloy. DRM method was studied in detail for precipitation reactions on reheating in order to compare them with the data plotted in Fig. 40. As it was mentioned the data from reheating can be directly compared with the cooling [15, 27, 43-48], see the Fig. 16.

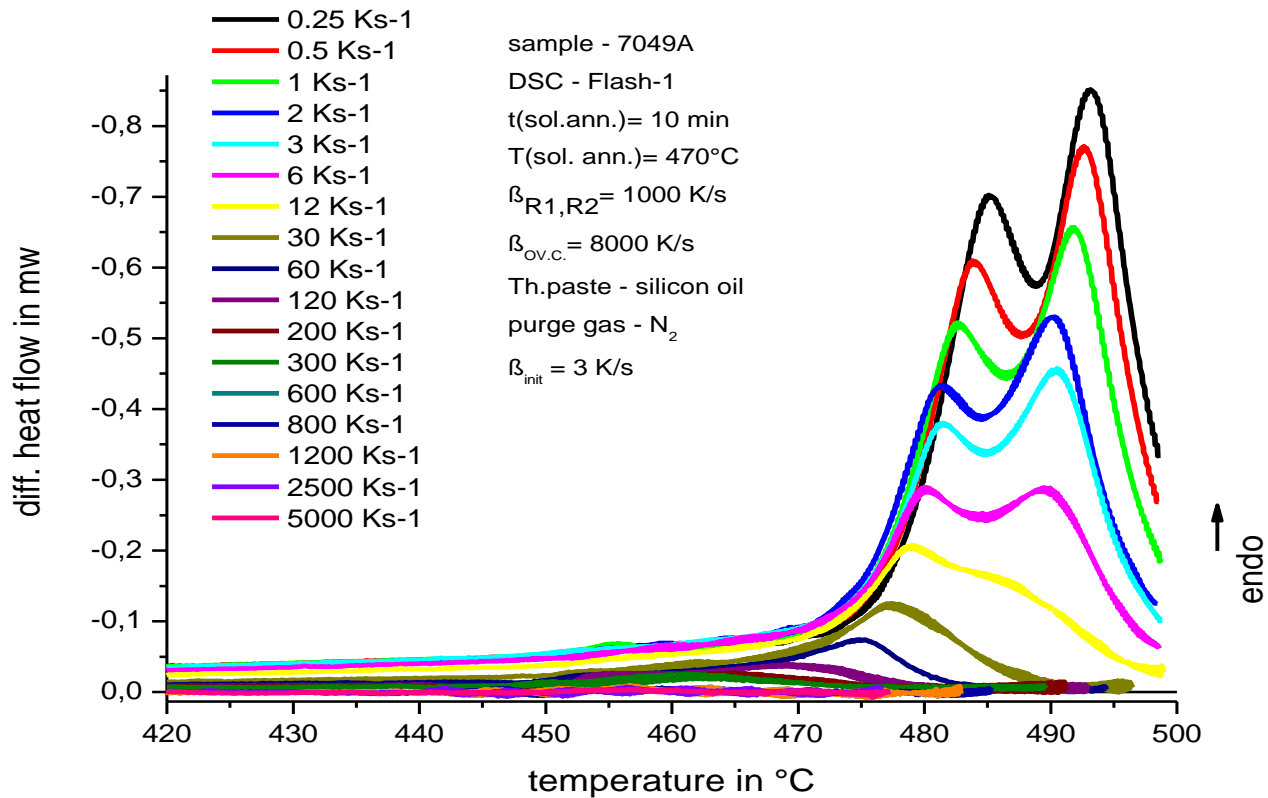


Fig. 41. Differential heat flow vs. temperature plot, for the EN AW 7049A alloy system. Reheating curves. Previous cooling rate varied from 0.25 – 5000 K/s. DFSC with the DRM was employed. R1- reheating number one after first cooling, R2- reheating after overcritical cooling, β_{ov} - overcritical cooling.

Plotted data in Fig. 41 shows the reheating of the sample which was previously cooled with different rates. As one can see the differential heat flow signal starts to differ from zero starting from 500°C. There are two main endothermic effects which are responsible for the shift from zero [49]. These effects are the dissolution of the various phases which are formed during quenching. The most fascinating thing about this plot is the intense change of the endothermic reactions with respect to previous cooling rate. It does mean that the curves where the previous cooling was performed faster show smaller endothermic effect in comparison to the curve which was cooled slower. Correlating the data obtained from this device with other DSC's as well as with the hardness data can give valuable information not only for the critical cooling rate but also for metallographic analysis. The data in Fig. 42 shows another set on experiments performed on Ultra-Fast DFSC Flash -1.

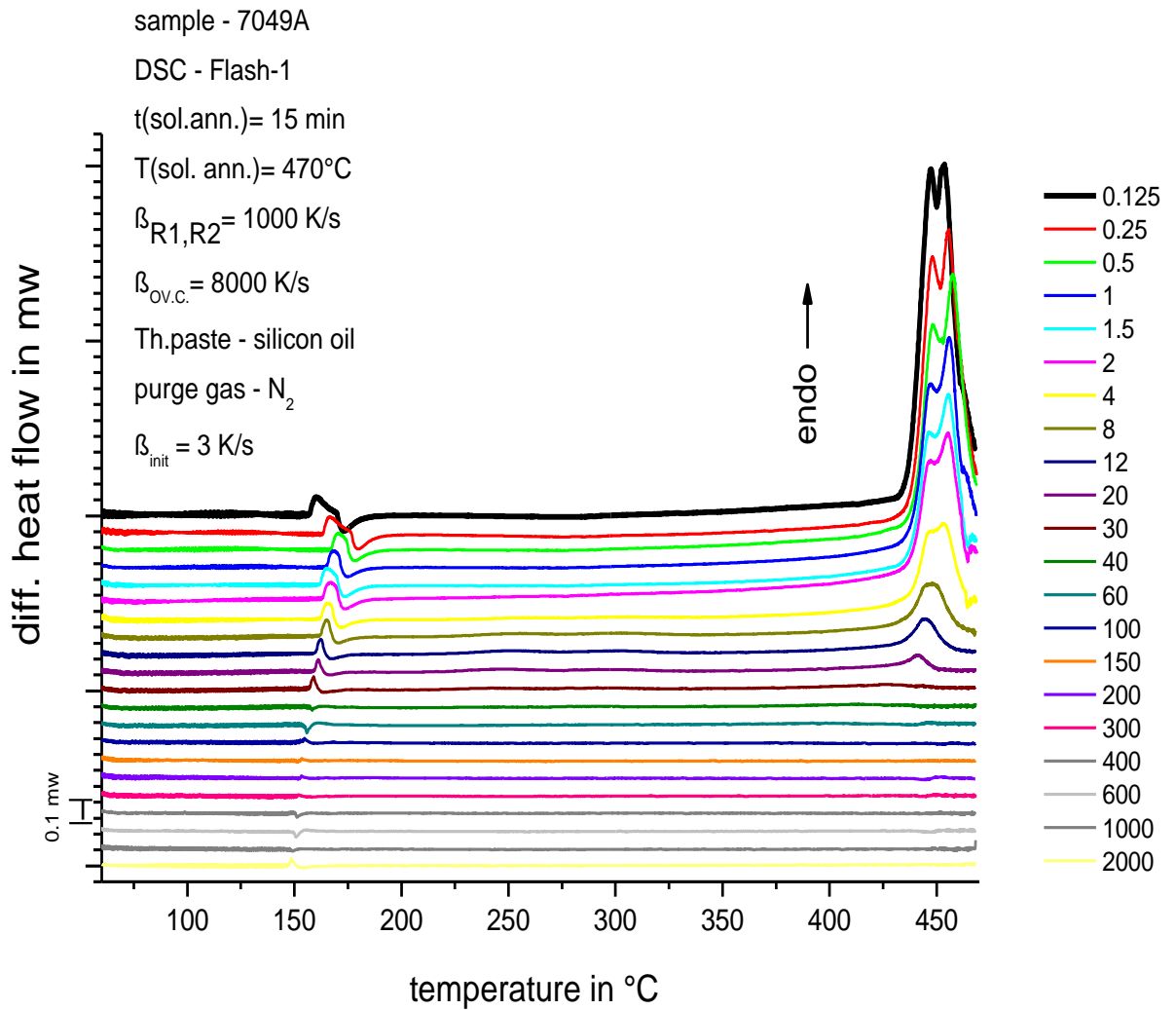


Fig. 42. EN AW 7049A alloy, differential heat flow vs. temperature, the sample was solution annealed for 15 min and reheated with 1000 K/s rate, under nitrogen purging, overcritical cooling rate was 8000 K/s. DFSC with the DRM was employed.

For the precipitation heat calculation the curves were integrated and plotted versus cooling rate, Fig. 43.

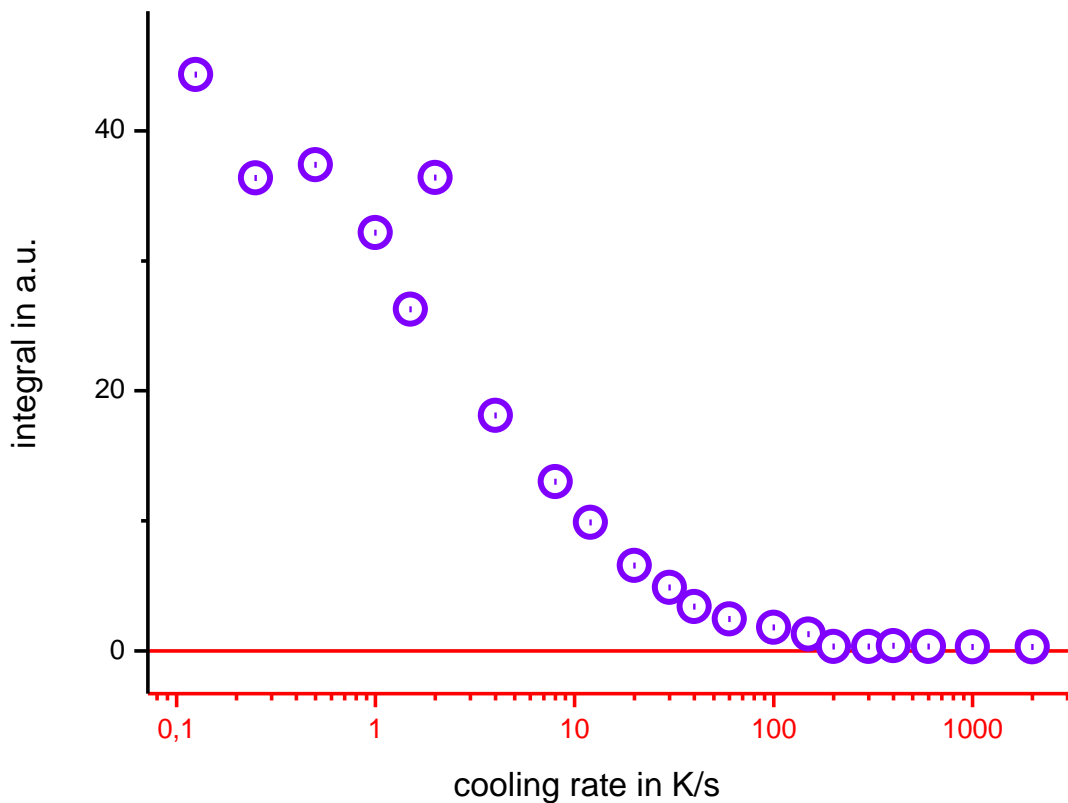


Fig. 43. EN AW 7049A alloy Integration of the differential heat flow versus temperature, and plotted vs. cooling rate. The integral is in arbitrarily units because the sample weight is not known; DFSC with the DRM was employed.

The decrease shown in plot continues until about 100-300 K/s, and later it reaches to zero, though remaining constant till 2000 K/s. Taking into consideration how the reheating method is working, we can estimate that the critical cooling rate is somewhere at about 100-300 K/s. In order to confirm the results, many datasets of experiments have been performed with similar experimental conditions.

The sample weights are not normalized therefore the shift of the curves due the various masses can be seen Fig. 44.

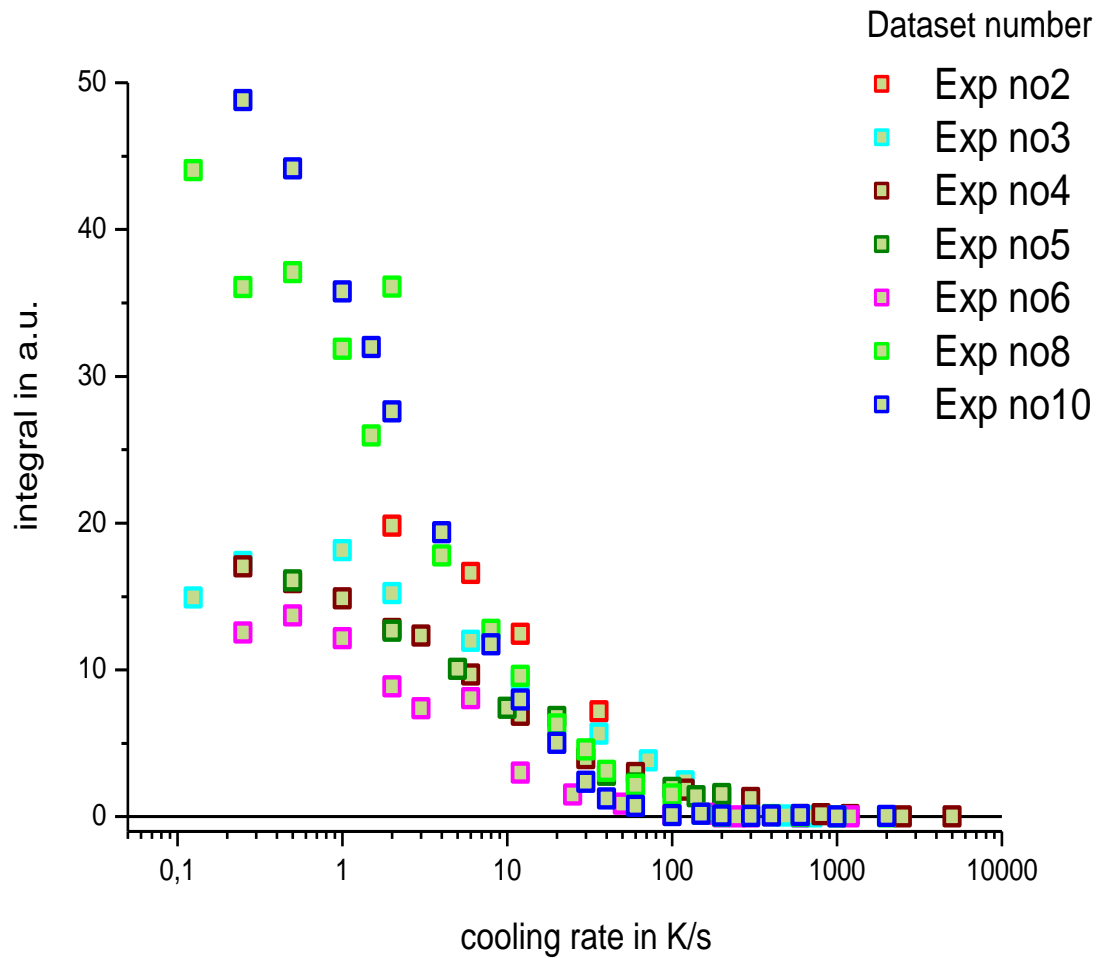


Fig. 44. EN AW 7049A alloy; various datasets obtained from Flash-1 Ultra-fast DFSC, all the datasets show the same CCR which is near to 100-300 K/s.

Summarizing the experiments performed in Ultra-DFSC's and plotting the data together with conventional DSC and also including hardness measurements, Fig. 45 can be seen the correlation of the critical cooling rate with hardness developments and also with the precipitation heat. Therefore the integrals in a.u. from DFSC have been calibrated with DSC experiments using the same cooling rate.

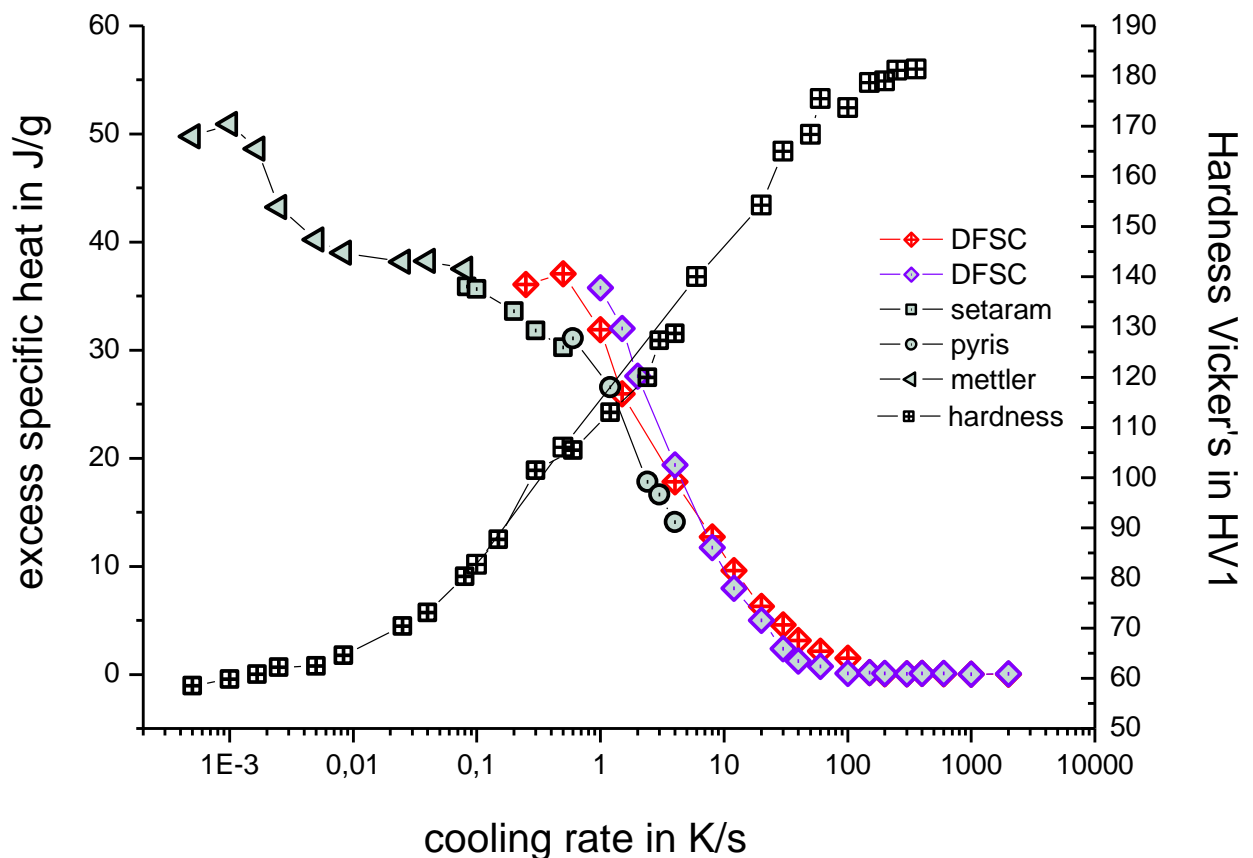


Fig. 45. EN AW 7049A alloy: excess specific heat vs. cooling rate and hardness HV1 Vickers. The precipitation heat (cooling) from DSC (Setaram 121, Mettler-Toledo, Pyris) and precipitation heat (reheating) from DFSC Mettler Flash -1 are scaled together; the data from Ultra-Fast DFSC is normalized.

The plot represents a very nice correlation in between various analytical techniques: which are the conventional DSC's, Hardness analysis, and the ultra-fast chip based DFSC. One can see that the precipitation heat calculated from cooling step in conventional DSC very nicely continues the precipitation heat obtained from Chip DFSC during reheating experiments and finally they end up with zero value, where one can see the critical cooling rate. The small deviation in range of 0.1 – 1 K/s is due to the very low sensitivity of the machine (DFSC). The fast scanning device (DFSC) has low sensitivity at slow scanning rates. Further the Vickers hardness analysis show the same correlation with respect to data obtained from DSC. The hardness values increases when the cooling rate increases. The increase in hardness

saturates near to critical cooling rate as expected. This means that the precipitation reactions have been fully suppressed. Only when the precipitation reactions are fully suppressed, one can be achieve the maximum hardness value after aging Fig. 45.

4.3 Metallographic analysis

The sample was solution annealed then cooled with rate 0.001 K/s inside DSC, and aged 30 days at room temperature. The primary precipitates, (insoluble phase) remained as it was expected, without any significant change (marked as red circles) Fig. 46. The precipitates of the secondary phase were relative large, up to about 7 μm . Coarse, needle like particles, marked with blue circles and the ones which have cubic geometry, marked with acid green circles.

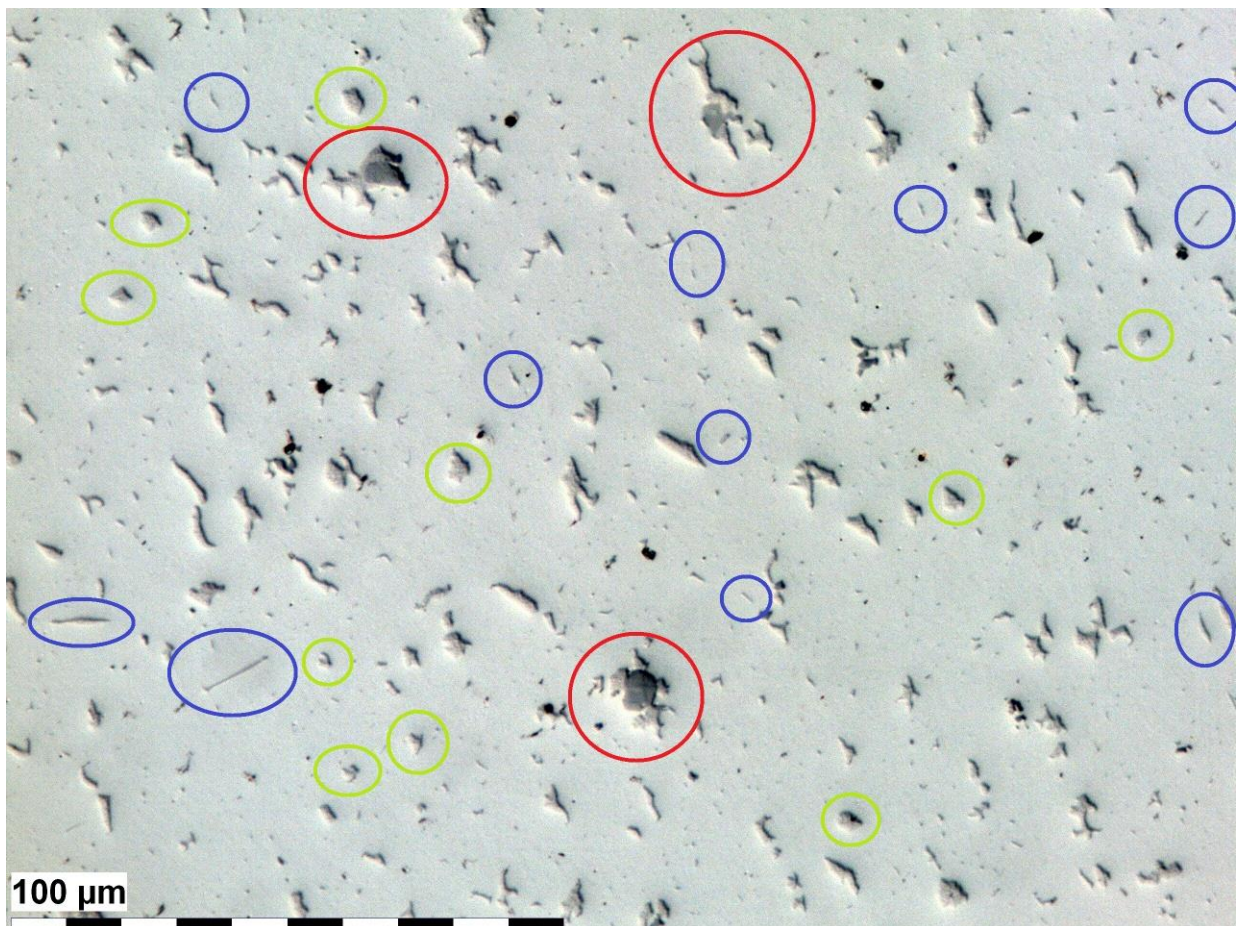


Fig. 46. 7049A alloy microstructure under light microscope, cooling rate =0.001 K/s : the red circles represent the insoluble phase, the blue circles and the green circles represent the secondary phases.

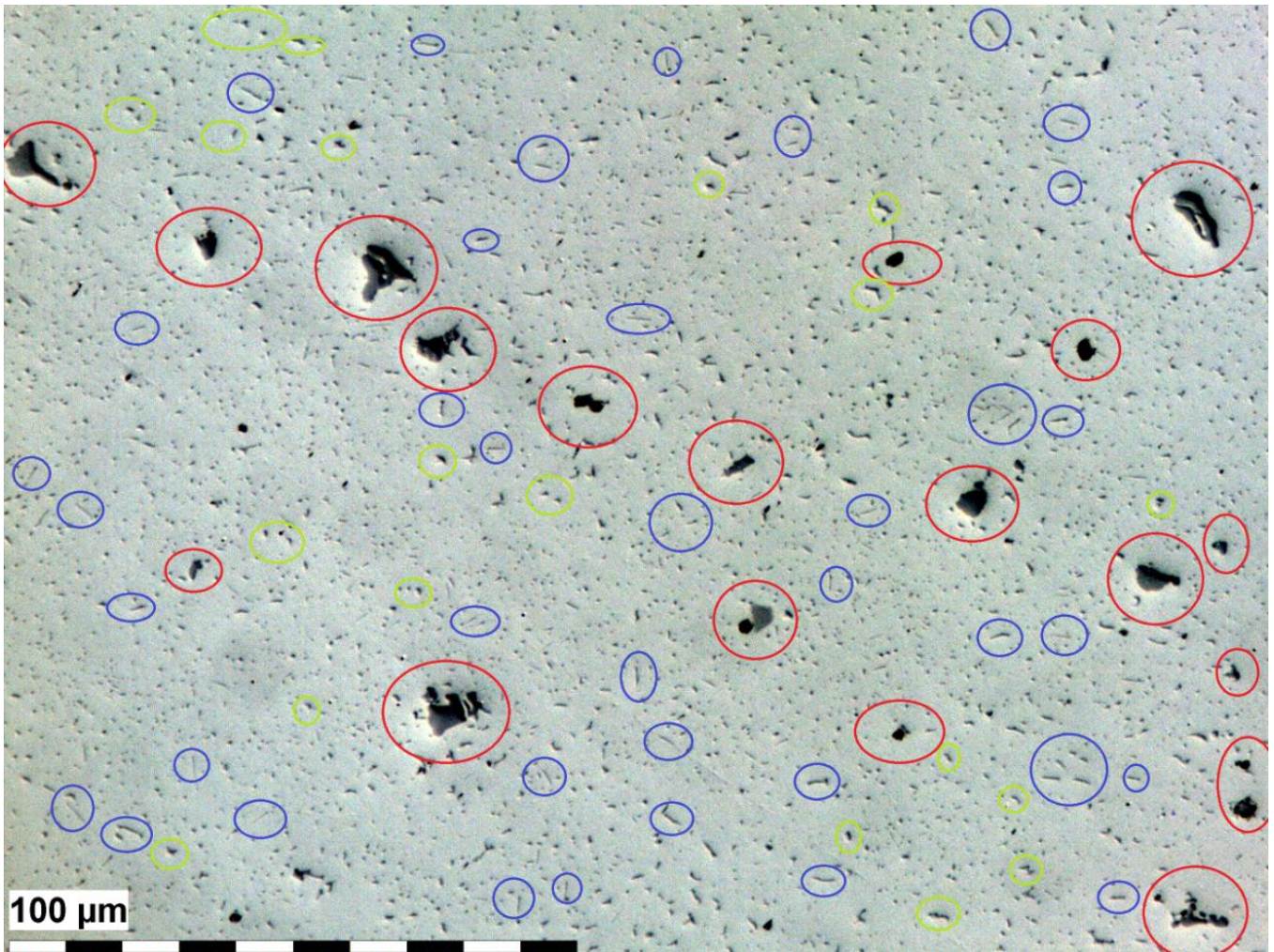


Fig. 47. 7049A alloy, microstructure under light magnification, cooling rate =0.08 K/s : the red circles represent the insoluble phase, the blue circles and the green circles represent the secondary phases.

To achieve the maximum ultimate strength the particle size should hinder the dislocation movement effectively, or efficiently. This can be only achieved, when the particle size is in range of several nanometers.

Fig. 46 points out the particle sizes are significantly bigger than several nm. This size is of about several microns. In Fig. 47 the cooling rate is 0.08 K/s and the changes in microstructure intensive in comparison to Fig. 46. As it was expected the primary phase (red circles) remains the same, the other two phases become smaller. The size of the secondary precipitates does change significantly with the rate of cooling.



Fig. 48. 7049A alloy, microstructure under light microscope, cooling rate =0.6 K/s : the red circles represent the insoluble phase, the blue circles and the green circles represent the secondary phases.

In Fig. 48 one can spot the sizes of the secondary phases, though they became significantly smaller. That means with the same magnification, possibility to measure sizes as well as the growth path and shapes of the precipitates inside the sample becomes uncertain. For the current alloy system metallographic technique by light microscopy has reached to its limits.

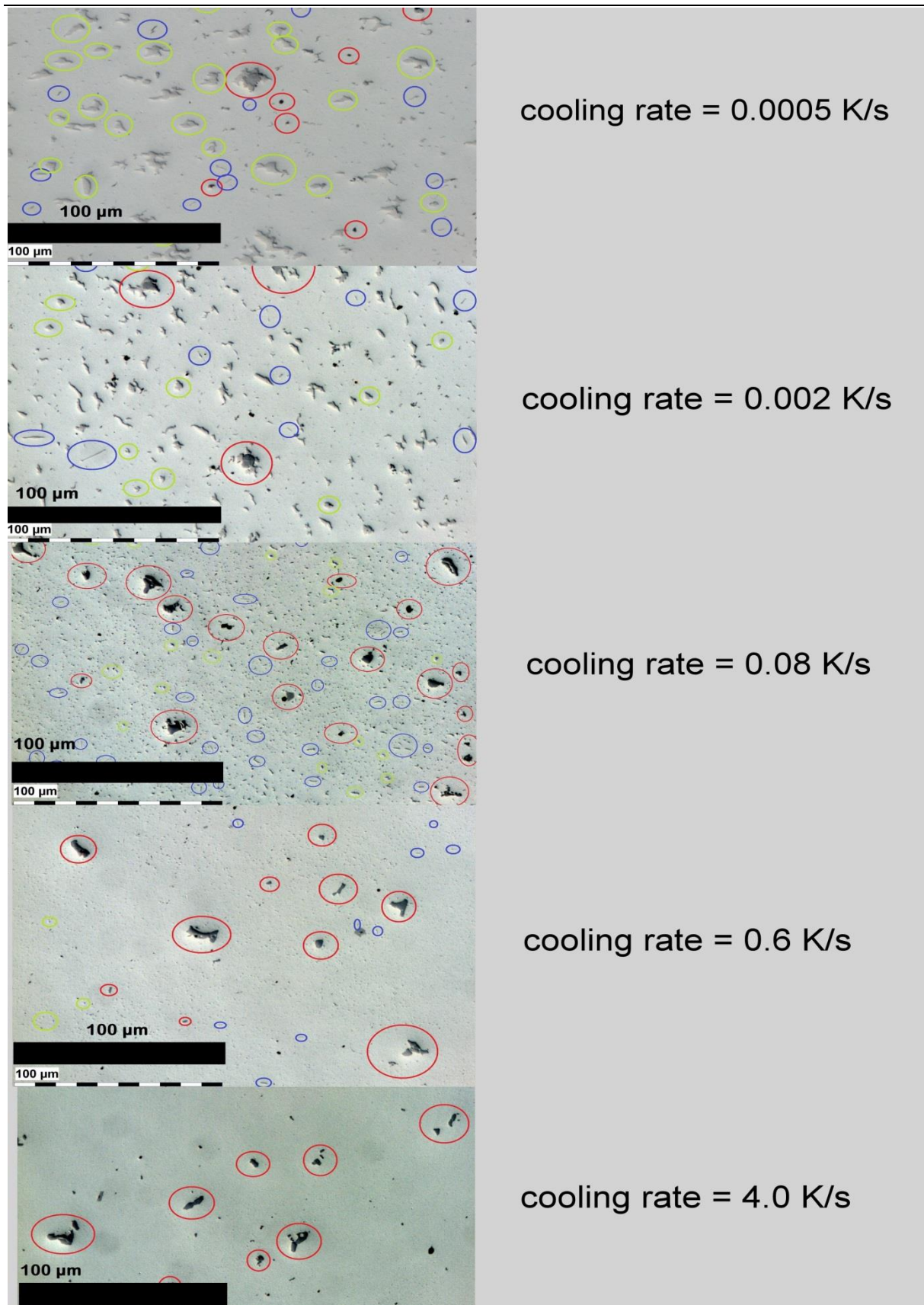


Fig. 49. EN AW 7049A alloy images from metallographic analysis: samples cooled with different rates are compared

In Fig. 49, Fig. 49 comparison of the pictures represents nicely the changes occurring in microstructure with respect to cooling rate change. Though the data coincides with the DSC analysis, and particularly in Fig. 38 and Fig. 40 but is limited to 4 K/s. The range of the cooling rates discussed in Fig. 49 describes the way how three main phases for the particular alloy start to change in size and the geometry changes as well. The red circles represent the primary precipitates, the insoluble phase, and therefore do not change, and show no response to cooling rate, as well as to heat treatment. The blue circles represent the soluble phases which are sensitive to age-hardening. Those start decrease/shrink not only with cooling rate, but also they do change their geometry. Undefined shapes transform to needle like coarse shape. Their size shrinks to less than a μm , and via light microscopy it's not possible to spot them. The Acid green circles are also similar to the blue ones and show the same change over the cooling rate range.

4.4

4.5 Scanning Electron Microscopy and EDX analysis

For conventional imaging in the SEM, specimens must be electrically conductive, at least at the surface, and electrically grounded to prevent the accumulation of electrostatic charge at the surface.

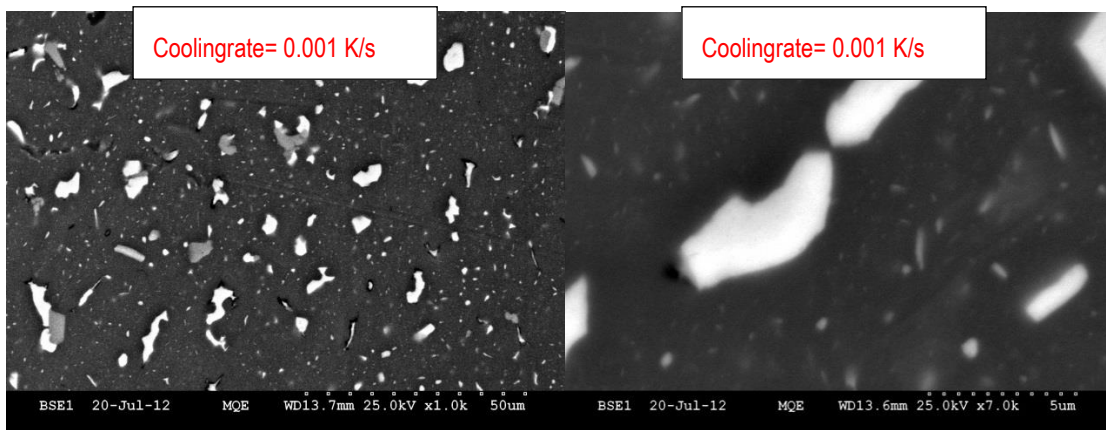


Fig. 50. SEM microscope with opened chamber.

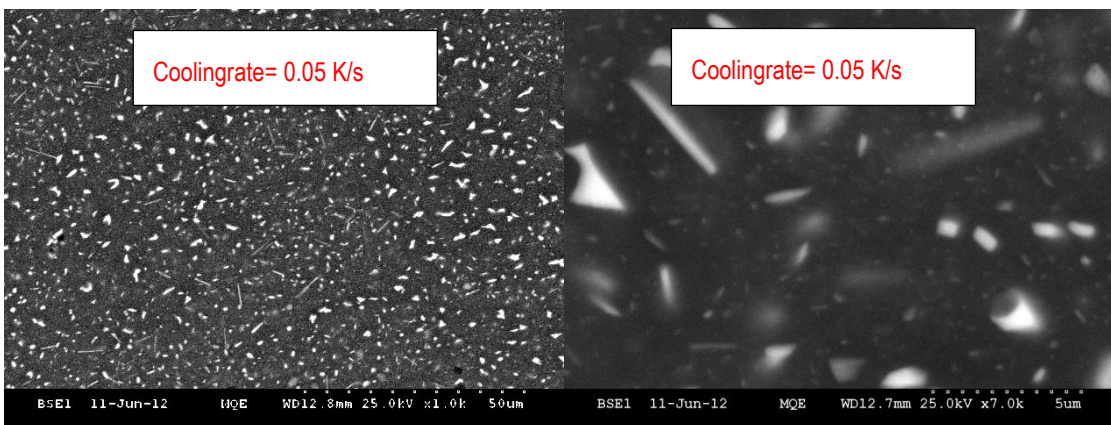
Nonconductive specimens tend to charge when scanned by the electron beam, and especially in secondary electron imaging mode, this causes scanning faults and other image artifacts. They are therefore usually coated with an ultrathin coating of electrically conducting material,

deposited on the sample either by low-vacuum sputter coating or by high-vacuum evaporation. Conductive materials in current use for specimen coating include gold, gold/palladium alloy, [12].

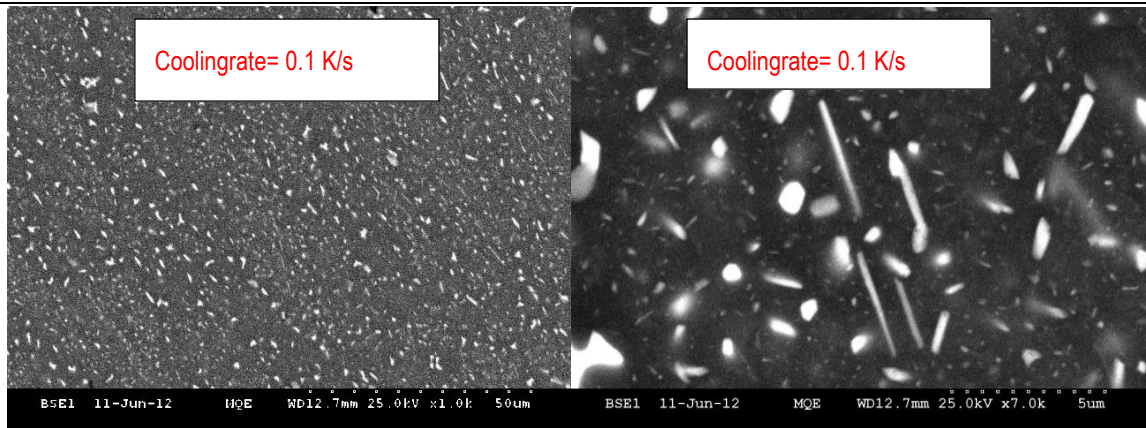
Further in Fig. 51 series of images obtained from SEM microscopy are represented. The images show the change in microstructure with increasing cooling rate inside the suitable samples. For more detailed overview another much higher magnified image is attached to each. The sample cooled with 0.1 K/s shows variety of phases. Some of the grains and grain boundaries are also easily identified for this sample. Higher magnification allows to spot the shapes which are rod like coarse particles and some much brighter with undefined shapes Fig. 51 (a). Samples cooled faster, Fig. 51 (b, c,d,e) show better distribution in comparison to (a), though significant decrease in size occurs.



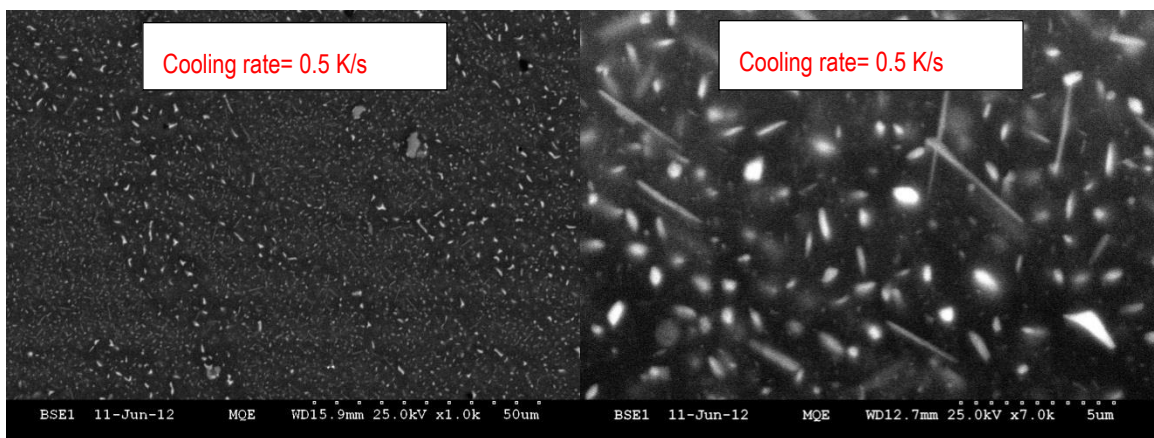
(a)



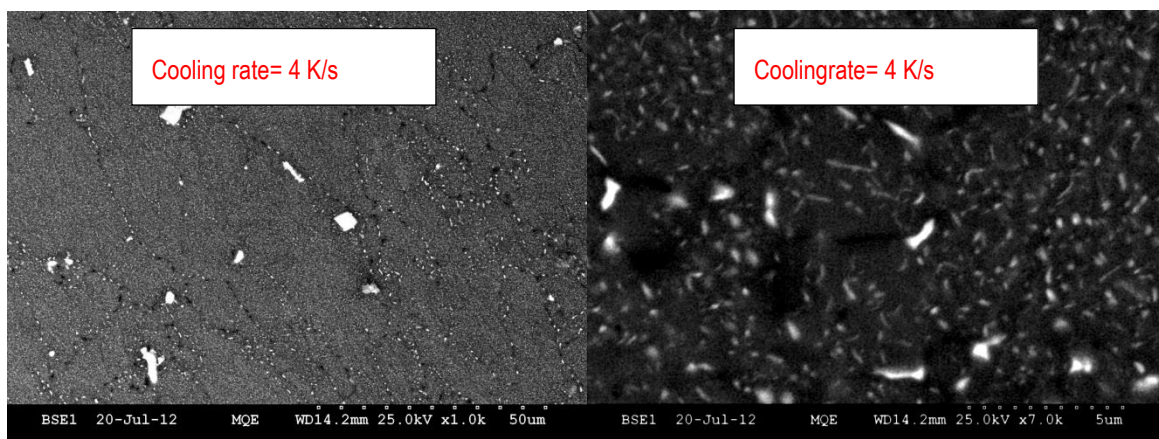
(b)



(c)



(d)



(e)

Fig. 51. EN AW 7049A alloy specimen studied with SEM, the images on left side have magnification 1000X (50 μm scale bar on pic.), and on right side 7000X (scale bar 5 μm on pic.) cooling rate is written on the pictures.

The sample cooled at rate 4K/s has the smallest size above all others, by means of precipitates. Coarse rods like particles tend to concentrate more near grain boundaries Fig. 51 (e). Grains are surrounded with rod-like coarse particles and inside the grain are resting the finer, and several orders of magnitude smaller precipitates Fig. 51 (e). Therefore it is extremely easy to see the contours of the grains and the grain boundaries, in image (e) they have size of c.a. 5 – 50 μm .

The specimen of aluminum alloy EN AW 7049A was solution annealed at 470°C for 30 min and then quenched with the suitable speed. Thin section was analyzed and presented in Fig. 52. On the picture several EDX spots can be seen, which are marked Spectrums 1-4 respectively. They represent the places where the beam was used to analyze the phases.

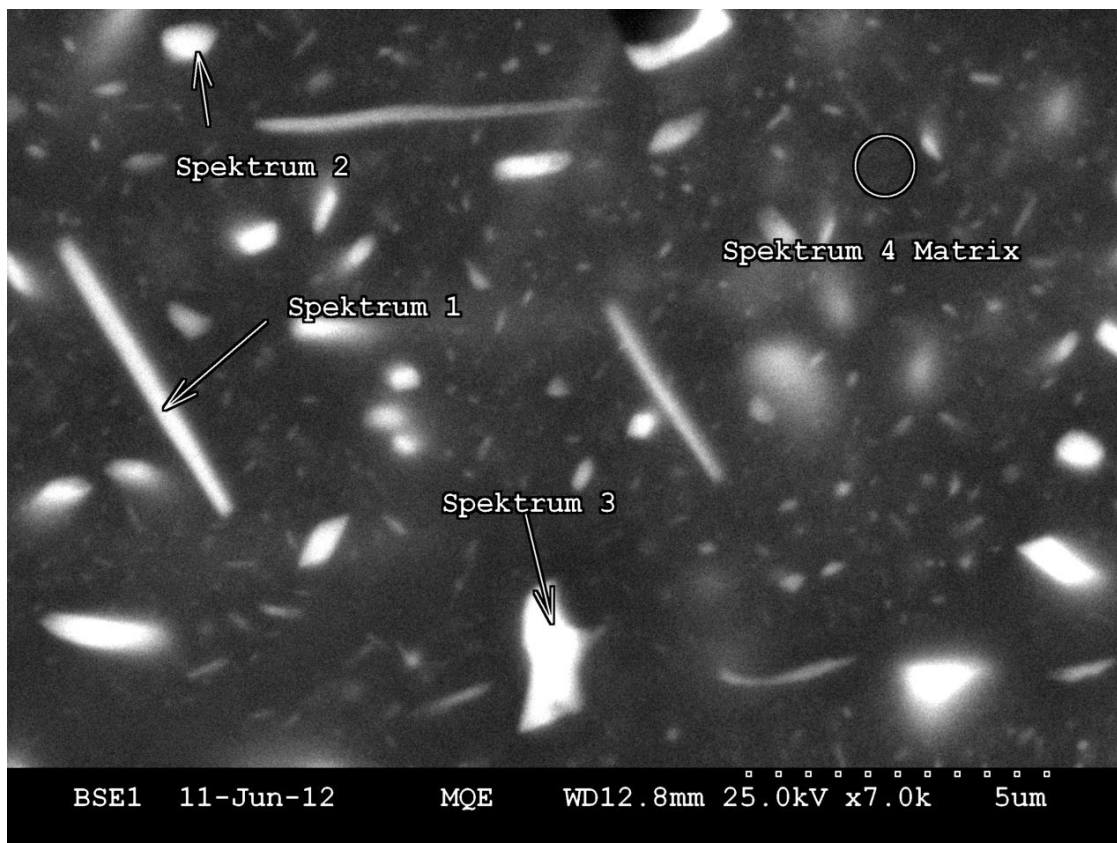


Fig. 52. Specimen of aluminum alloy 7049A was solution annealed at 470 °C for 30 min and then cooled with rate of 0.05 K/s.

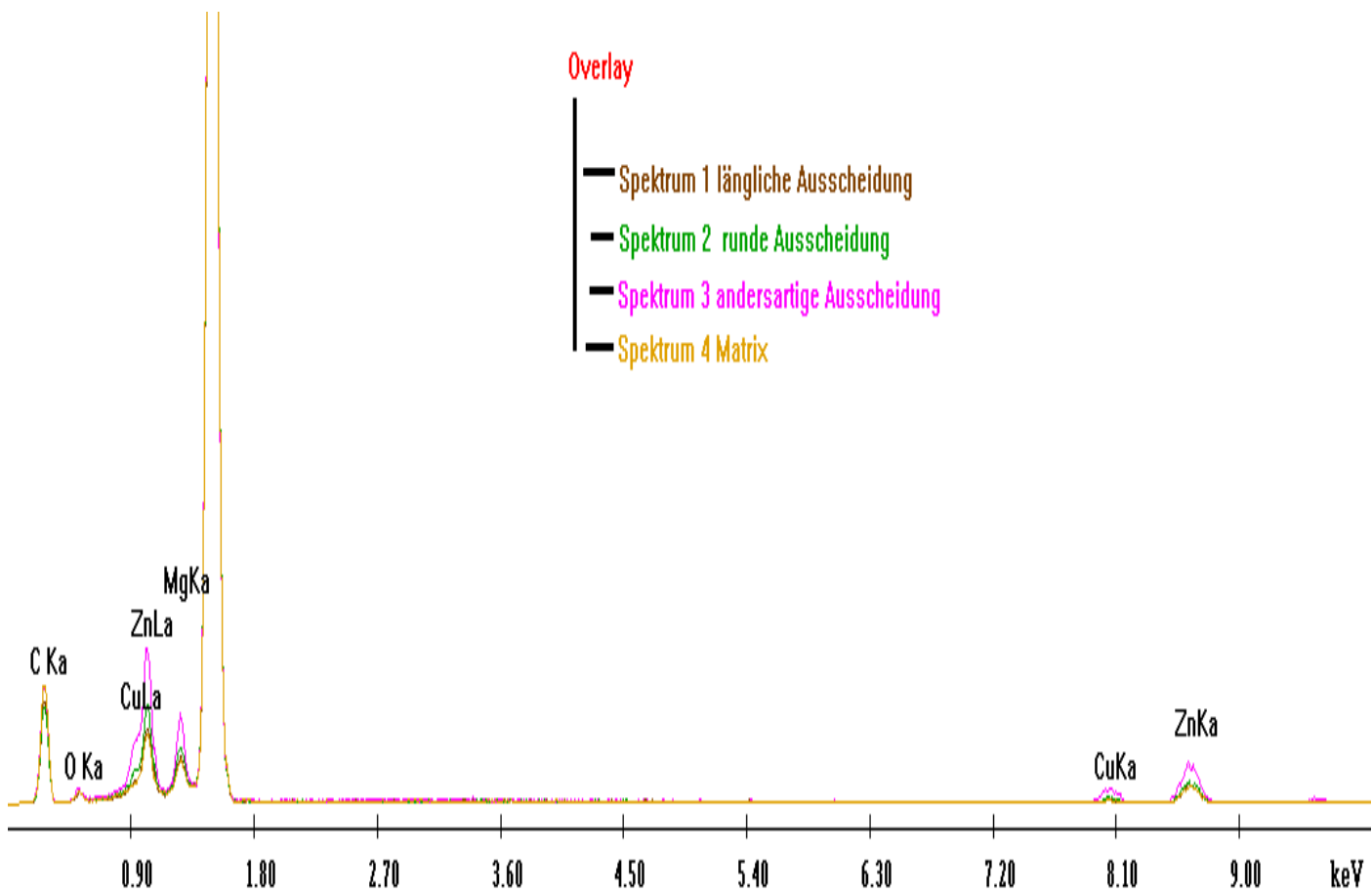


Fig. 53. EDX pattern for the EN AW 7049A alloy, the highest peak corresponds to pure aluminum, the smaller peak are combination of several alloying elements which are found in alloy composition.

Same samples were subjected to analysis via scanning electron microscopy including also the EDX analyses. EDX gives clear understanding of the elements and their concentration in various regions. Having in mind information for chemical structure of the phases helps to understand which chemical structures are influencing the strength Fig. 53.

Specimen of aluminum alloy 7049A was homogenized at 480 °C for 30min and then quenched with 0.5 K/s, thin section specimen for scanning electron microscopy (SEM) was prepared using Jeol EM-09100IS [2]. The instrument irradiates an argon ion beam on the specimen and thins it. The specimen is partially masked with a mask belt (bulk cross section preparation). Thin section specimen was further analyzed by SEM (Jeol JEM-2100) using (EDS, Jeol JED-2300 Series) at 20 kV, Fig. 52. [50]

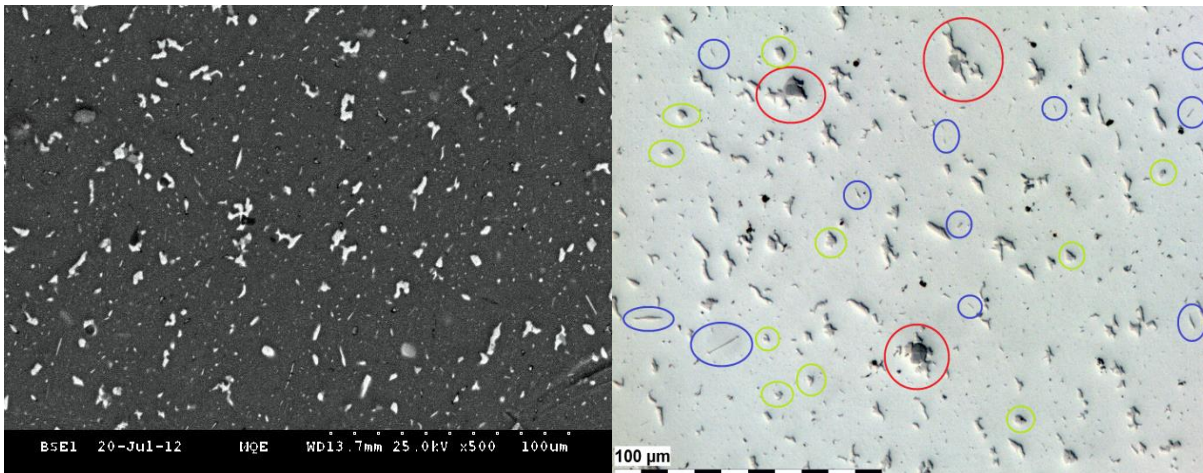


Fig. 54. EN AW 7049A alloy system: SEM (left) and the structure from light microscopy, image on the right. Cooling rate is $\beta = 0.001$ K/s which is very slow, and therefore the precipitates are clearly seen on both pictures.

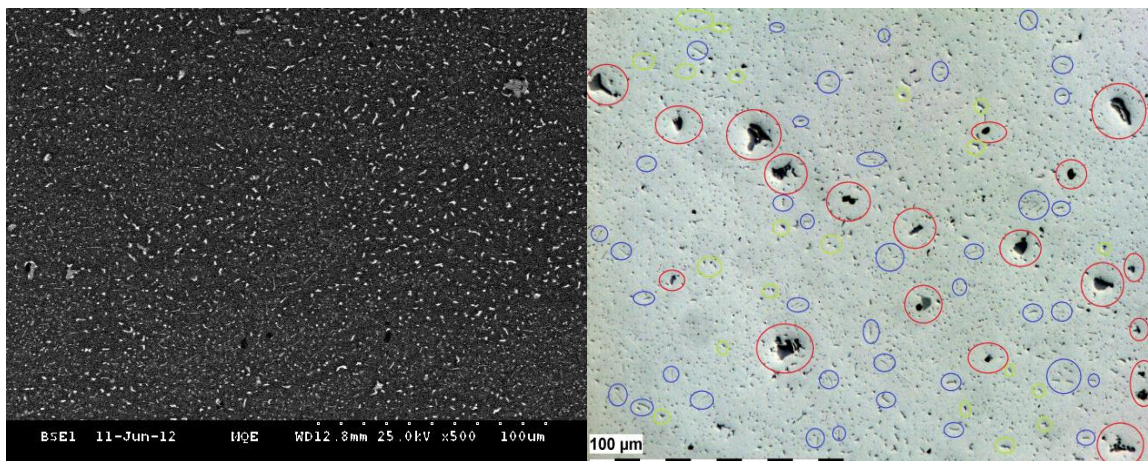


Fig. 55. EN AW 7049A alloy system: SEM (left) and the structure from light microscopy, image on the right. Cooling rate is $\beta = 0.08$ K/s.

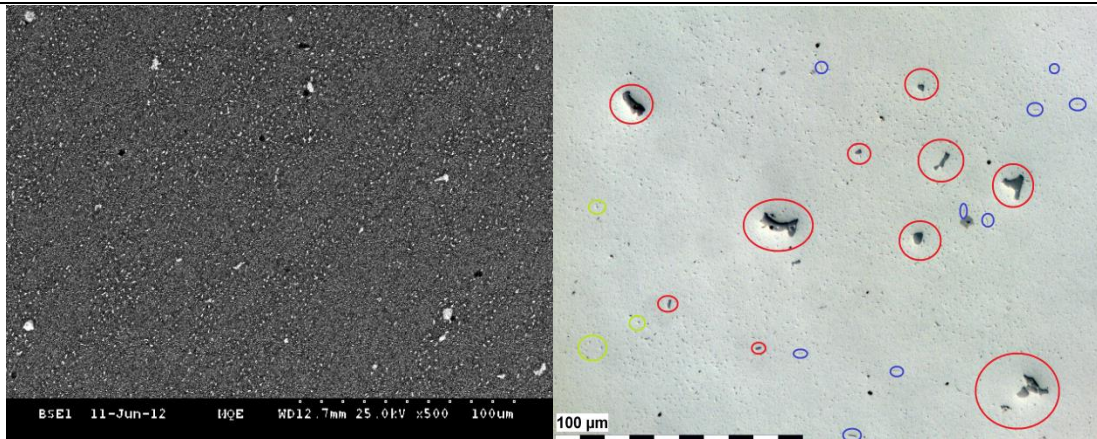


Fig. 56. EN AW 7049A alloy system: SEM (left) and the structure from light microscopy right side, the cooling rate is $\beta = 0.5$ K/s.

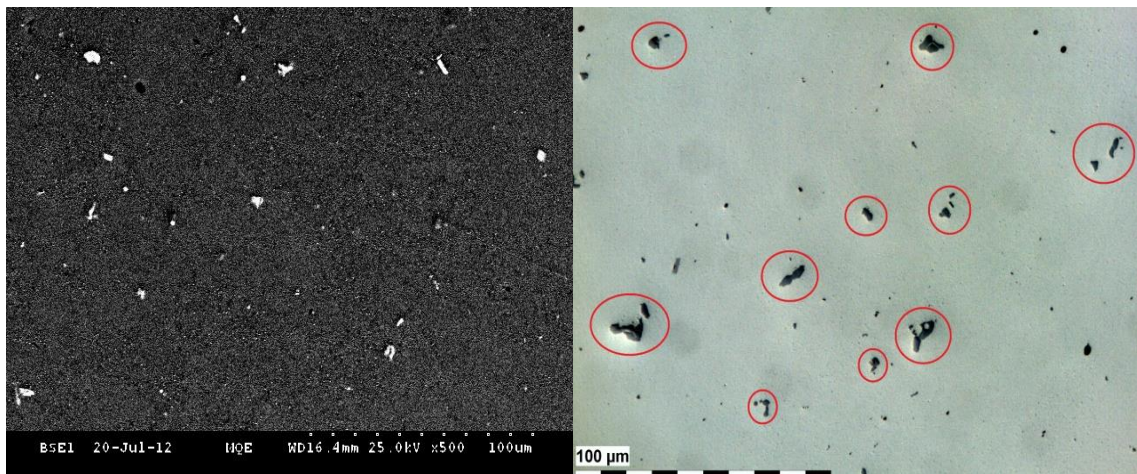
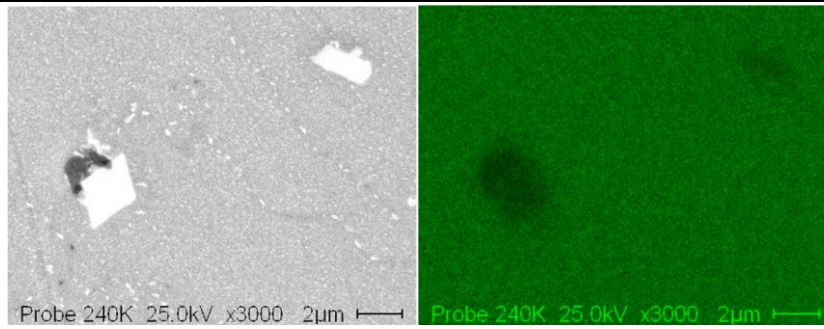


Fig. 57. EN AW 7049A alloy: SEM (left) and the structure from light microscopy, image on the right. Cooling rate is $\beta = 4$ K/s.

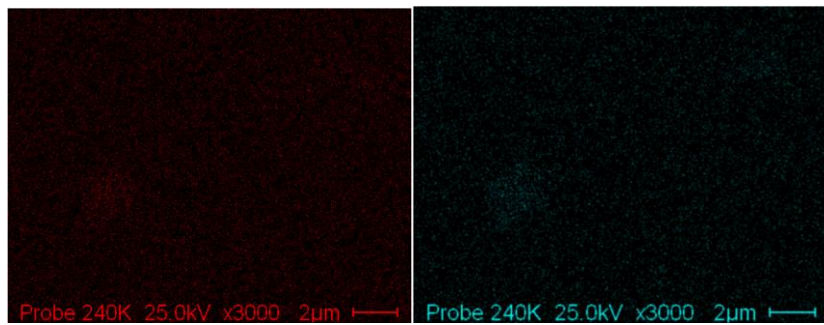
Precipitates differ by morphology, size and contrast. Precipitates include bigger rods of about $1\mu\text{m}$ long and up to 100 nm thick, smaller rods and smaller precipitates of polygonal shapes Fig. 54, Fig. 55, Fig. 56, Fig. 57. By means of EDS it was ascertained that bigger rods were composed of magnesium, aluminum, copper and zinc. Smaller rods contained, apart from those elements, also chromium. Polygonal shaped precipitates differed among each other by contrast, which meant the chemical composition was different. Some contained magnesium, aluminum, copper and zinc but in different ratios as in bigger rods. Other contained additionally, chromium, copper, zinc, nickel, iron and manganese Fig. 58.



SE picture

(a)

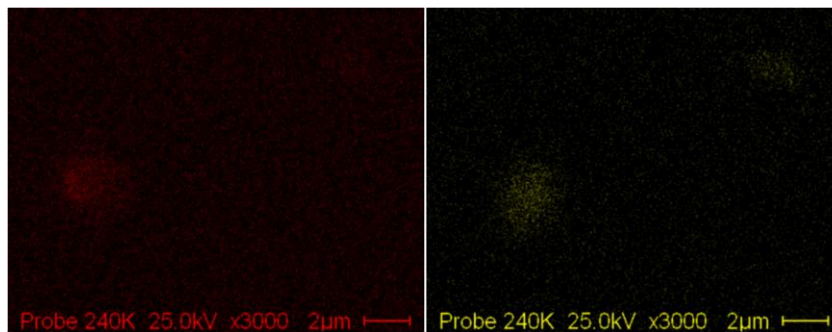
Aluminum



Zink

(b)

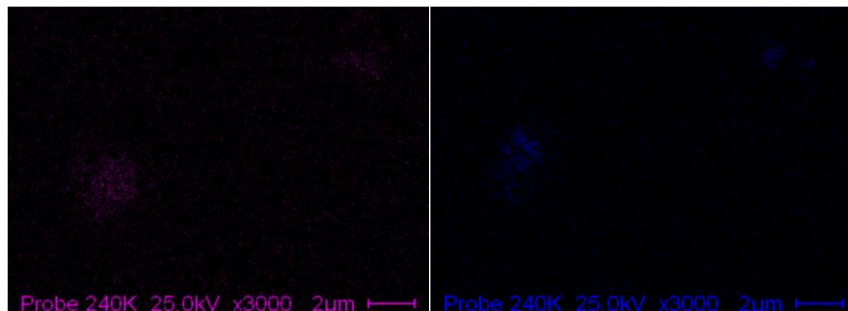
Copper



Magnesium

(c)

Chromium



Manganese

(d)

Titan

Fig. 58. Elemental mapping of the EN AW 7049A alloy sample from Fig. 57, cooling rate $\beta = 4$ K/s.

Element maps show the spatial distribution of elements in a sample. Maps of different elements over the same area can help to determine what phases are present. Element maps give a complete 2D picture of internal chemical zonation within a mineral, which is more informative than a simple line traverse. Element maps are recorded digitally and can be saved to use as sample maps for locating spot analyses.

Unlike back-scattered electron images (BSE), which only show average Z in a phase, element maps show the true spatial distribution of each element of interest. In these examples, the chemical zonation in plagioclase is clear for the elements Fig. 58 (c), Mg (left) and Cr (right), or Fig. 58 (d) the Mn (left) and Ti (right). Element maps are often displayed in false color, which helps the human eye distinguish subtle variations by expanding the range of visible hues Fig. 58. Here, higher concentrations are yellow and orange, whereas lower concentrations are magenta to blue.

4.5 Nano-Indentation results

Defining the point of initial contact is the critical starting point in the analysis of almost all instrumented indentation data. Load/displacement curves Fig. 59, as well as the data acquisition rates clearly define how well one can determine the location of the surface. However, it is also important to be able to resolve and detect near-surface forces, as these often have an important bearing on the interpretation of the surface location. Because of these, techniques that use preload or back extrapolation of the data to determine the point of initial

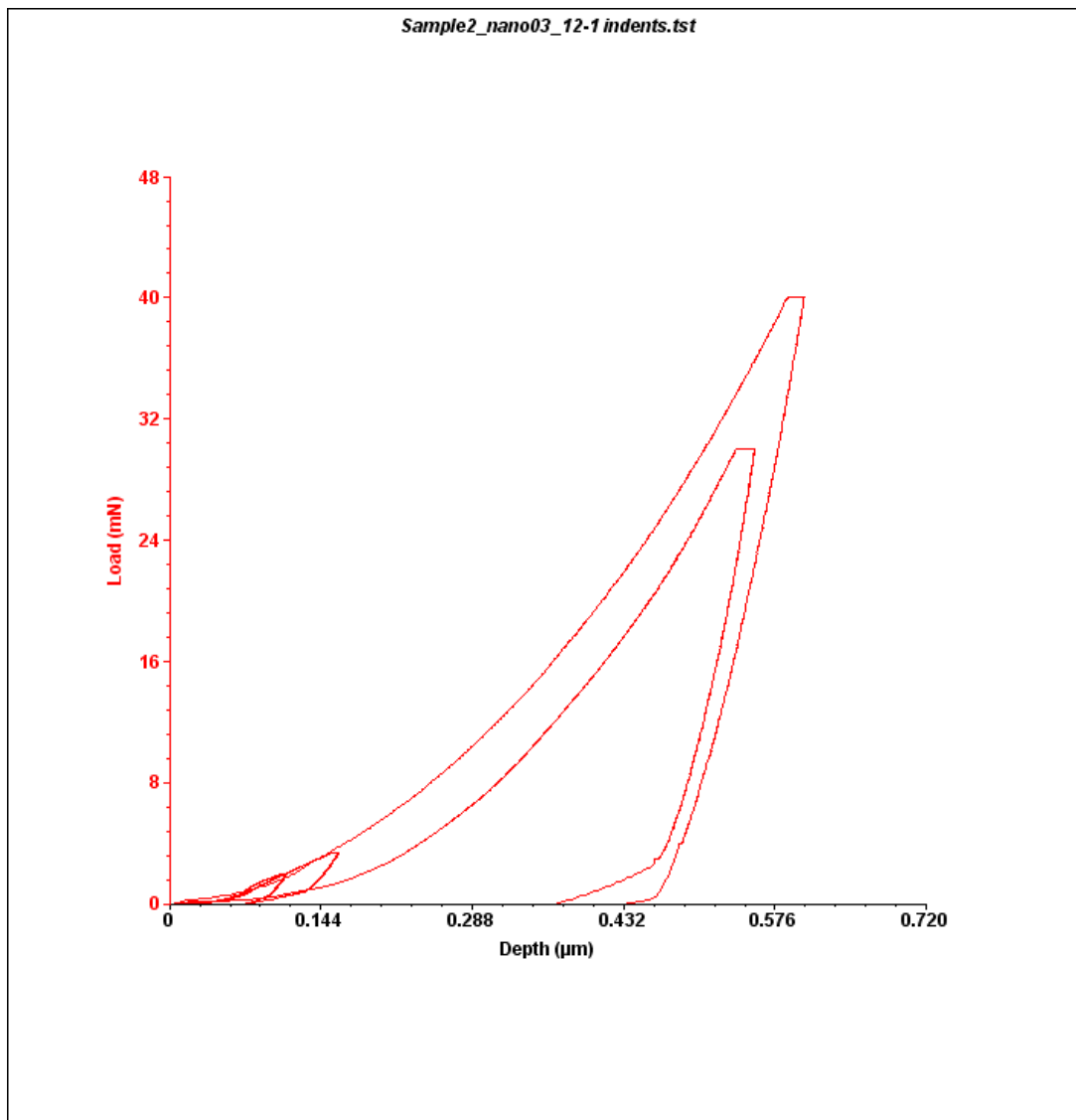


Fig. 59. Load vs. displacement curve for the EN AW 7049A alloy nano-specimen. The indentation depth is shown in mN.

contact can be misleading. The approach we prefer is to observe the entire mechanical response of the system before, during, and after the point of initial contact and identify the point of contact by examining the overall observed behavior.

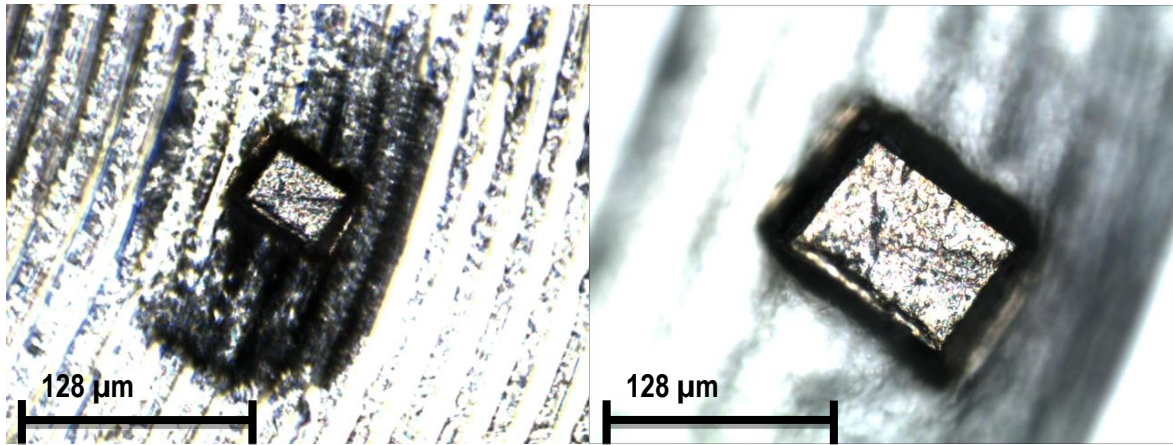


Fig. 60. EN AW 7049A alloy specimen used for nano-indentation experiments, quenching rate 1000 K/s, inside DFSC Flash-1 (Mettler-Toledo).

Test repetition	Avg. Modulus [170-180 nm]	Avg. Red Modulus	Avg. Hardness [170-180 nm]
	GPa	GPa	GPa
1	46.7	50.4	0.89
2	67.6	71.6	1.56
3	55.4	59.4	0.91
4	64.2	68.3	1.89
5	36.1	39.4	0.45
6	70.3	74.3	1.74
8	59.9	64	1.45
Mean	57.2	61.1	1.27
Std. Dev.	12.2	12.5	0.53

Table No2.EN AW 7049A data obtained from nano-indentation analyzer.

In assumption of these facts discussed above for the small nano/micro scale it is possible to make hardness analysis. This statement is of great importance and very useful especially for research fields dealing with the DFSC. Those studies nearly always involve extremely small specimens for analysis see Fig. 60. Thus results need to be compared with nano calorimetry, where the sample has several microns dimensions. Procedures described here represent how such experiments can be realized using various nano scale indentation techniques.

The Hardness of EN AW 7049A for the 1000 K/s cooled samples has been determined by nano-indentation to about 1.3 ± 0.5 GPa see (table 2). Although the comparison is very difficult, this is the same magnitude as Vickers Hardness testing in Fig. 45, resulting in about 180 HV1 for high quenching rates. Scattering of the nano-indentation is still high and has to be reduced for the DFSC samples.

5 Summary

The exothermal heat flow from quench-induced precipitation in alloy EN AW 7049A during cooling was investigated by measuring excess specific heat capacity curves with DSC measurements. The influence of the cooling rate on the precipitation behaviour was described by means of a newly developed Continuous Cooling Precipitation (CCP) diagram. The results show that there are at least three different quench-induced precipitation reactions that occur during cooling in specific cooling rate ranges.

Precipitation reactions inside aluminium alloys are known to be very important for hardness and yield strength. Premature precipitation during quenching from solution annealing decreases the yield strength after aging. Differential fast-scanning calorimetry was applied to cover the cooling rate range needed for high alloyed materials. A new methodology, called Differential reheating method, was applied for differential fast-scanning calorimetry (DFSC) and differential scanning calorimetry (DSC). The method was quantitatively verified with EN AW 6063 alloy in a DSC due to its low critical cooling rate. The combination of DSC and DFSC extends the available cooling rate range for precipitation studies from mK/s up to some 10,000 K/s. The critical cooling rate for the quench sensitive EN AW 7049A alloy was determined as 300 K/s.

The new differential reheating method presented here, can be used to characterize the precipitation process during previous cooling of aluminum alloys. The advantages of this method are the following:

- Precipitation monitoring up to critical cooling rate region even for high alloyed aluminum alloys with high critical cooling rates seems to be possible by applying fast scanning calorimetry, DFSC
- Precipitation enthalpy can be assessed from heating scans collected at optimum experimental conditions without collecting data from the previous cooling step at varying cooling rate.

The prerequisites to be fulfilled for the successful application of the reheating analysis are

- (i) a reheating curve after overcritical cooling must be available as a reference, and
- (ii) The dissolution of the precipitates must be finalized during the heating scan.

The latter condition limits the applicable heating rates as well as the lowest cooling rates because of the stability of the precipitates. But the differential reheating method allows the determination of the critical cooling rate probably for a large number of available aluminum alloy.

Eidesstattliche Versicherung

Ich versichere eidesstattlich durch eigenhändige Unterschrift, dass ich die Arbeit selbstständig und ohne Benutzung anderer als der angegebenen Hilfsmittel angefertigt habe. Alle Stellen, die wörtlich oder sinngemäß aus Veröffentlichungen entnommen sind, habe ich als solche kenntlich gemacht. Ich weiß, dass bei Abgabe einer falschen Versicherung die Prüfung als nicht bestanden zu gelten hat.

Rostock, den 10.02.2014

(Unterschrift Student)

Abkürzungsverzeichnis

DSC – Differential scanning calorimetry

DFSC-Differential fast scanning calorimetry

DRM- Differential reheating method

β – Cooling rate

CCP-critical cooling rate

EDX-Energy dispersive X-Ray

SEM-Scanning Electron microscopy

TEM-transmission electron microscopy

HV- hardness Vicker's

Cp- specific heat capacity

GP- Guinier-Preston zones

CCR- Critical cooling rate

SSSS-Super saturated solid solution

MPa- megaPascals

mK/s – mega Kelvins per second

GPa – gigaPascals

DAC-Digital analog converter

T – temper mode

Ref – reference

TMDSC – temperature modulated DSC

XI-Xensor Integration

KeV- kilo electron Volt

Dil-dilatometer

PID- Proportional, Integral, and Derivative.

6 References

1. Polmear, I.J., *From Traditional Alloys to Nanocrystals*. 2006: Elsevier.
2. Bertsch, G., *Melting in Clusters*. Science, 1997. **277**(5332): p. 1619-1619.
3. Cavazos, J.L. and R. Colás, *Quench sensitivity of a heat treatable aluminum alloy*. Materials Science and Engineering A, 2003. **363**(1-2): p. 171-178.
4. Milkereit, B., O. Kessler, and C. Schick, *Continuous Cooling Precipitation Diagrams of Aluminium-Magnesium-Silicon Alloys*, in *Aluminium Alloys*, S.B. Hirsch J, Gottstein G, Editor. 2008, Deutsche Gesellschaft für Materialkunde e.V.; WILEY-VCH Weinheim: Aachen, Germany. p. 1232-1237.
5. Milkereit, B., *Kontinuierliche Zeit-Temperatur-Ausscheidungs-Diagramme von Al-Mg-Si-Legierungen*, in *Fakultät für Maschinenbau und Schiffstechnik*. 2011, University of Rostock: Rostock. p. 178.
6. Milkereit, B., et al., *Precipitation kinetics of an aluminium alloy during Newtonian cooling simulated in a differential scanning calorimeter*. Thermochemica Acta, 2011. **522**(1-2): p. 86-95.
7. Deschamps, A., et al., *Influence of cooling rate on the precipitation microstructure in a medium strength Al-Zn-Mg alloy*. Materials Science and Engineering: A, 2009. **501**(1-2): p. 133-139.
8. Milkereit, B., O. Kessler, and C. Schick, *Recording of continuous cooling precipitation diagrams of aluminium alloys*. Thermochemica Acta, 2009. **492**(1-2): p. 73-78.
9. Milkereit, B., C. Schick, and O. Kessler. *Continuous Cooling Precipitation Diagrams Depending on the Composition of Aluminum-Magnesium-Silicon Alloys*. in *12th International Conference on Aluminium Alloys*. 2010. The Japan Institute of Light Metals.
10. Takeuchi, A. and A. Inoue, *Quantitative evaluation of critical cooling rate for metallic glasses*. Materials Science and Engineering: A, 2001. **304-306**: p. 446-451.
11. Evancho, J.W. and J.T. Staley, *Kinetics of Precipitation in Aluminum-Alloys during Continuous Cooling*. Metallurgical Transactions, 1974. **5**(1): p. 43-47.
12. Cahn, R.W., *Combining metals and sciences: ways of investigating intermetallics*. Intermetallics, 1998. **6**(7-8): p. 563-566.
13. Herding, T., et al. *An approach for Continuous Cooling Transformation (CCT) diagrams of aluminium alloys*. in *8th International Conference on Aluminium Alloys: Their Physical and Mechanical Properties*. 2002. Cambridge, UK: Trans Tech Publications Ltd.
14. Kessler, O., et al. *Continuous cooling transformation (CCT) diagram of aluminum alloy Al-4.5Zn-1Mg*. in *10th International Conference on Aluminium Alloys*. 2006: WILEY-VCH Weinheim.
15. Zhuravlev, E. and C. Schick, *Fast scanning power compensated differential scanning nanocalorimeter: 1. The device*. Thermochemica Acta, 2010. **50**(1-2): p. 1-13.
16. Minakov, A.A. and C. Schick, *Ultrafast thermal processing and nanocalorimetry at heating and cooling rates up to 1 MK/s*. Review of Scientific Instruments, 2007. **78**(7): p. 073902-10.
17. Adamovsky, S.A., A.A. Minakov, and C. Schick, *Scanning microcalorimetry at high cooling rate*. Thermochemica Acta, 2003. **403**(1): p. 55-63.
18. I. J. Polmear, *Light Alloys: Metallurgy of the Light Metals*. 1988, Melbourne.

19. Chattopadhyay, K. and R. Goswami, *Melting and Superheating of Metals and Alloys*. Prog. Mater. Sci., 1997. **42**(1-4): p. 287-300.
20. von Barga, R., O. Kessler, and H.W. Zoch, *Kontinuierliche Zeit- Temperatur-Ausscheidungsdiagramme der Aluminiumlegierungen 7020 und 7050*. HTM Zeitschrift für Werkstoffe, Wärmebehandlung, Fertigung, 2007. **62**(6): p. 8.
21. C.H.J. Davies, N.R., T. Sheppard, *Ageing Kinetics of a silicon Carbide Reinforced Al-Zn-Mg-Cu alloy*. Acta Materialia, 1994. **42**: p. 309-318.
22. D. Godard, et al, *Precipitation sequences during quenching of the AA 7010 alloy*. Acta Materialia, 2002. **50**: p. 2319-2329.
23. M. J. Starink, et al, *A Model for the Electrical Conductivity of Peak-aged and Overaged Al-Zn-Mg-Cu Alloys*. Metallurgical and Materials Transactions A, 2007. **34**(4): p. 899-911.
24. Ajayan, P.M. and L.D. Marks, *Quasimelting and phases of small particles*. Phys. Rev. Lett., 1988. **60**(7): p. 585-587.
25. Polmear, I.J., *Light alloys : from traditional alloys to nanocrystals*. 4th ed. 2006, Oxford ; Burlington, MA: Elsevier/Butterworth-Heinemann. xiv, 421 p.
26. Cahn, J.W., *The Kinetics of Grain Boundary Nucleated Reactions*, in *The Selected Works of John W. Cahn*. 1998, John Wiley & Sons, Inc. p. 10-12.
27. Zhuravlev, E. and C. Schick, *Fast scanning power compensated differential scanning nano-calorimeter: 2. Heat capacity analysis*. Thermochemica Acta, 2010. **50**(1-2): p. 14-21.
28. Aziz, M.J., *Interface Attachment Kinetics in Alloy Solidification*. Metall. Mater. Trans. A, 1996. **27**(3): p. 671-686.
29. Bachmann, R., et al., *Heat capacity measurements on small samples at low temperatures*. Rev. Sci. Instrum., 1972. **43**(2): p. 205-214.
30. Bach, F.W., P. Stoll, and T. Krussel, *Rapid thermal analysis of solid materials*. Metall, 2002. **56**(4): p. 214-217.
31. Zohrabyan, D., et al., *Precipitation enthalpy during cooling of aluminum alloys obtained from calorimetric reheating experiments*. Thermochemica Acta, 2012. **529**: p. 51-58.
32. Wurm, A., M. Merzlyakov, and C. Schick, *TMDSC and DMA Measurements in the Crystallization and Melting Region of Polymers*. Proc. 25th NATAS Conference, McLean, Va., 1997: p. 319-326.
33. Airoldi, G., et al., *DSC calibration in the study of shape memory alloys*. J. Therm. Anal., 1994. **42**(4): p. 781-791.
34. Chandler, H., *Heat treater's guide: practices and procedures for nonferrous alloys*. 1996: ASM International. 241.
35. Milkereit, B., et al., *Das kontinuierliche Zeit- Temperatur- Ausscheidungs- Diagramm einer Aluminiumlegierung EN AW-6005A*. HTM J. Heat Treatm. Mat., 2010. **65**(3): p. 159-171.
36. A. Deschamps, Y.B., *Nature and Distribution of Quench-Induced Precipitation in an Al-Zn-Mg-Cu Alloy*. Scripta Materialia, 1998. **39**: p. 1517-1522.
37. Shengdan Liu, Q.Z., Yong Zhang, Wenjun Liu, Xinming Zhang, Yunlai Deng, *Investigation of Quench Sensitivity of High Strength Al-Zn-Mg-Cu alloys by time-temperature-properties Diagrams*. Materials & Design, 2010. **31**: p. 3116-3120.

38. Merzlyakov, M. and C. Schick, *Complex heat capacity measurements by TMDSC Part 1. Influence of non-linear thermal response*. Thermochem. Acta, 1999. **330**: p. 55-64.
39. Merzlyakov, M. and C. Schick, *Complex heat capacity measurements by TMDSC Part 2: Algorithm for amplitude and phase angle correction*. Thermochem. Acta, 1999. **330**: p. 65-73.
40. Allen, S.M. and J.W. Cahn, *Coherent and incoherent equilibria in iron-rich iron-aluminum alloys*. Acta Metallurgica, 1975. **23**(9): p. 1017-1026.
41. W.C. Oliver, G.M.P., *Measurement of hardness and elastic modulus by instrumented indentation: Advances in understanding and refinements to methodology*. Journal of Materials Research, 23 September 2003. **19**(No. 1).
42. Nix, W.D., *Yielding and strain hardening of thin metal films on substrates*. Scripta Materialia, 1998. **39**(4-5): p. 545-554.
43. Adamovsky, S., et al., *Fractions of different mobility in semicrystalline polymers revealed from temperature dependent heat capacity and NMR measurements*. Proceedings NATAS 2000, 2000: p. 351-356.
44. Boller, A., C. Schick, and B. Wunderlich, *Modulated Differential Scanning Calorimetry in the Glass Transition Region*. Proc. 23rd NATAS Conference, Toronto, 1994: p. 1.
45. Boller, A., C. Schick, and B. Wunderlich, *Modulated differential scanning calorimetry in the glass transition region*. Thermochem. Acta, 1995. **266**: p. 97-111.
46. Hensel, A. and C. Schick, *Relation between freezing-in due to linear cooling and the dynamic glass transition temperature by temperature-modulated DSC*. J. Non-Cryst. Solids, 1998. **235-237**: p. 510-516.
47. Weyer, S., M. Merzlyakov, and C. Schick, *Application of an extended Tool-Narayanaswamy-Moynihan model Part 1. Description of vitrification and complex heat capacity measured by temperature-modulated DSC*. Thermochem. Acta, 2001. **377**(1-2): p. 85-96.
48. Wurm, A. and C. Schick, *Development of thermal stability of polymer crystals during isothermal crystallisation*. E-Polymers, 2002. **24**: p. 1-15.
49. Akiba, A., et al., *Specific heat of NaV6O11 single crystals*. J. Phys. Soc. Jpn., 1998. **67**(4): p. 1303-1305.
50. Wu, R.I., G. Wilde, and J.H. Perepezko, *KINETICS OF GLASS FORMATION AND NANOCRYSTALLIZATION IN Al-RE-(TM) ALLOYS*. Ultrafine Grained Materials, ed. S.L.S.C.S.u.a. R. S. Mishra. 2000. 63-72.